Doctoral Thesis on

Signal Processing Methods for Localisation and Medium Characterisation in Remote Sensing Applications

Giuseppe Giammello

Università Degli Studi di Catania
Dipartimento di Ingegneria Elettrica, Elettronica e Informatica

Signal Processing Methods for Localisation and Medium Characterisation in Remote Sensing Applications

Copyright

Thesis valid to obtain the doctorate in *Systems, Energetic, Informatics, and Communications Engineering* at *Università Degli Studi di Catania*, *Dipartimento di Ingegneria Elettrica, Elettronica e Informatica*.

Doctoral Candidate	Giuseppe Giammello
Supervisor	Gino Sorbello

Colophon

This document was typeset with the help of KOMA-Script and LaTeX using the kaobook class.

Preface

This thesis deals with two common applications in remote sensing, namely the task of localisation in passive remote sensing and the medium characterisation in active remote sensing. Two novel approaches are presented, using and combining together the latest trends in literature for both the topics. For localisation, a new approach to deal with the direction of arrival (DoA) problem is presented, along with a new metric to evaluate the correctness of the estimation. As medium characterisation, a novel approach to estimate the drop size distribution (DSD) is proposed, which exploits the features of polarimetric radar measurements and the pattern-recognition capacity of a fully connected neural network (FCNN).

Giuseppe Giammello

Contents

Preface iii

Contents v

Conventions and Symbols xi
- Mathematical conventions xi
- Symbols xi

Acronyms xiii

1 Introduction 1
- 1.1 Detection and localisation in passive remote sensing 2
- 1.2 Medium characterisation in active remote sensing 3
- 1.3 Outline 4

2 Overview on the Direction of Arrival estimation 5
- 2.1 Introduction 5
- 2.2 Antenna array theory 7
  - 2.2.1 Conventional Steering Vectors 10
- 2.3 Algorithms 10
  - 2.3.1 Bartlett 11
  - 2.3.2 MUSIC 11
- 2.4 Conclusions 13

3 Embedded Radiation Patterns for Direction of Arrival estimation 15
- 3.1 Introduction 15
- 3.2 System model 16
- 3.3 Detection and localisation 20
  - 3.3.1 Detection 20
  - 3.3.2 Localisation 20
- 3.4 Localisation performance evaluation 21
  - 3.4.1 Antenna array size 22
  - 3.4.2 Method for array response reconstruction 24
  - 3.4.3 Number of snapshots 25
- 3.5 Conclusions 28

4 Error metrics for Direction of Arrival estimation 31
- 4.1 Introduction 31
- 4.2 Error metrics 32
  - 4.2.1 Proposed metric 33
- 4.3 Experimental validation 34
- 4.4 Conclusions 37

5 Drop Size Distribution retrieval through Deep Learning approach 39
- 5.1 Introduction 39
- 5.2 Theory 41
  - 5.2.1 Radar scattering 41

5.2.2 Drop Size Distribution 44
5.3 Methodology 45
5.3.1 Dataset generation 45
5.3.2 Neural network design 48
5.4 Results 51
5.4.1 Frequency dependence 57
5.5 Conclusions 64

6 Conclusions **67**

Bibliography **71**

List of Publications **79**

Alphabetical Index **81**

List of Figures

3.1 Indoor propagation model 17
3.2 Mean Absolute Error over azimuth per different antennas sizes 23
3.3 Receiver with different iter-element distances 23
3.4 Mean Absolute error on azimuthal plane 24
3.5 Mean Absolute Error over elevation per different antennas sizes 25
3.6 Mean Absolute Error for CSV and ERP approaches 26
3.7 Mean Absolute Error for ERP approach for 3x3 and 4x4 arrays 27
3.8 Mean Absolute Error with ERP approach for algorithm comparison 28

4.1 Direction of arrival limit case for classic error metrics 33
4.2 Error comparison for different metrics and test cases 35
4.3 Error comparison for different reference frames 36
4.4 Error comparison for different trials 37

5.1 Generic DSD example 40
5.2 Parameters effect on gamma DSD 46
5.3 Representation of Fisher distribution for chosen values 47
5.4 Errors on DSD parameters estimation 52
5.5 PDFs of the true and estimated DSD parameters 53
5.6 Difference in median diameter between the estimated and true DSD 54
5.7 Difference in terminal velocity between the estimated and true DSD 55
5.8 Kullback-Leibler divergence between the estimated and true DSD 56
5.9 Total number concentration ratio between the estimated and true DSD 56
5.10 Errors on the first DSD parameter estimation across frequencies 58
5.11 Errors on the second DSD parameter estimation across frequencies 59
5.12 Difference in median diameter (estimated and true DSD) across frequencies 60
5.13 Difference in terminal velocity (estimated and true DSD) across frequencies 61
5.14 Kullback-Leibler divergence between estimated and true DSD across frequencies 62
5.15 Total number concentration ratio (estimated over true DSD) across frequencies 63

List of Tables

4.1 Test cases (TC) for error comparison in 2D DoA estimation. 34

5.1 Parameters to generate dataset of covariance matrices 46
5.2 FCNN configuration for DSD retrieval 49
5.3 Frequencies and water permittivities adopted to train the FCNN. 57

Conventions and Symbols

Mathematical conventions

Here is a summary about the mathematical notation used throughout the text, even for different topics. The appropriate symbols and constants used for each topic are listed in the *Symbols* section.

General variables representing scalar quantities are identified by *italic* latin letters ($a - z$, $A - Z$), and greek letters ($\alpha - \omega$, $A - \Omega$). When the variables represent a vector quantity, they are identified by **bold** latin and greek letters ($\mathbf{a}$, $\mathbf{A}$, $\boldsymbol{\alpha}$, $\mathbf{A}$, etc.).

A matrix is represented using a bold uppercase latin or greek letter with a bar below the letter; some examples can be $\underline{\mathbf{A}}$, $\underline{\mathbf{B}}$, $\underline{\boldsymbol{\Gamma}}$. The zero vector is identified by a bold zero, i.e. $\mathbf{0}$, while the zero matrix with a bold underlined zero, $\underline{\mathbf{0}}$. The identity matrix is represented with a bold underlined capital i, $\underline{\mathbf{I}}$. The transpose of a matrix is written with a capital T superscript, i.e. $\underline{\mathbf{A}}^{\mathrm{T}}$.

There is no particular notation for complex numbers, they follow the previous notation for scalar, vector and matrix quantities. The imaginary unit is represented with the lowercase italic j, where $j = (-1)^{1/2}$. The complex conjugate is done by putting a *star* superscript above the variable, e.g. z^*; if the variable is a matrix quantity, then this notation identifies the conjugate transpose of that matrix (e.g. $\underline{\mathbf{A}}^*$). When the matrix is Hermitian, a capital H superscript is used to write the conjugate transpose ($\underline{\mathbf{A}}^{\mathrm{H}}$).

Another general notation is the usage of a *hat* diacritic above the variable. This identifies the variable as the estimated version of the "*truth*" variable (if a is the true quantity, $\hat{a}$ is the estimated one). This notation is applied to the vector and matrix quantities that are estimated, too. This diacritic, together with the notation to write a vector, may be used to represent a *unit vector*, depending on the context.

The components of a vector quantity are represented by using the same letter as the vector, but not in bold, and with a subscript identifying the component they refer to; this notation applies to both when the basis elements are identified through unit vectors ($\mathbf{a} = a_x\hat{\mathbf{x}} + a_y\hat{\mathbf{y}} + a_z\hat{\mathbf{z}}$) and when they are identified by an index ($\mathbf{a} = a_1\hat{\mathbf{u}}_1 + a_2\hat{\mathbf{u}}_2 + a_3\hat{\mathbf{u}}_3$). The same notation works when vectors are written in vector form ($\mathbf{a} = [a_x\ a_y\ a_z]$, $\mathbf{a} = [a_1\ a_2\ a_3]$).

Symbols

Symbols (mathematical and physical) used throughout the whole document:

$\mathbb{E}\left[\cdot\right]$	Expected value operator.
$\mathcal{N}(\mu, \sigma)$	Univariate normal distribution, with mean μ and variance σ.
c_0	Speed of light in vacuum, $299\,792\,458\,\mathrm{m\,s^{-1}}$ (approximated to $3 \times 10^8\,\mathrm{m\,s^{-1}}$)

Acronyms

A
ADC analog to digital converter. 19, 22
AoA angle of arrival. 10
API application programming interface. 51
AWGN additive white Gaussian noise. 19

B
BLE Bluetooth Low Energy. 15, 16, 19, 20, 28, 34, 37
BN Batch Normalization. 50
BSA back scatter alignment. 41

C
CP circular polarisation. 67
CRB Cramér-Rao bound. 31, 32
CRC cyclic redundancy check. 20
CSV conventional steering vector. 7, 10, 15, 20, 21, 24–28, 34, 35, 37, 67
CTE constant tone extension. 20

D
DF direction finding. 5, 20, 28
DL Deep Learning. 4, 39, 48, 50, 64, 69
DoA direction of arrival. iii, ix, 2–7, 9–13, 15, 16, 20, 24, 25, 28, 31, 32, 34, 35, 37, 67, 68
DSD drop size distribution. iii, vii, 3, 4, 39–48, 52–64, 68, 69

E
ERP embedded radiation pattern. 4, 7, 15, 16, 20–28, 34, 35, 37, 67, 69

F
FCNN fully connected neural network. iii, ix, 45, 46, 48–50, 57, 64, 69
FOMP Focused Orthogonal Matching Pursuit. 6

G
GELU gaussian-error linear unit. 49, 51

I
iid independent and identically distributed. 19
IQ in-phase and quadrature. 20

L
LHCP left-handed circular polarisation. 16
LN Layer Normalization. 50, 64
LOS line of sight. 17, 18, 21, 22, 24, 28
LR learning rate. 49, 51
LWC liquid water content. 45, 53, 54, 60, 64

M

MAE mean absolute error. 23–28, 32–34
ML machine learning. 45, 48, 68, 69
MLP Multi-Layer Perceptron. 50
MSE mean square error. 32, 49, 51
MTL multi-task learning. 4, 39, 49, 50, 64, 69
MUSIC Multiple Signal Classification. 2, 5–7, 10, 11, 13, 15, 20, 21, 23–28, 34, 67
MVDR Minimum Variance Distortionless Response. 5, 10

N
NLOS non line of sight. 17, 18, 21, 23, 25–28

O
OMP Orthogonal Matching Pursuit. 6

P
PDF probability density function. vii, 44, 52, 53, 55
POD particle orientation distribution. 43, 46, 48, 69

Q
QPE quantitative precipitation estimation. 39

R
ReLU rectified linear unit. 51
RF radio frequency. 67
RHCP right-handed circular polarisation. 16, 67
RMSE root mean square error. 32–34, 68

S
SNR signal-to-noise ratio. 5, 6, 15, 19, 21, 22, 25–28, 35

T
TRGRM two-ray ground-reflection model. 17, 18

U
ULA uniform linear array. 8, 9
URA uniform rectangular array. 8, 9, 16, 18, 21

Introduction

1

1.1 Detect and localise in passive remote sensing . . 2
1.2 Characterise media in active remote sensing . . . 3
1.3 Outline 4

Signal processing lies at the core of modern remote sensing, enabling the transformation of raw sensor data into meaningful information about the Earth's surface and atmosphere. Remote sensing systems acquire data through the measurement of electromagnetic, acoustic, or other types of waves reflected, emitted, or scattered by the target environment. The goal of signal processing in this context is to improve the interpretability of these measurements by filtering noise, enhancing resolution, and extracting features that represent physical, biological, or structural properties of observed objects.

Recent developments in computational power and data-driven methodologies, particularly in machine learning, have significantly expanded the capabilities of remote sensing signal processing. For instance, advanced frequency-domain techniques and deep learning architectures have enabled precise detection and changed the monitoring across complex environments [1].

Feature extraction transforms raw signals into reduced, interpretable descriptors suitable for classification, detection, and estimation. Features can represent physical characteristics (e.g., reflectance spectra, backscatter coefficients), temporal dynamics, or statistical properties of the observed scene. For instance, in optical fibre networks used for passive sensing, feature extraction of reflected optical spectra enables the accurate estimation of environmental parameters such as water levels [2].

In active sensing modalities, features derived from signal phase and amplitude play a crucial role in forming radar or LiDAR images. For example, passive radar imaging using GNSS signals of opportunity relies on sophisticated processing chains to reconstruct target geometries and extract physical features such as ship length or orientation [3].

The effectiveness of feature extraction defines the ultimate success of downstream analytical tasks such as classification or anomaly detection, making it a central challenge in both passive and active sensing workflows.

Remote sensing systems are generally divided into two main categories – passive and active – based on how the signal used for observation is generated.

Passive remote sensing relies on naturally emitted or reflected radiation, such as sunlight or thermal emissions. Examples include optical and infrared imaging sensors used for environmental monitoring.

Active remote sensing, in contrast, employs artificially generated signals, such as radar or LiDAR pulses, to probe the environment. These systems measure the time delay and intensity of the returned signal to estimate distance, shape, and material properties [4].

Recent hybrid systems integrate both approaches to exploit the complementary advantages of each. For example, combining passive satellite imagery with active LiDAR data enhances the characterization of complex ecosystems by linking radiometric and structural information [5].

In some applications, and particularly in the experimental case developed in this thesis, the locator's antenna system detects a signal intentionally emitted by a tag. In this context, the tag is not fully *passive*, but *collaborative*, meaning that the target (i.e. the tag) is not just emitting radiations – as in most of the passive remote sensing scenarios – but actually sends a signal. However, the locator itself is fully passive, as it only detects signals emitted by the tag present in the environment.

1.1 Detection and localisation in passive remote sensing

Detection and localisation are among the most common applications when dealing with passive remote sensing observations, enabling the identification and spatial tracking of targets based on naturally emitted or reflected signals. Unlike active systems that transmit their own energy, passive systems rely on ambient sources such as sunlight, thermal radiation, or environmental acoustic waves. Their advantage lies in stealth, simplicity, and energy efficiency, though they require advanced signal processing to extract meaningful information from often weak and noisy signals.

A key method to perform localisation in passive RF systems is direction of arrival (DoA) estimation. DoA techniques determine the angle at which a signal impinges on a sensor array, allowing triangulation of the target's position when combined with geometric information. These techniques typically rely on beamforming, interferometry, or subspace-based algorithms such as MUSIC and ESPRIT, which exploit the spatial correlation among array elements to estimate incoming signal angles with high precision.

In the RF domain, passive radar sensors have shown that DoA estimation enables precise localisation using ambient electromagnetic fields. Passive radar systems leverage signals of opportunity such as those from Global Navigation Satellite Systems (GNSS) or cellular transmissions. By cross-correlating direct and reflected signal paths, DoA measurements can be used to estimate target positions and trajectories without active illumination. This makes them particularly effective for surveillance, air traffic monitoring, and non-cooperative target tracking [6]. Moreover, DoA estimation in passive RF sensing is being adapted for emerging wireless sensing and situational awareness applications. For instance, passive RF sensor networks can localise transmitters, detect interference sources, or infer environmental properties like building layouts by analysing multi-path DoA patterns. Such methods are central to next-generation spectrum monitoring and remote localisation architectures where passive sensing offers strategic advantages – notably, non-emission-based detection and resilience against jamming or detection.

1.2 Medium characterisation in active remote sensing

Active remote sensing plays a crucial role in characterising the physical and chemical properties of a medium, whether terrestrial, oceanic, or atmospheric. By transmitting controlled electromagnetic or acoustic pulses and analysing their interactions with the environment, active sensors provide precise, quantitative information about material composition, structure, and dynamics. Active remote sensing systems, such as radar, LiDAR, and sonar, enable accurate measurements of topography, vegetation height, ocean salinity, and atmospheric composition. For example, synthetic aperture radar (SAR) and light detection and ranging (LiDAR) systems provide complementary information: while SAR characterises surface roughness and moisture, LiDAR captures vertical structure and elevation, both of which are vital for understanding habitat and terrain morphology [7]. Moreover, active object-detection frameworks in modern remote sensing leverage adaptive algorithms and reinforcement learning to adjust sensing parameters dynamically, thereby improving detection and medium characterisation accuracy under challenging imaging conditions [8]. These systems autonomously optimise illumination and perspective based on environmental feedback, marking a paradigm shift from static observation to interactive environmental interrogation.

An important application of active remote sensing in atmospheric medium characterisation is the retrieval of drop size distribution (DSD), which describes the concentration and size of droplets within a volume of air. Active sensors – particularly radar and lidar – enable remote DSD retrieval by analysing the backscattered power, Doppler velocity, and attenuation of transmitted signals. In fact, dual-frequency and Doppler radar systems provide vertical profiles of raindrop characteristics, including mean diameter, total number concentration, and liquid water content, by exploiting the spectral dependence of radar reflectivity and velocity on drop size. For instance, 94 GHz Doppler radar data combined with lidar observations have been used to retrieve DSD and rain rate using the CAPTIVATE variational algorithm developed for the EarthCARE mission [9]. Similarly, coherent Doppler lidar techniques can separate aerosol and raindrop signals to estimate DSD parameters such as mean drop diameter and fall velocity, showing strong correlation with co-located micro rain radar measurements [10].

1.3 Outline

Here is the outline of this thesis.

Chapter 2 focuses on a general overview related to the direction of arrival (DoA) estimation, introducing the problem and presenting the necessary basic theory. Also, two estimation algorithms are discussed, which are then used in the rest of the thesis to conduct the studies presented.

Chapter 3 presents a novel approach to estimate the DoA by using the embedded radiation patterns (ERPs) of the antenna under test. In particular, using two well-known algorithms, it will be shown that the performance of the sensing system will be enhanced by using the proper physical properties of the receiving antenna.

Chapter 4 discusses the usage of the metrics in the literature related to DoA estimation, by reviewing the most used metrics, and introducing a novel one, capable of measuring more accurately the difference between the true and estimated DoA, due to geometric considerations related to the direction of the incoming wave.

Chapter 5 presents a new method to estimate the drop size distribution (DSD) for a cloud of hydrometeors from polarimetric radar observations by using a DL approach; the designed model retrieves the parameters of the distribution – modelled as a gamma DSD – at the same time, using the principle of multi-task learning (MTL).

Chapter 6 summarises the works and the results reported in the various chapters, providing also some directions for future improvement on the results obtained.

Overview on the Direction of Arrival estimation

2

2.1 Introduction 5
2.2 Array theory 7
2.2.1 Conventional Steering Vectors 10
2.3 Algorithms 10
2.3.1 Bartlett 11
2.3.2 MUSIC 11
2.4 Conclusions 13

This chapter presents an introduction to the problem of the direction of arrival (DoA) estimation. As a widely studied problem, there are many approaches and methods to solve it, many belonging to the more generic direction finding (DF) topic. Most of these approaches are out of the scope of this chapter (and thesis); here, the work is focused on the so-called *subspace-based* algorithms, which identify the directions of the incoming signals by exploiting the properties of the spaces generated by the signals at the receiver's ports and the geometric disposition (and interactions) of the set of sensors used on the receiver (e.g., the *array manifold*). Firstly, the necessary theory that backs these algorithms is analysed, then a summary on this category of algorithms is presented. After that, the algorithms that will be used in the remaining chapters are detailed, namely Bartlett and Multiple Signal Classification (MUSIC).

2.1 Introduction

Direction of arrival (DoA) estimation is a technique in array signal processing, aiming at determining the direction a received signal originates from, generally performed by processing data from multiple antennas or the radiating elements of an antenna array. This problem has been widely studied, finding its way in many applications in different fields, e.g. remote sensing (radar), wireless communication, seismology. Over the years, researchers have developed several algorithms that can be broadly categorized into classical, subspace-based, sparse, and machine learning-based methods.

Classical methods, such as beamforming and Capon's Minimum Variance Distortionless Response (MVDR), rely on spatial filtering techniques to estimate the directions of the incoming signals. These are simple and computationally efficient but often limited by low resolution and sensitivity to noise [11]. To overcome these limitations, subspace-based methods such as the Multiple Signal Classification (MUSIC) and Estimation of Signal Parameters via Rotational Invariance Techniques (ESPRIT) were introduced. These techniques exploit the properties of the signal covariance matrix – mostly eigenvalues and singular values – to achieve high resolution, even under low signal-to-noise ratio (SNR) conditions [12, 13].

In recent years, sparse signal representation and compressed sensing techniques have significantly advanced DoA estimation performance. These approaches reconstruct the spatial spectrum from limited or incomplete measurements, improving resolution and reducing the number of required sensors. Grid-less sparse methods, such as atomic norm minimization and covariance fitting, have been shown to avoid discretization errors and enhance estimation accuracy [14]. The most famous in this category is the Orthogonal Matching Pursuit (OMP) algorithm, which leverages the sparsity of incoming signals within a redundant dictionary to reconstruct the sparse representation of the received data [15]. This was also used as a foundation for developing an on-grid sparse recovery algorithm [16]. Also, there are improved versions, like the Focused Orthogonal Matching Pursuit (FOMP) algorithm [17], which can detect peaks from the angular spectrum even for two adjacent incoming signal sources, even for non-uniform arrays [18], or its application to a Hybrid non-uniform array configuration (HOMP) [19], or its extended version called 3D-OMP [20].

There are also cases in which the estimation performances of the subspace-based algorithms and methods using compressive sensing have been combined [21]. From this analysis it has been inferred that subspace-based methods, like 3D-MUSIC and 3D-ESPRIT [22], have better angular resolution with respect to Compressive sensing methods for small array configurations and a higher number of snapshots; when the array becomes large, compressive sensing performs better.

The integration of machine learning and deep learning has opened a new frontier in DoA estimation. Neural networks, including convolutional and deep architectures, can learn complex signal patterns directly from data, outperforming traditional methods in noisy and non-linear environments [23, 24]. Additionally, novel hybrid systems that combine artificial intelligence with metasurface antennas have demonstrated potential for real-time, high-precision DoA detection in miniaturized systems [25].

Despite the significant progress in processing strategies over the last years, subspace-based algorithms such as MUSIC, Root-MUSIC, and ESPRIT remain the preferred choice in DoA estimation, due to their balance of accuracy, interpretability, and computational feasibility, especially in scenarios with moderate SNR and well-calibrated arrays. When calibration or training data are limited, those subspace-based algorithms maintain superior accuracy and robustness under a broad range of conditions, outperforming newer approaches [26]. Even the new deep learning frameworks for DoA estimation – such as SubspaceNet – embed neural architectures within subspace frameworks rather than replacing them, relying on subspace-based algorithms to leverage interpretability of signal and noise subspaces [27]. Other hybrid models – like TransSubNet and MD-DOA – build upon the theoretical foundations of subspace decomposition while enhancing covariance estimation through deep learning, reinforcing that subspace analysis remains the core computational paradigm for modern DoA estimation [28, 29].

Amongst the many algorithms available at the state of the art, only the subspace-based ones will be addressed here, focusing on two of them, MUSIC and Bartlett. The other types of algorithms are beyond the scope of this thesis.

2.2 Antenna array theory

The subspace-based algorithms perform the DoA estimation relying on the design of the system of receiving antennas when using multiple sensors – being either a network of antennas or an antenna array. In particular, the most important characteristics exploited by these algorithms is the spatial distribution of the various sensors (or elements).

Focusing on the antenna arrays, the concept used to this end is the one related to the *steering vectors* or *array response* (often organised in matrix format). In the following, the array response – either measured or simulated – of the receiver (locator) antenna system is used to synthesise the measured data (snapshots) for a prescribed environment. Some DoA reconstruction algorithms may exploit the array response (or embedded radiation pattern), while others rely solely on the conventional steering vector approach.

Steering vectors

Let us consider a narrowband electromagnetic plane wave with angular frequency ω_0 impinging on an array of M antenna elements located at fixed position vectors $\mathbf{r}_m$ in free space, with $m = 0, \ldots, M-1$. Suppose that the array is in the far field region with respect to the source, thus the electric field at the array can be locally approximated as a uniform plane wave:

$$\mathbf{E}(\mathbf{r}, t) = \Re \left\{ \mathbf{E}_0 \, e^{j\omega_0 t - jk\hat{\mathbf{k}}(\phi,\theta)\cdot\mathbf{r}} \right\} \tag{2.1}$$

where λ is the wavelength, $k = 2\pi/\lambda$ is the wavenumber, and $\hat{\mathbf{k}}(\theta, \phi)$ is the unit vector in the direction of propagation of the incident wave (expressed as depending on the elevation θ and azimuth ϕ angles, as in a spherical reference system), [30]. For a receiving element at position $\mathbf{r}_m$, this wavefront introduces a propagation delay:

$$\tau_m(\phi, \theta) = \frac{1}{c_0} \, \hat{\mathbf{k}}(\phi, \theta) \cdot \mathbf{r}_m \tag{2.2}$$

Under the usual narrowband assumption, where the complex envelope $s(t)$ of the impinging signal varies slowly compared to the carrier, each sensor output can be written in complex baseband form as:

$$x_m(t) \approx s(t)\, e^{-j\omega_0 \tau_m(\phi,\theta)} + n_m(t) = s(t)\, e^{-jk\hat{\mathbf{k}}(\phi,\theta)\cdot\mathbf{r}_m} + n_m(t) \quad (2.3)$$

where $n_m(t)$ denotes additive noise and possible interference at the mth sensor [31].

Stacking the M sensor outputs into a column vector yields the canonical narrowband array model:

$$\mathbf{x}(t) = \begin{bmatrix} x_0(t) \\ x_1(t) \\ \vdots \\ x_{M-1}(t) \end{bmatrix} = \mathbf{a}(\phi,\theta)\, s(t) + \mathbf{n}(t), \quad (2.4)$$

where $\mathbf{n}(t)$ is the noise vector and

$$\mathbf{a}(\phi,\theta) = \begin{bmatrix} e^{-jk\,\hat{\mathbf{k}}(\phi,\theta)\cdot\mathbf{r}_0} \\ e^{-jk\,\hat{\mathbf{k}}(\phi,\theta)\cdot\mathbf{r}_1} \\ \vdots \\ e^{-jk\,\hat{\mathbf{k}}(\phi,\theta)\cdot\mathbf{r}_{M-1}} \end{bmatrix} \in \mathbb{C}^M \quad (2.5)$$

is called the *steering vector* – or array manifold vector – associated with direction (ϕ, θ) [32, 33], collecting the relative phase shifts experienced by the plane wave propagating in that direction at the different array elements' ports.

ULA and URA cases

Two simple and important special cases are the steering vectors of a uniform linear array (ULA) and of a uniform rectangular array (URA). A ULA has M identical elements with inter-element spacing d, arranged along the x axis. Their position is referenced with respect to the first element ($m = 0$), which lies at the origin of the reference system; thus, $\mathbf{r}_m = md\,\hat{\mathbf{x}}$. If θ denotes the angle of arrival measured from broadside in the (x, z) plane, then $\hat{\mathbf{k}}(\theta) = \sin\theta\hat{\mathbf{x}} + \cos\theta\hat{\mathbf{z}}$ and

$$\hat{\mathbf{k}}(\theta)\cdot\mathbf{r}_m = md\sin\theta.$$

Inserting this into Equation 2.5 gives the familiar ULA steering vector:

$$\mathbf{a}(\theta) = \begin{bmatrix} 1 \\ e^{-jkd\sin\theta} \\ e^{-j2kd\sin\theta} \\ \vdots \\ e^{-j(M-1)kd\sin\theta} \end{bmatrix}, \tag{2.6}$$

which depends only on the element spacing, the wavelength, and the direction of arrival.

The derivation for the URA is similar; the M identical elements form a rectangular with dimensions M_x on the x axis and M_y on the y axis, resulting in $M = M_x \times M_y$. The inter-element spacings along both axes are d_x and d_y, respectively. The first element lies at the origin, with $m_x = m_y = 0$. Following the result for the ULA, and considering that here two angles need to be taken into account (θ and ϕ), the steering vector for the URA is:

$$a(\phi, \theta, m_x, m_y) = e^{-jk\sin\theta\left[m_x d_x \cos\phi + m_y d_y \sin\phi\right]} \tag{2.7}$$

where $m_x = 0, \ldots, M_x - 1$ and $m_y = 0, \ldots, M_y - 1$ and $\mathbf{a}(\phi, \theta) \in \mathbb{C}^{(M_x \times M_y) \times 1}$.

Applications

The steering vector plays a central role in array processing during both transmission and reception; as an example, when using the array to receive signals, a linear beamformer forms the scalar output

$$y(t) = \mathbf{w}^{\mathrm{H}}\mathbf{x}(t)$$

and the same steering-vector formalism governs the spatial filtering properties of $\mathbf{w}$, with many classical and modern DoA and beamforming algorithms expressed directly in terms of $\mathbf{a}(\phi, \theta)$ and its collection over angles, the so-called *array manifold* [31–33].

In practical systems, the steering vector also provides the parametric link between the physical array geometry and the statistical data model. In the presence of K narrowband sources with waveforms $s_k(t)$ arriving from directions (ϕ_k, θ_k), the snapshot vector generalizes Equation 2.4 to

$$\mathbf{x}(t) = \sum_{k=1}^{K} \mathbf{a}(\phi_k, \theta_k)\, s_k(t) + \mathbf{n}(t) = \underline{\mathbf{A}}(\boldsymbol{\phi}, \boldsymbol{\theta})\, \mathbf{s}(t) + \mathbf{n}(t) \tag{2.8}$$

where

$$\underline{\mathbf{A}}(\boldsymbol{\phi}, \boldsymbol{\theta}) = \left[\mathbf{a}(\phi_1, \theta_1), \ldots, \mathbf{a}(\phi_K, \theta_K)\right] \tag{2.9}$$

is the *steering matrix* and $\mathbf{s}(t)$ collects the source signals. This narrow-band array model underlies classical beamforming, Capon/MVDR processing, subspace methods such as MUSIC and ESPRIT, and many contemporary sparse-reconstruction approaches [31–33].

2.2.1 Conventional Steering Vectors

The conventional steering vectors (CSVs) approach refers to the use of ideal analytically-derived steering vectors to perform the reconstruction of the array response. These are computed only from the nominal array geometry and the operating frequency, considering a simple plane-wave (in far-field); moreover, some assumptions are made:

- the array elements are identical and perfectly calibrated;
- mutual coupling between elements is negligible;
- the element patterns are either isotropic or known but separable from the array factor;
- the propagation medium is homogeneous and lossless.

Under these assumptions, the *conventional* steering vector $\mathbf{a}_{\mathrm{CSV}}(\phi, \theta)$ is equal to the one in Equation 2.5 and it is used directly in both beamforming and DoA estimation algorithms [31]. For example, in the Bartlett algorithm for DoA estimation, as defined in Subsection 2.3.1, the spatial pseudo-spectrum is given by:

$$P_{\mathrm{B}}(\phi, \theta) = \mathbf{a}_{\mathrm{CSV}}^{\mathrm{H}}(\phi, \theta)\, \underline{\mathbf{R}}_{\mathbf{x}}\, \mathbf{a}_{\mathrm{CSV}}(\phi, \theta) \tag{2.10}$$

where $\underline{\mathbf{R}}_{\mathbf{x}}$ is the sample-averaged covariance matrix of $\mathbf{x}(t)$, and scanning (ϕ, θ) over the field of view – or the entire array manifold.

2.3 Algorithms

Amongst all the DoA estimation algorithms, here only Bartlett and Multiple Signal Classification (MUSIC) will be covered. Both require, as first step, the estimation of the covariance matrix. MUSIC, starting from this matrix, estimates the eigenvectors of the noise space and uses them to filter out the Angles of Arrival (AoAs) related to noise, returning a pseudo-spectrum. Bartlett, instead, does not isolate the noise directions, providing a lower resolution than Schmidt's MUSIC algorithm [34].

2.3.1 Bartlett

Let us start from the situation described by Equation 2.8, but considering M sensors and D incoming signals from different directions (ϕ_d, θ_d), with $d = 0, \ldots, D-1$. Equation 2.8 can be rewritten as

$$\mathbf{x}(k) = \underline{\mathbf{A}}(\boldsymbol{\phi}, \boldsymbol{\theta})\, \mathbf{s}(k) + \mathbf{n}(k) \tag{2.11}$$

where k is the time sample, $\mathbf{x}(k) \in \mathbb{C}^M$ is the array snapshot, $\mathbf{s}(k) \in \mathbb{C}^D$ collects the source signals, $\mathbf{n}(k)$ is additive noise and $\underline{\mathbf{A}}(\boldsymbol{\phi}, \boldsymbol{\theta})$ is the steering matrix, as defined in Equation 2.9. Given K snapshots, the sample-averaged covariance matrix of the array data is:

$$\underline{\mathbf{R}}_{\mathbf{x}} = \frac{1}{K} \sum_{k=1}^{K} \mathbf{x}(k)\, \mathbf{x}^{\mathrm{H}}(k) \tag{2.12}$$

Most classical DoA estimators, including Bartlett and MUSIC, operate on $\underline{\mathbf{R}}_{\mathbf{x}}$ and differ in how they construct a spatial spectrum from it.

The Bartlett (or conventional beamformer) forms, for each direction (ϕ, θ) in the array manifold, a spatial filter with weight vector $\mathbf{w}_B(\phi, \theta)$ proportional to the steering vector (up to a scalar normalization). The output power of this beamformer is:

$$P_B(\phi, \theta) = \mathbf{w}_B^{\mathrm{H}}(\phi, \theta)\, \underline{\mathbf{R}}_{\mathbf{x}}\, \mathbf{w}_B(\phi, \theta) \;\propto\; \mathbf{a}^{\mathrm{H}}(\phi, \theta)\, \underline{\mathbf{R}}_{\mathbf{x}}\, \mathbf{a}(\phi, \theta) \tag{2.13}$$

The Bartlett spatial spectrum $P_B(\phi, \theta)$ is then scanned as a function of ϕ and θ; peaks in this spectrum are interpreted as DoA estimates.

Generally, the Bartlett spectrum exhibits relatively high sidelobes, so strong interferers or noise can mask weaker sources. On the other hand, the method is conceptually simple, computationally inexpensive, and robust to modest model mismatches, which makes it a useful baseline and a natural starting point for more sophisticated DoA estimators [31, 32].

2.3.2 MUSIC

The Multiple Signal Classification (MUSIC) algorithm, introduced by Schmidt in the mid-1980s [34], offers a dramatic improvement in angular resolution by exploiting the eigenvalues of the array covariance matrix. Under the standard assumptions of narrowband, far-field sources, spatially white noise (Equation 2.8), and a number of sensors M strictly larger than the number of sources D, the ensemble covariance of the array output is:

$$\underline{\mathbf{R}}_{\mathbf{x}} = \mathbb{E}\left[\mathbf{x}(k)\,\mathbf{x}^{\mathrm{H}}(k)\right] = \underline{\mathbf{A}}(\boldsymbol{\phi},\boldsymbol{\theta})\,\underline{\mathbf{R}}_{\mathbf{s}}\,\underline{\mathbf{A}}^{\mathrm{H}}(\boldsymbol{\phi},\boldsymbol{\theta}) + \sigma_n^2\,\underline{\mathbf{I}}_M \tag{2.14}$$

where $\underline{\mathbf{R}}_{\mathbf{s}}$ is the source sample-averaged covariance matrix and $\sigma_n^2\,\underline{\mathbf{I}}_M$ models spatially white noise.

The key insight of MUSIC is that $\underline{\mathbf{R}}_{\mathbf{x}}$ admits an eigen-decomposition such as:

$$\underline{\mathbf{R}}_{\mathbf{x}} = \underline{\mathbf{U}}_{\mathbf{s}}\,\underline{\boldsymbol{\Lambda}}_{\mathbf{s}}\,\underline{\mathbf{U}}_{\mathbf{s}}^{\mathrm{H}} + \underline{\mathbf{U}}_{\mathbf{n}}\,\underline{\boldsymbol{\Lambda}}_{\mathbf{n}}\,\underline{\mathbf{U}}_{\mathbf{n}}^{\mathrm{H}} \tag{2.15}$$

where the D largest eigenvalues in $\underline{\boldsymbol{\Lambda}}_{\mathbf{s}}$ and their eigenvectors in $\underline{\mathbf{U}}_{\mathbf{s}}$ span the signal subspace, and the remaining $M-D$ equal eigenvalues – all equal to σ_n^2 in the ideal model – and associated eigenvectors in $\underline{\mathbf{U}}_{\mathbf{n}}$ span the noise subspace. When a steering vector corresponds to a true DoA, it lies entirely in the signal subspace, thus being orthogonal to the noise subspace:

$$\underline{\mathbf{U}}_{\mathbf{n}}^{\mathrm{H}}\,\underline{\mathbf{a}}(\phi_d,\theta_d) = \mathbf{0}\,, \qquad i = 0,\ldots,D-1. \tag{2.16}$$

In practice, $\underline{\mathbf{R}}_{\mathbf{x}}$ is replaced by its sample estimate $\hat{\underline{\mathbf{R}}}_{\mathbf{x}}$, which is then eigen-decomposed numerically. Once an estimate of the number of sources $\hat{D}$ is available, the $M-\hat{D}$ eigenvectors associated with the smallest eigenvalues are collected into $\hat{\underline{\mathbf{U}}}_{\mathbf{n}}$, an estimate of the noise subspace. MUSIC defines the pseudo-spectrum:

$$P_{\mathrm{MUSIC}}(\phi,\theta) = \frac{1}{\mathbf{a}^{\mathrm{H}}(\phi,\theta)\,\hat{\underline{\mathbf{U}}}_{\mathbf{n}}\,\hat{\underline{\mathbf{U}}}_{\mathbf{n}}^{\mathrm{H}}\,\mathbf{a}(\phi,\theta)} \tag{2.17}$$

For a direction (ϕ,θ) close to a true DoA, the steering vector $\mathbf{a}(\phi,\theta)$ becomes nearly orthogonal to the estimated noise subspace, so the denominator in Equation 2.17 is small and the pseudo-spectrum exhibits a sharp peak. By locating these peaks, one obtains high-resolution DoA estimates, often capable of resolving sources separated by less than a conventional beamwidth [32, 34].

Compared to the Bartlett spectrum, the MUSIC pseudo-spectrum typically has much narrower peaks and greatly reduced sidelobes, enabling more accurate discrimination of closely spaced sources and weaker emitters in the presence of strong interferers. However, this gain in resolution comes at the price of higher computational complexity, a need to estimate the number of sources, and increased sensitivity to model mismatches such as calibration errors, array perturbations, coherent multipath, or coloured noise. When sources are highly correlated or coherent, preprocessing techniques such as spatial smoothing are often required to restore the rank conditions assumed by MUSIC.

In summary, the Bartlett beamformer can be interpreted as a classical spatial spectral estimator whose resolution is fundamentally limited by the physical aperture, while MUSIC is a subspace-based method that leverages the structure of the array covariance matrix to achieve super-resolution under suitable conditions. Both algorithms play a central role in the theory and practice of DoA estimation and serve as canonical examples of, respectively, conventional and high-resolution array processing techniques.

2.4 Conclusions

Here, an overview about the DoA estimation problem was given, by showing the theory behind it and the various methods that have been developed through the years, as the topic is well established in the literature. The presented theory and algorithms' detailed explanations will be used in the following chapters, which deal with two precise aspects of this problem.

Embedded Radiation Patterns for Direction of Arrival estimation

3

3.1 Introduction 15
3.2 System model 16
3.3 Detection and localisation 20
3.3.1 Detection 20
3.3.2 Localisation 20
3.4 Localisation performance evaluation . . . 21
3.4.1 Antenna array size . . 22
3.4.2 Array reconstruction method 24
3.4.3 Snapshots number . . 25
3.5 Conclusions 28

This chapter is dedicated to the analysis of performance in DoA estimation by using the embedded radiation patterns (ERPs) of the locator antenna. This method was applied to an indoor positioning application and implemented on top of the Bluetooth Low Energy (BLE) standard, where a system of receiving antennas works as a locator. The aspect related to signal processing and the antenna array modelling are very similar to a DoA application for remote sensing; the detection part may be different (since detection is performed by the BLE protocol), but the localisation – i.e. DoA estimation – is equal.

The performance analysis of the algorithms (mostly MUSIC) is conducted by a) changing the inter-element spacing of the receiving antenna array, b) comparing conventional steering vector (CSV) approach and the newly proposed embedded radiation pattern (ERP) approach, c) reducing the number of snapshots.

3.1 Introduction

Subspace-based algorithms are the most common algorithms used in DoA estimation, mainly due to their ability to achieve high angular resolution – even under low SNR conditions – without requiring extensive array calibration [35]. The input data for these algorithms is the spatial covariance matrix derived from the received signals, containing both the wanted and the unwanted signals – generally noise and unwanted echos of the true signals. To achieve good performances with these algorithms, part of the input data must be modelled very precisely; since the signal is generally unknown, this task is heavily related to the modelling of the antenna array used in reception.

Modelling the antenna array means to analyse how each element of the array responds to a certain input. Traditionally, this response is represented through conventional steering vectors (CSVs), assuming simplified conditions about the elements gains and neglecting their inter-element coupling – basically treating them as idealised isotropic radiators with uniform gain. Although simple, a CSV-based approach can introduce significant modelling errors when the inter-element interactions cannot be ignored [36]. Such inaccuracies lead to distortions between the ideal and actual array responses, degrading the performances of these algorithms. Many tried to mitigate these effects – e.g., deriving from inter-element coupling, or mutual coupling – by computing them and taking them into account when dealing with linear arrays of dipoles [37, 38] or with spherical antenna arrays [39–41].

A valid solution to these problems can be the usage of embedded radiation patterns (ERPs), which consist in the true electromagnetic responses of each antenna element, thus automatically including the various effects due to the geometry and the building of the antenna array, such as mutual coupling, loading effects, and radiation nonidealities. This leads to a broader approach in dealing with these different effects, instead of taking care of them separately.

3.2 System model

To perform the DoA estimation, three models need to be considered:

- The physical model of the receiving antenna array;
- The mathematical model related to the propagation of the signals in an indoor environment;
- The determination of the incoming signals' model, which combines true signals and noise.

Antenna array

The receiver (or locator) is a uniform rectangular array (URA) with 9 octagonal microstrip patch antennas, working in right-handed circular polarisation (RHCP) [42]. This polarisation was chosen because it is not – or slightly – affected by signal degradation that may be caused by a) bad weather conditions and b) the relative orientation between the transmitting and receiving antennas [43, 44]. Also, this polarisation makes the antenna naturally reject the odd reflections from the environment; this is due to the way circular polarised waves are reflected. If a RHCP wave is reflected by a perfect electric conductor (PEC), it becomes LHCP after reflection (and vice versa). For a dielectric interface, this is not necessarily the case: a RHCP wave does not in general become perfectly LHCP upon reflection. The resulting polarisation depends on the incidence angle, the permittivity contrast, and the Fresnel coefficients. Only in special situations – such as grazing incidence or strong dielectric contrast – can the reflected wave approach the opposite handedness.

Signals' propagation

The mathematical model adopted to describe the signal propagation accounts only for coherent reflections of the useful signal, since the filtering chain implemented in the BLE receiver is capable of avoiding the non-coherent power of adjacent channels, making those unwanted signals negligible. Therefore, all interfering signals in this formulation arise from reflections (coherent interferences) of the useful signal itself. Considering an indoor environment, there may be more than one reflection reaching the receiving antenna: generally, the dominant reflection is from the ground, then the one from the roof, then reflections from unintentional reflectors placed sideways to the path, and finally also reflections from obstacles behind the receiver.

To model such a propagation environment with an appropriate relative power P_i, the two-ray ground-reflection model (TRGRM) is exploited for each reflection. Considering the position of the receiver and the target in the indoor environment, the lateral walls can be identified depending on their position with respect to both:

- *rear wall*, the one closest to the back of the target and that stands behind it;
- *front wall*, the one opposite to the *rear wall* (closer to the receiver).
- *right wall*, the one that is on the right when looking at the receiver from the *rear wall*;
- *left wall*, the one that is on the left when looking at the receiver from the *rear wall*;

Let us suppose that r is the line of sight (LOS) distance between the target and the receiver, h_l is the height of the receiver, h_t is the height of the target, h_r is the height of the indoor environment (like in a room, this is the distance between the ground and the ceiling), d_t and d_l are the horizontal distances from one of the walls to the target and the receiver, respectively. d_w is the distance between lateral walls. This situation is displayed in Figure 3.1.

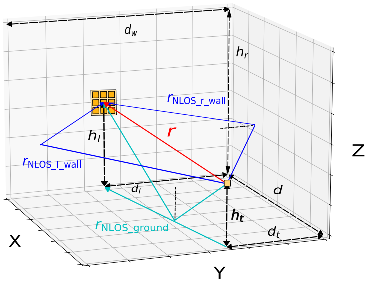

Figure 3.1: Propagation model for an indoor environment with the TR-GRM applied to the walls and the ground. The line of sight (LOS) path is shown by a solid red line, while the non line of sight (NLOS) paths are shown as solid lines in blue (walls) and light blue (ground). The dashed black lines denote the various heights and distances, while the small dotted-dashed lines (located near the surface where the reflection happens) represent the normal direction with respect the related surface.

The LOS distance, r, between the target and the receiver can be calculated as:

$$r = \sqrt{d^2 + |h_t - h_l|^2 + |d_t - d_l|^2} \tag{3.1}$$

The non line of sight (NLOS) wave paths reflected by the ground (NLOS_ground), ceiling (NLOS_roof) and walls (NLOS_r_wall, NLOS_l_wall) can be expressed as:

$$\begin{aligned} r_{\text{NLOS\_ground}} &= \sqrt{r^2 + 4h_t h_l} \\ r_{\text{NLOS\_roof}} &= \sqrt{r^2 + 4(h_r - h_t)(h_r - h_l)} \\ r_{\text{NLOS\_r\_wall}} &= \sqrt{r^2 + 4d_t d_l} \\ r_{\text{NLOS\_l\_wall}} &= \sqrt{r^2 + 4(d_w - d_t)(d_w - d_l)} \end{aligned} \tag{3.2}$$

Equation 3.1 and Equation 3.2 simply incorporate the Euclidean distance in the model depicted in Figure 3.1. For the sake of brevity, we introduce the following notation, which will be used throughout the rest of the chapter:

$$r_{\mathrm{NLOS,d}} \in \left\{ r_{\mathrm{NLOS\_ground}}, r_{\mathrm{NLOS\_roof}}, r_{\mathrm{NLOS\_l\_wall}}, r_{\mathrm{NLOS\_r\_wall}} \right\} \tag{3.3}$$

Then, by using the TRGRM and assuming the target to be a nearly isotropic radiator, the relation between the LOS path loss L_{LOS} of the direct signal and the NLOS path loss $L_{\mathrm{NLOS,d}}$ due to the reflected signals is given by the Friis formula for radio links in decibel:

$$L_{\mathrm{NLOS,d}} = L_{\mathrm{LOS}} + 10\log_{10}\left(\frac{r}{r_{\mathrm{NLOS,d}}}\right)^2 + 10\log_{10}|\Gamma_{\mathrm{W}}| \tag{3.4}$$

where $|\Gamma_{\mathrm{W}}|$ is the reflection coefficient of the sidewalls, assuming it to be a random value varying within the interval 0.2 to 0.6. This coefficient can incorporate polarisation mismatch losses, which can be evaluated by adding the logarithm term in the equation above. Hence, the power of the signal arriving from the direction d can be expressed as:

$$P_d = \begin{cases} P_0 = P_t + L_{\mathrm{LOS}}, & \text{for LOS signal} \\ P_{\mathrm{NLOS}} = P_t + L_{\mathrm{NLOS}}, & \text{for NLOS signals} \end{cases} \tag{3.5}$$

where P_t is the radiated power emitted by the tag.

The resulting model is a typical statistical model for one incoming signal and its reflections; to do this, some assumptions were made:

- the usage of circular polarisation significantly reduces the power received from odd reflections (since the power received is affected by large polarisation mismatch losses);
- $h_r = h_t + h_l$;
- $dw = dt + dl$.

Signals' model

The response of the URA to the $D + 1$ impinging signals at a specific nth snapshot is described by the array response matrix (or *steering vector matrix*):

$$\underline{\mathbf{A}} = \left[a(\phi_0, \theta_0), \dots, a(\phi_i, \theta_i), \dots, a(\phi_D, \theta_D) \right] \in \mathbb{C}^{M \times (D+1)} \tag{3.6}$$

where $i = 1, \dots, D$ is the index of one of the incoming signals and M is the number of elements in the antenna array. $\mathbf{a}(\phi_d, \theta_d) \in \mathbb{C}^{M\times 1}$ is the column vector containing the response of the M elements of the array due to the signal arriving from direction $d \leftrightarrow (\phi_d, \theta_d)$ [1]; $d = 0$ identifies the useful LOS signal.

[1] These angles refer to a spherical reference system; thus, ϕ is the *azimuthal* angle (or *azimuth*), and θ is the *polar angle*, which is defined as $\theta = 90 - \theta_{\mathrm{el}}$, where θ_{el} is the *elevation* angle.

The baseband samples at the BLE receiver, running at a proper sample period T_s without ADC impairments can be expressed as:

$$\underline{\mathbf{X}}_{\mathbf{ADC}} = \underline{\mathbf{A}}\,\underline{\mathbf{E}}\,\underline{\mathbf{S}} + \underline{\mathcal{N}} \ \in \mathbb{C}^{M \times N} \tag{3.7}$$

where $\underline{\mathbf{A}}$ is the array response matrix seen above. $\underline{\mathbf{E}}$ is the matrix considering the path loss for each impinging signal, and it is defined as:

$$\underline{\mathbf{E}} = E_d e^{j\Delta_d} \underline{\mathbf{I}} = \begin{bmatrix} E_0 & 0 & \cdots & 0 \\ 0 & E_1 e^{j\Delta_1} & \cdots & 0 \\ \vdots & 0 & \ddots & \vdots \\ 0 & 0 & \cdots & E_D e^{j\Delta_D} \end{bmatrix}, d = 0, \ldots, D \tag{3.8}$$

with $E_d \propto \sqrt{P_d}$ used to consider the relative amplitude of the d impinging signal – incorporating possible polarisation mismatch losses – and Δ_d being the phase shift of the dth signal due to its propagation (with reflections or not). $\underline{\mathbf{S}}$ is the matrix containing the signals with normalised amplitude (with respect to its contribution to the received power, P_d):

$$\underline{\mathbf{S}} = \begin{bmatrix} s_{01} & s_{02} & \cdots & s_{0N} \\ s_{11} & s_{12} & \cdots & s_{1N} \\ \vdots & \vdots & \ddots & \vdots \\ s_{D1} & s_{D2} & \cdots & s_{DN} \end{bmatrix} \in \mathbb{C}^{(D+1) \times N} \tag{3.9}$$

where N is the number of samples. $\underline{\mathcal{N}}$ is the noise matrix, which is modelled as additive white Gaussian noise (AWGN):

$$\underline{\mathcal{N}} = \begin{bmatrix} n_0 \\ n_1 \\ \vdots \\ n_D \end{bmatrix} = \begin{bmatrix} n_{01} & n_{02} & \cdots & n_{0N} \\ n_{11} & n_{12} & \cdots & n_{1N} \\ \vdots & \vdots & \ddots & \vdots \\ n_{D1} & n_{D2} & \cdots & n_{DN} \end{bmatrix} \in \mathbb{R}^{M \times N} \tag{3.10}$$

where n_m is the AWGN for the mth antenna element port, which is independent and identically distributed (iid) and drawn from $\mathcal{N}(0, \sigma^2)$, with σ^2 related to the SNR.

The matrix $\underline{\mathbf{X}}_{\mathbf{ADC}}$ previously defined in Equation 3.7, needs to be low-pass filtered and downsampled to F_{IQ} – during the sampling process of the incoming signal – to obtain the matrix $\underline{\mathbf{X}}$, with dimensions $M \times N$.

3.3 Detection and localisation

Applications performing localisation of targets generally require the detection task to be executed before actually working to localise the target. In this specific application:

- the detection is performed by using the BLE protocol, using a feature called constant tone extension (CTE);
- the localisation phase is performed by the DoA estimation algorithms.

3.3.1 Detection

DF via Bluetooth was made possible by introducing the CTE at the end of a BLE packet. It consists of a sequence of alternating switch and sample slots, each with a duration of either 1 µs or 2 µs, as specified by the host [45].

The CTE has a variable length between 16 µs and 160 µs. During the in-phase and quadrature (IQ) sampling process, the BLE receiver extracts only CRC-valid packets. Considering the *switch* slot duration T_{switch} and the *sampling* slot duration T_{sample}, the receiver extracts IQ samples during the CTE sample slots at the frequency $F_{IQ} = 1/(T_{switch} + T_{sample})$.

As said in Section 3.2, these IQ samples are arranged in a matrix, labelled $\underline{\mathbf{X}}$. This matrix has M rows and N columns – with M the number of elements in the array and N the number of samples for each antenna. Each column can be referred to as a *snapshot*. The $\underline{\mathbf{X}}$ matrix is the input data for the DoA algorithm to perform the localisation phase. The maximum number of snapshots that can be obtained is $N = 80$, when the CTE length in time is set equal to 160 µs, with $T_{switch} = T_{sample} = 1$ µs.

3.3.2 Localisation

The localisation phase is performed by using two DoA estimation algorithms, namely Bartlett and MUSIC [2]. Bot of them require the reconstruction of the array response for all the different possible directions of incoming signals. For this task, two approaches are considered: CSV and ERP.

For both the approaches, the array response is sampled for different discrete directions of arrival (ϕ, θ) in 3D space; thus, the steering matrix used in the estimation algorithms (Equation 2.9) has dimensions $M \times L$, with M the number of sensors (which is nine) and L the number of directions obtained by varying ϕ and θ. The total

[2] Since MUSIC is a reference model in DoA estimation, it is still used here alongside the conventional Bartlett beamformer, despite the well-known fact that MUSIC does not perform well with coherent signals.

field of view analysed by the algorithms is achieved by sweeping ϕ from 0° to 359° and θ from 0° to 180°, with 1° resolution. In the end, $L = 65160$.

The CSV approach starts from the analytical definition of the steering vectors for a URA, as written in Equation 2.7, with $m_x, m_y \in \{0, 1, 2\}$, since the array is a 3×3 URA, and ϕ and θ varying in the L aforementioned directions.

In this application, to use the ERP approach, the steering vectors are evaluated from the radiation patterns calculated by full-wave simulations, which consider the various effects on the generated pattern due to the geometry of the array. Amongst the several advantages, this method can also be applied in a more compact version of the array with very closely spaced elements, where the oversimplified CSV approach falls short.

The resulting steering matrix is then fed to both of the algorithms to compute the pseudo-spectra for each of the L directions, as seen in Equation 2.13 and Equation 2.17. The estimated directions of arrival are given by the combinations of (ϕ, θ) where the pseudo-spectrum has a peak.

3.4 Localisation performance evaluation

The effectiveness of the mathematical model presented in Section 3.2 was tested in different scenarios, obtained by changing:

- the size of the receiving antenna array (by changing their inter-element distance);
- the method for reconstructing the array response, i.e. CSV or ERP;
- the number of snapshots;

Extensive numerical analysis has been carried out by considering realistic 3D ERPs from the antenna design in [42], where the ERPs were obtained either from measurements on a real locator prototype or from full-wave simulations in *ANSYS HFSS*. Only the locator with spacing $d = \lambda/2.5$ was fabricated and measured. The pattern measurements show that the simulated and measured ERPs are in good agreement, thereby justifying the use of simulated patterns for the other spacings as well.The performances of MUSIC and Bartlett algorithms have been tested by considering only the incident signal (LOS) or both the incident signal and two NLOS interfering signals, by varying the SNR of the system.

3.4.1 Antenna array size

The aim of this first step is to find a balance between antenna miniaturization and accuracy of the estimation.

To perform this analysis, a statistical model for the incoming signals was generated and stored, allowing the comparison between the performances of different layouts. The ranges for the considered angles of arrival are: $\theta \in [0°, 85°]$ for elevation and $\phi \in [0°, 360°]$ for the azimuth. The SNR is referred to the ADC frequency, F_{ADC}, and to the received power of the LOS path, P_0. Cases with 80, 8, and 1 snapshots have been simulated, where 8 snapshots correspond to 1 packet. For these tests, the distance between the receiver and the target, r, has been chosen randomly in the range from 1 m to 9 m. The selected distance between the ceiling and the floor, h_r, has been taken equal to 4 m, while the distance between the walls, d_w, has been randomly chosen up to 6 m. Moreover, the reflection coefficient of the materials, Γ_W, has been chosen randomly in the interval 0.2 to 0.6.

To effectively evaluate the performances of various antenna layouts through extensive numerical analysis, all the comparisons have been made by assuming the same incoming signal statistics, thus under equal conditions. To obtain a better configuration in terms of tracking accuracy and miniaturisation, three array structures have been taken into account, with a over-wavelength-normalised inter-element distance d/λ of 0.5, 0.4, and 0.35, respectively. For these scenarios, the ERP approach was used to account for mutual coupling effects and gain loss due to miniaturization.

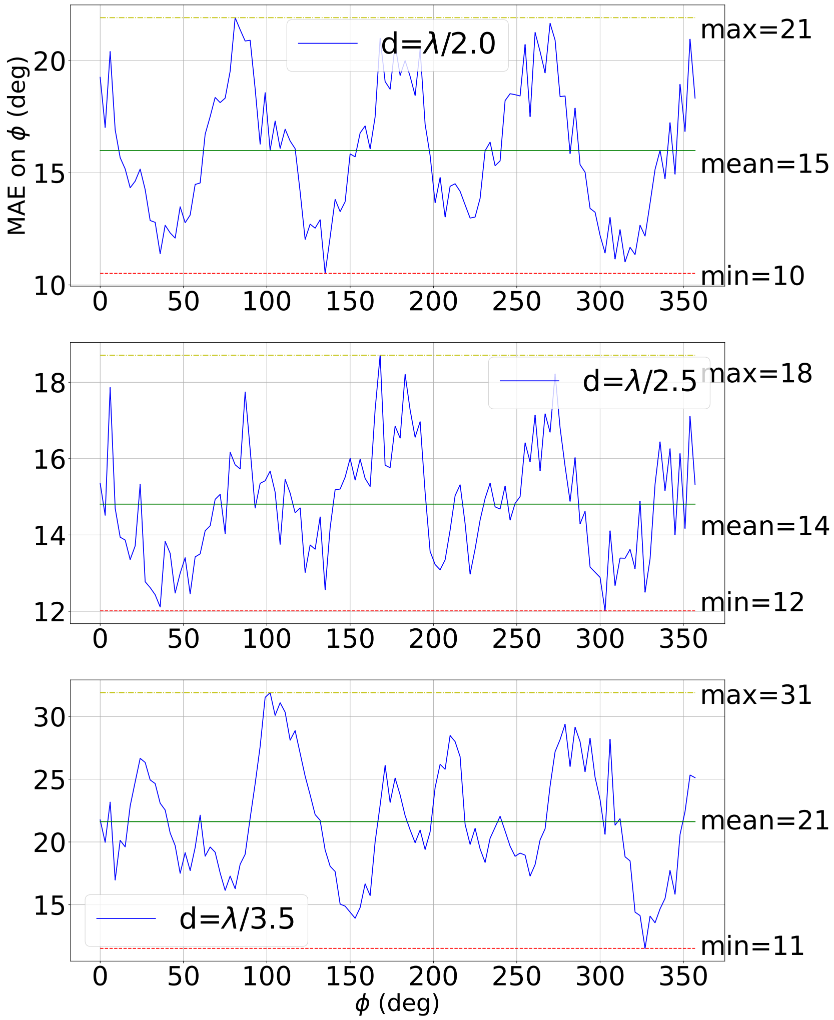

Figure 3.2: Impact of inter-element distance d with 2 NLOS and ERP approach. MAE applied to the results of the MUSIC algorithm, with 1° resolution on azimuth ϕ. The MAE analysis reveals more accurate estimates (minimum, mean, maximum) across the azimuthal range ϕ when the $d = \lambda/2.5$ spacing is chosen.

As shown in Figure 3.3, a reduction in size of 20 % and 30 % is achieved by moving from (a) to (c). However, this size reduction also results in a significant decrease in gain. Specifically, the gain drops from 3.4 dB for a single radiator at 2.44 GHz in the 3×3 array with a $d = \lambda/2$ spacing, to 2 dB for a $d = \lambda/2.5$ spacing, and 0.5 dB for a $d = \lambda/3.5$ spacing.

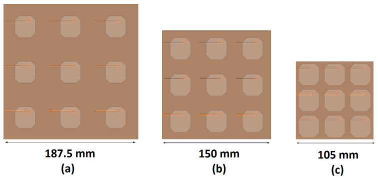

Figure 3.3: 3×3 array configurations with different inter-element distances: (a) $d = \lambda/2$, (b) $d = \lambda/2.5$, (c) $d = \lambda/3.5$. Over these values, the estimation tests were conducted, to find the best trade-off between tracking accuracy and miniaturisation. By reducing the size of the array, a substantial decrease in gain is observed, passing from 3.4 dB in case (a) to 0.5 dB in case (c).

The mean absolute error (MAE) served as the performance metric to assess the accuracy of the estimation for the main direction of arrival. MAE represents the average absolute error between the true angle of arrival (ground truth), and its estimation, averaged over N measurements. MAE can be calculated individually for the elevation, θ, and for the azimuth, ϕ. The definition of MAE over θ is the following, as seen in [46]:

$$\mathrm{MAE}_\theta = \frac{1}{N}\sum_n \left|\theta_n - \hat{\theta}_n\right| \tag{3.11}$$

The MAE over ϕ has been estimated by exploiting the concept of direction cosines; namely, true and estimated directions along the azimuthal plane are associated to their unit vectors, $\mathbf{u}$ and $\hat{\mathbf{u}}$ (see Figure 3.4):

$$\begin{aligned} \mathbf{u} &= \cos\phi\,\hat{\mathbf{u}}_x + \sin\phi\,\hat{\mathbf{u}}_y \\ \hat{\mathbf{u}} &= \cos\hat{\phi}\,\hat{\mathbf{u}}_x + \sin\hat{\phi}\,\hat{\mathbf{u}}_y \end{aligned} \tag{3.12}$$

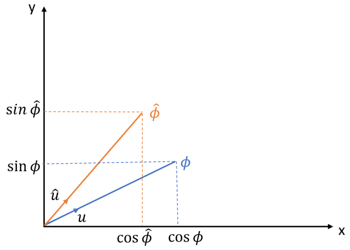

Figure 3.4: MAE estimation in the ϕ plane. By adopting the direction cosines approach, the geometric angle between the two unit vectors $\mathbf{u}$ and $\hat{\mathbf{u}}$ is calculated.

thus the MAE can be computed as:

$$\begin{aligned} \mathrm{MAE}_\phi &= \frac{1}{N}\sum_n \arccos\left(\cos\phi_n\cos\hat{\phi}_n + \sin\phi_n\sin\hat{\phi}_n\right) \\ &= \frac{1}{N}\sum_n \arccos\left[\cos(\hat{\phi}_n - \phi_n)\right] \end{aligned} \tag{3.13}$$

where N is the number of trials. The definition presented in Equation 3.13 is equivalent to the one in [46], with the notable difference that it effectively incorporates the periodicity of ϕ every 2πrad or 360°.

Results for the error in the azimuth (ϕ) plane are presented in Figure 3.2. The analysis reveals that the $d = \lambda/2.5$ configuration yields the highest accuracy based on the minimum, mean, and maximum MAE values.

Considering the results for MAE over elevation θ, as illustrated in Figure 3.5, a large increase of MAE for high values of θ is observed, due to the negligible gain of patch antennas at such angles.

As a result of the MAE analysis over θ and ϕ, the $d = \lambda/2.5$ array spacing was selected as optimal configuration, as it provides a good balance between the size of the array and estimation accuracy. This configuration, which is depicted in Figure 3.3(b), will be used throughout the rest of the chapter.

3.4.2 Method for array response reconstruction

It is useful to compare the performance of the MUSIC and Bartlett algorithms when using the CSV and ERP approaches. This provides insight on the impact of mutual coupling and gain loss on DoA estimation accuracy.

The ERP approach considers and automatically compensates for mutual coupling between array elements. On the other hand, CSV is an analytical approach that requires less information on the array since does not account for these factors. As shown in Figure 3.6, in a environment with just one LOS signal, the ERP estimation over

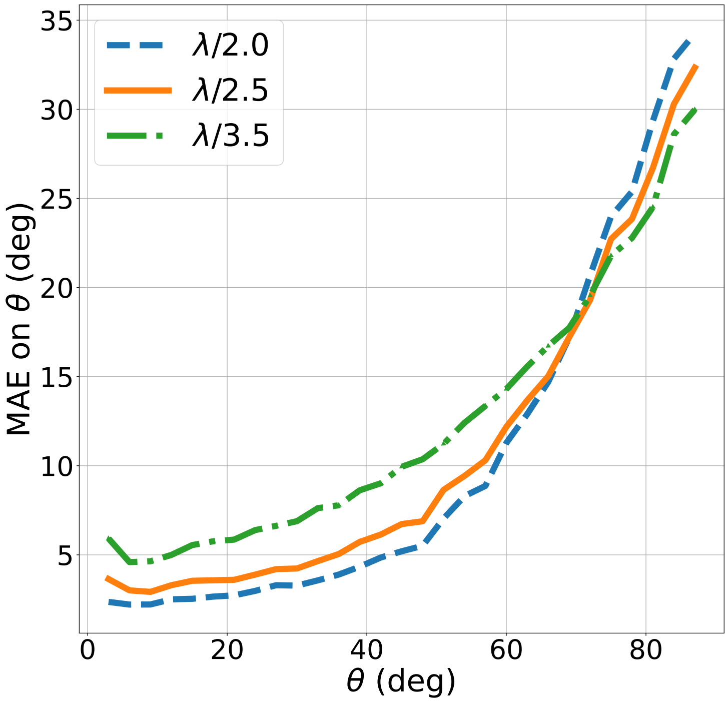

Figure 3.5: Impact of inter-element distance d with 2 NLOS and ERP approach. MAE using MUSIC algorithm, 1° resolution on θ. In this case, the MAE value increases for high values of θ since the gain becomes negligible at those angles. For $\theta < 70°$, $d = \lambda/2$ spacing demonstrates superior performance, while for $\theta > 70°$, $d = \lambda/2.5$ spacing is the recommended compromise.

ϕ and θ is more accurate than CSV. In the presence of multipath, the performance with ERP is still better than CSV as long as the number of NLOS paths does not degrade the SNR. However, in a noisy scenario, the two approaches do not differ much.

In Figure 3.7, an ERP comparison has been conducted considering 3×3 and 4×4 array configurations, for 0 and 2 NLOS paths. The evaluation of MAE on the azimuthal and elevation plane indicates that the 4×4 configuration outperforms the 3×3 configuration thanks to the higher spatial resolution of the larger array. In this simulation, the ERPs for the 4×4 array were simulated.

3.4.3 Number of snapshots

The problem of using few snapshots (or just one) for DoA algorithms has been extensively studied for linear arrays in the literature [47] and to a lesser extent for rectangular arrays [48], but in both cases, only isotropic radiators were considered. In [49], a linear array of independent isotropic radiators was studied with a single snapshot and multiple snapshots.

Here, the analysis is conducted by varying the number of snapshot, and using the ERP approach for every test.

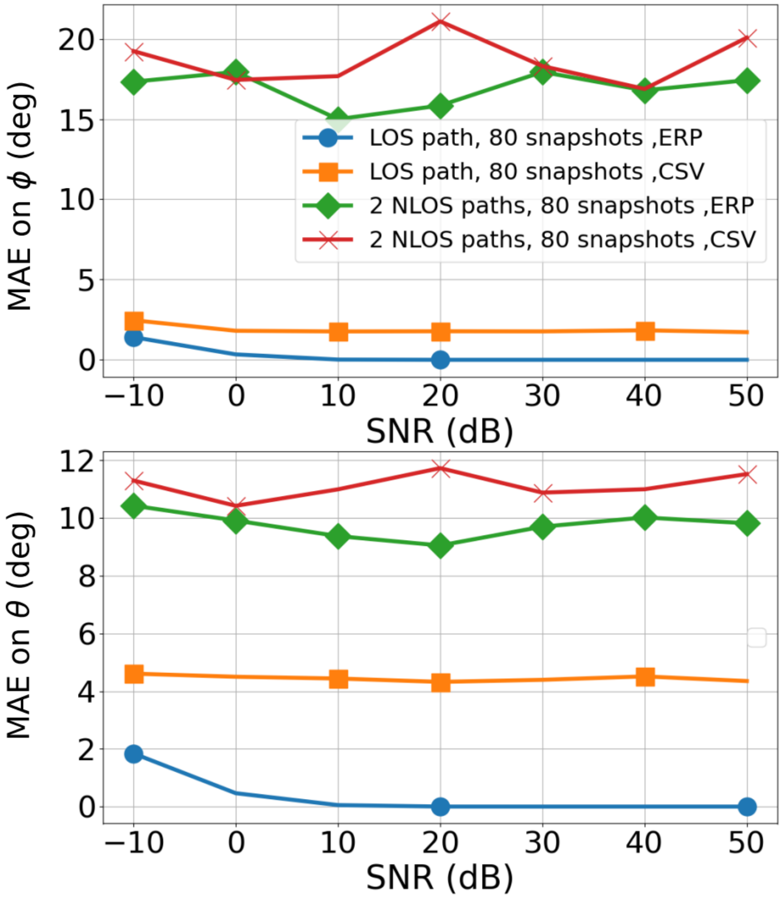

Figure 3.6: ERP vs CSV approach comparison with 0 and 2 NLOS. MAE evaluation using MUSIC algorithm, 1° resolution on azimuth and elevation, 80 snapshots and inter-elements distance of $d = \lambda/2.5$(as seen in Figure 3.3(b)). ERP can compensate for frequency mismatching and mutual coupling between elements ensuring better performances in terms of SNR over θ and ϕ. Nonetheless, when multiple reflections are considered (i.e., NLOS paths), similar performances between ERP and CSV approaches are achieved.

In Figure 3.8a, the performance of the algorithm is evaluated as the number of snapshots varies. It is observed that as the number of snapshots decreases, the MAE increases, indicating a decrease in performance. The degradation is noticeable when the number of snapshots is reduced from 80 to 8, especially for SNRs below 0 dB. The degradation is even more significant for a single snapshot, especially for SNRs less than 10 dB. Neither of the two presented algorithms outperforms the other in the case under test. This observation is consistent with the fact that MUSIC does not provide any advantage over conventional beamformers in the presence of coherent signals.

In the case of two reflections, as shown in Figure 3.8b, the MAE gets worse in the case of azimuthal acquisition: about 15° at SNR = 20 dB. Instead, about 9° degradation is observed in elevation. In particular, when SNR > 20 dB, similar performances are achieved as the number of snapshots varies. This implies that for high SNRs the accuracy resolution does not depend on the number of snapshots, with a significant reduction on the overall computational burden if only one snapshot is used. Again, MUSIC and Bartlett exhibit similar performances.

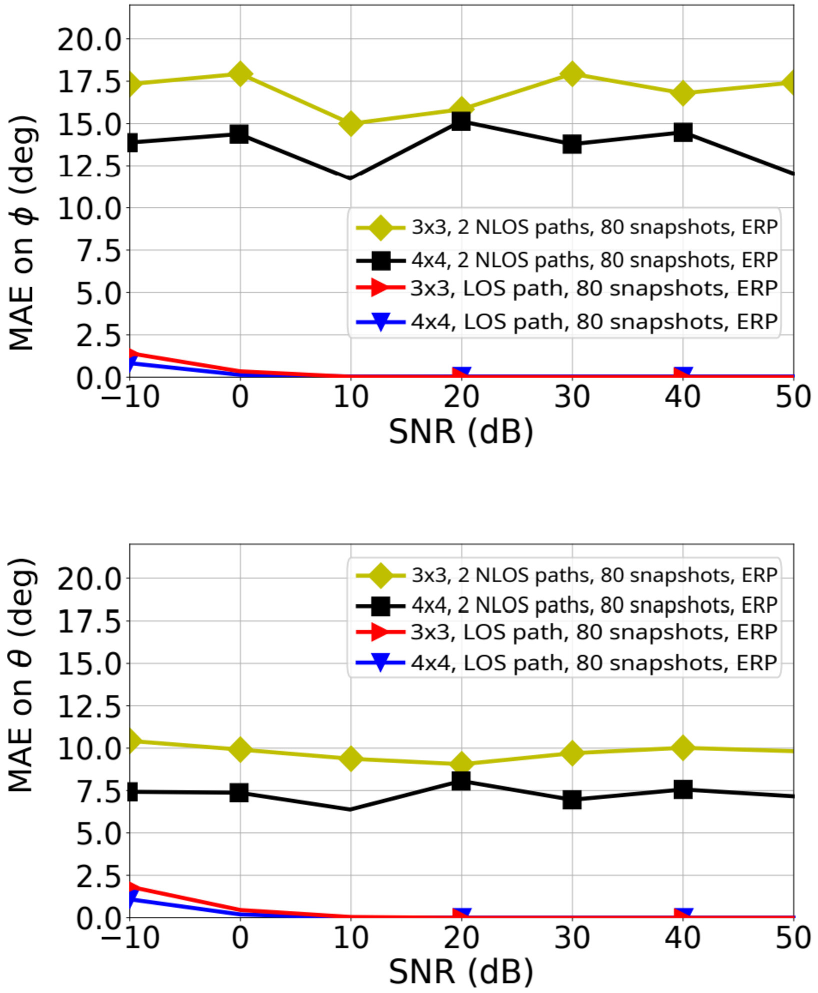

Figure 3.7: ERP approach comparison for 3×3 and 4×4 array configuration with 0 and 2 NLOS. MAE evaluation using MUSIC algorithm, 1° resolution on azimuth and elevation, 80 snapshots and inter-elements distance of $d = \lambda/2.5$. 4×4 array configuration outperforms 3×3 on azimuth and elevation.

For 4 NLOS paths, both the ERP and CSV approaches were found to fail, due to large number of coherent interferences, which degraded the SNR. However, we do not report the results for 4 NLOS, since the usage of circular polarisation effectively limits the number of coherent reflections. Moreover, the scenario with 4 strong NLOS signals is not very common in real applications, when both target and receiver use circular polarisation.

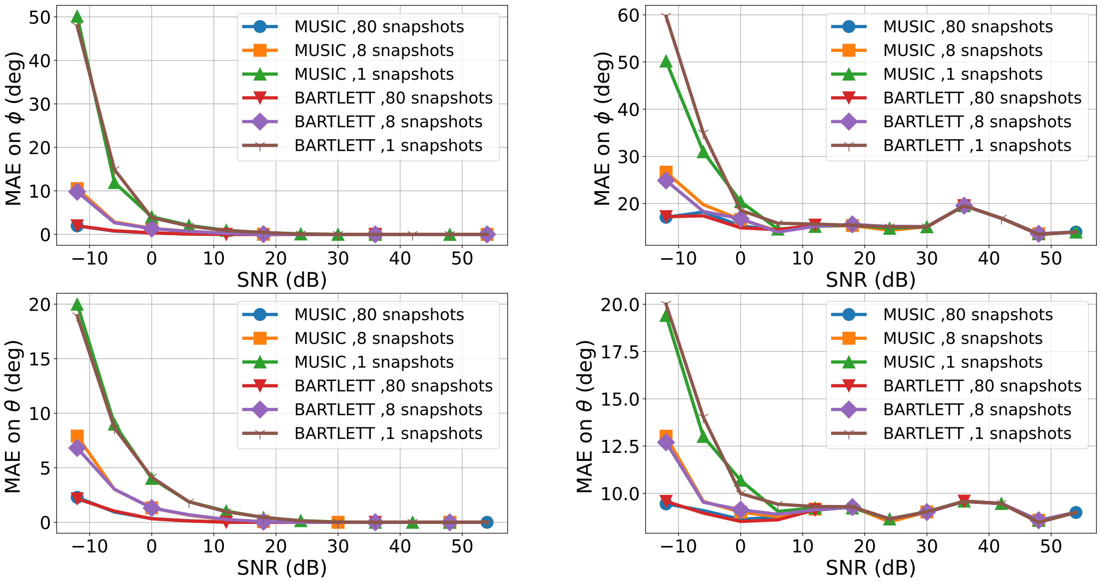

(a) 0 NLOS **(b)** 2 NLOS

Figure 3.8: (a) Comparison between MUSIC and Bartlett algorithms by varying the number of snapshots with 0 NLOS. MAE evaluation, 1° resolution on azimuth and elevation. When the number of snapshots decreases the performance in terms of MAE deteriorates. Specifically, a noticeable degradation is observed for SNR less than 0 dB when reducing the snapshots from 80 to 8. Considering only 1 snapshot results in a performance deterioration, especially for SNR values less than 10 dB.

(b) Comparison between MUSIC and Bartlett algorithms by varying the number of snapshots with 2 NLOS. MAE evaluation, 1° resolution on azimuth and elevation. As shown, for high SNR (i.e., > 20 dB), the accuracy does not depend on the number of snapshots, thus allowing faster computation.

3.5 Conclusions

In this chapter, the performance of a BLE DoA estimation application was evaluated by using a newly developed approach based on ERPs together with subspace-based DF algorithms, MUSIC and Bartlett. The performance was measured in terms of MAE by varying some setup parameters, namely the receiver size, the number of snapshots and the approach for array response reconstruction. While it was observed that reduction of the number of snapshots leads to a predictable loss of SNR in every condition, the ERP approach generally guarantees better results compared with the CSV approach, both in LOS and NLOS environments. The limit that still remains is the number of interferences, which degrades the SNR when increasing.

By accurately modelling the device with real values, higher performances can be reached, paving the way for next-generation direction-finding systems capable of operating effectively in miniaturized, multi-sensors platforms where conventional steering vector assumptions no longer hold.

Error metrics for Direction of Arrival estimation

4

4.1 Introduction 31
4.2 Error metrics 32
4.2.1 Proposed metric 33
4.3 Validation 34
4.4 Conclusions 37

This chapter investigates the topic related to the evaluation of the performance of the direction of arrival (DoA) estimation algorithms. Although this problem is widely studied, there is no unique error metric in the literature to compare the results obtained in the various works. Here, a new approach is considered, which deals with the angular nature of the results in DoA estimation. A set of numerical and experimental results is presented to demonstrate the potential of the proposed approach compared to the other well-known metrics. Unlike other metrics, the proposed error definition is frame-independent. Also, practical use cases are briefly discussed to highlight the pervasive impact of this fundamental definition.

4.1 Introduction

direction of arrival estimation is a long-standing area of research extensively studied in various disciplines and fruitfully applied in many fields of engineering, including in radar systems [50], sonar, navigation, and geophysical and seismic sensing, to name a few. Despite being a mature topic, it has become a research area of great interest at present due to the recent advancements in (i) signal processing [51] and machine learning techniques [52–54]; (ii) electronics and sensing devices [55, 56]; and (iii) wireless technologies [57, 58] and services [59, 60].

In the vast literature on DoA estimation, it is very common to evaluate the performance of these estimations with the Cramér-Rao bound (CRB) and/or with an error metric. Although they are both related to the performance of the estimators, they serve different purposes in the context of statistical estimation and signal processing. The key differences between them are summarized below:

- The CRB serves as a theoretical benchmark for the variance of unbiased estimators, whereas error metrics are practical tools used to assess the accuracy of any estimator, regardless of whether it is biased or unbiased;
- The CRB focuses on the minimum achievable variance, offering insight into the optimal performance of an estimator. In contrast, error metrics concentrate on the actual performance of the estimator, providing a measure of how well it performs with real data.

It is worth mentioning that the optimal achievable performance of different DoA estimators is well defined by means of the CRB in the literature. However, the actual performance of DoA estimators is evaluated using different error metrics, namely root mean square error (RMSE), mean square error (MSE), and mean absolute error (MAE).

To perform the evaluation, a comparison between the *true* and *estimated* directions is made. The problem in the usage of these metrics lies on the datum itself, since a direction is generally indicated by using the *azimuth* and *elevation* angles in a spherical reference system centred at the receiver. With the result of the estimation expressed through its angles, the resulting statistics – deriving from the simulations – should be regarded as a distribution in *directional statistics*. There are strategies to avoid this issue when dealing with a 1D DoA estimation problem – e.g. evaluating azimuth and elevation errors separately [61–64] – but it cannot be avoided in 2D DoA estimation.

4.2 Error metrics

1D DoA estimation

Let us start with the most-common used error metrics in the literature related to 1D DoA estimation; considering N number of tests, θ_n the direction of arrival for the nth test, and $\hat{\theta}_n$ its estimation, the mean absolute error (MAE), mean square error (MSE), and root mean square error (RMSE) are defined:

$$\mathrm{MAE} = \frac{1}{N}\sum_{n=1}^{N} \left|\hat{\theta}_n - \theta_n\right| \tag{4.1}$$

$$\mathrm{MSE} = \frac{1}{N}\sum_{n=1}^{N} \left(\hat{\theta}_n - \theta_n\right)^2 \tag{4.2}$$

$$\begin{aligned} \mathrm{RMSE_a} &= \frac{1}{N}\sum_{n=1}^{N} \sqrt{\left(\hat{\theta}_n - \theta_n\right)^2} \\ \mathrm{RMSE_b} &= \sqrt{\frac{1}{N}\sum_{n=1}^{N} \left(\hat{\theta}_n - \theta_n\right)^2} \end{aligned} \tag{4.3}$$

As it can be seen, the only problem in these metrics is that they not take into account the cyclic nature of the angular data, leading to possible distortions in the results – more evident when the angle is near 0°.

2D DoA estimation

For 2D DoA estimation, the most used metric is the RMSE, but it is applied in many different ways. The framework here is generally a spherical reference system, identifying a direction of arrival with the two angles, ϕ and θ. The first method is to evaluate separately the estimations of the two angles by applying on each of them the RMSE:

$$
\begin{aligned}
\mathrm{RMSE}_{\phi} &= \sqrt{\frac{1}{N}\sum_{n=1}^{N}\left(\hat{\phi}_n - \phi_n\right)^2} \\
\mathrm{RMSE}_{\theta} &= \sqrt{\frac{1}{N}\sum_{n=1}^{N}\left(\hat{\theta}_n - \theta_n\right)^2}
\end{aligned}
\tag{4.4}
$$

Such an approach may not offer a comprehensive view of the error since it does not provide a joint error. To address this issue, other authors have combined the azimuthal and the elevation error (as in [54]) for MAE and RMSE:

$$
\mathrm{MAE} = \frac{1}{N}\sum_{n=1}^{N}\left(\left|\hat{\theta}_n - \theta_n\right| + \left|\hat{\phi}_n - \phi_n\right|\right) \tag{4.5}
$$

$$
\mathrm{RMSE} = \sqrt{\frac{1}{N}\sum_{n=1}^{N}\left[\left(\hat{\theta}_n - \theta_n\right)^2 + \left(\hat{\phi}_n - \phi_n\right)^2\right]} \tag{4.6}
$$

Here, the two angular errors are combined by treating them as a two-dimensional array, while ignoring the physical 3D problem; both expressions may provide unexpected results when, for instance, incoming signals arrive from directions close to the z axis of a cartesian reference system (as in Figure 4.1).

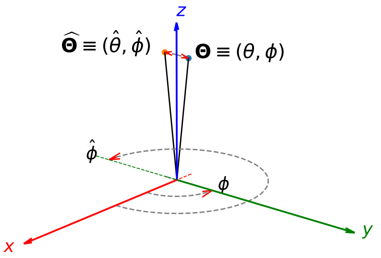

Figure 4.1: Limit situation for true and estimated angles, when the direction of arrival and its estimation are close to the z axis. In this case, classical error metrics like MAE or RMSE will fail to report the correctness of the prediction, giving rise to a high error, even though the directions are very close to each other.

For this reason, an error metrics that takes into account the distance between the true and estimated directions in 3D space needs to be addressed.

4.2.1 Proposed metric

Let $\mathbf{d}$ be the true direction of arrival and $\hat{\mathbf{d}}$ the estimated one, both defined in a spherical reference system and with radius equal to 1 (thus lying on the surface of a unit sphere). Converting them into 3D vectors on a cartesian reference system, they can be written:

$$
\begin{aligned}
\mathbf{d} = (1, \theta, \phi) &\leftrightarrow \mathbf{d} = (\sin\theta\cos\phi, \sin\theta\sin\phi, \cos\theta) \\
\hat{\mathbf{d}} = (1, \hat{\theta}, \hat{\phi}) &\leftrightarrow \hat{\mathbf{d}} = (\sin\hat{\theta}\cos\hat{\phi}, \sin\hat{\theta}\sin\hat{\phi}, \cos\hat{\theta})
\end{aligned}
\tag{4.7}
$$

Considering the definition of *direction cosines* and of scalar product between two vectors, and applying it to the both vectors expressed in cartesian coordinates [1]:

$$\mathbf{d} \cdot \hat{\mathbf{d}} = d_x \hat{d}_x + d_y \hat{d}_y + d_z \hat{d}_z = \cos \alpha_{\mathrm{E}} \tag{4.8}$$

and removing the cosine,

$$\alpha_{\mathrm{E}} = \arccos \left(\mathbf{d} \cdot \hat{\mathbf{d}} \right) \tag{4.9}$$

obtaining the angle (or angular distance) between them. Since the cosine is odd, there are two solutions for α_{E}: one is an acute angle and the other is an obtuse one. Picking the acute one – as a convention – gives the minimum angular distance.

Here, the MAE and the RMSE are rewritten with the new angular error:

$$\mathrm{MAE}_{\alpha} = \frac{1}{N} \sum_{n=1}^{N} \alpha_{\mathrm{E}} \tag{4.10}$$

$$\mathrm{RMSE} = \sqrt{\frac{1}{N} \sum_{n=1}^{N} (\alpha_{\mathrm{E}})^2} \tag{4.11}$$

4.3 Experimental validation

In this section, the performance of the proposed error metrics in different electromagnetic scenarios is analysed, using a receiver specifically designed for Bluetooth Low Energy (BLE) applications [42]. The details of the fabricated 3 × 3 array and its application for DoA estimation are reported in [42] for a single channel and in [65] for multiple channels of the BLE band. The DoAs are estimated with the classical Multiple Signal Classification (MUSIC) method using the conventional steering vector (CSV) and embedded radiation pattern (ERP), as discussed in Chapter 3. In Table 4.1, there are the test cases considered during this evaluation.

Table 4.1: Test cases (TC) for error comparison in 2D DoA estimation.

	TC1	TC2
(θ, ϕ)	(5,90)	(45,90)
$(\hat{\theta}, \hat{\phi})$	(5,270)	(45,270)
MAE	180	180
RMSE	180	180
α_{E}	10	90

Dependence of incoming DoA

In the first scenario, the sensitivity to the direction of the incoming signals – as indicated in the test cases (TCs) listed in Table 4.1 – is analysed within a real setup under various noise levels, as shown in Figure 4.2.

Specifically, the estimation error for TC 1 when using the CSV approach is shown in Figure 4.2a and the one using the ERP is shown in Figure 4.2c, while the error for TC 2 is presented in Figure Figure

[1] Geometrically speaking, performing the scalar product between two vectors means to select a plane containing both vectors and project one of them onto the other one.

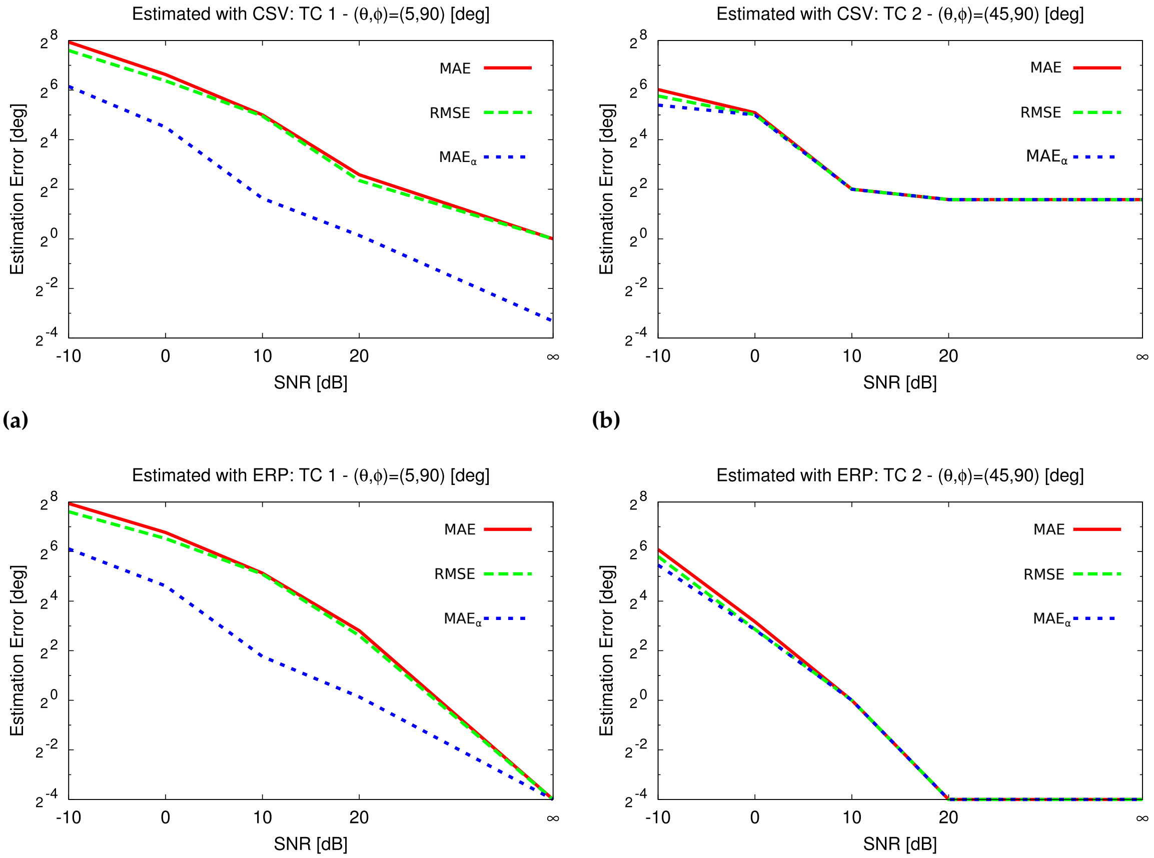

(a) **(b)** **(c)** **(d)**

Figure 4.2: Error vs. SNR, estimated using different metrics: CSV method for (**a**) TC 1 and (**b**) TC 2; ERP method for (**c**) TC 1 and (**d**) TC 2.

4.2b when using the CSV approach and Figure 4.2d when using the ERP. As expected and confirmed by the application in Chapter 3, the ERP outperforms the CSV in DoA estimation in terms of both metrics; however, the proposed metric MAE_α consistently produces lower estimated errors compared to commonly used metrics across the different cases and in noisy scenarios. The errors evaluated using the 2D metrics are, in general, overestimated for the $\theta \approx 0$ case compared to the one found with the proposed 3D metric, reinforcing the results in Table Table 4.1. Also, the estimated errors for TC 2 are less sensitive to the choice of error metric, which aligns with the findings in Table Table 4.1 for TC 2. This suggests that 2D error metric definitions may exaggerate the error in DoAs from the broadside ($\theta \approx 0$) direction.

Reference frame dependence

To verify the universality of the metric across reference systems, an analysis was performed using the same physical DoA but adopting different conventions for the reference system, specifically by using the antenna's plane, labelled as the YZ plane, as illustrated in Figure 4.3b, instead of the previously considered XY plane, as shown

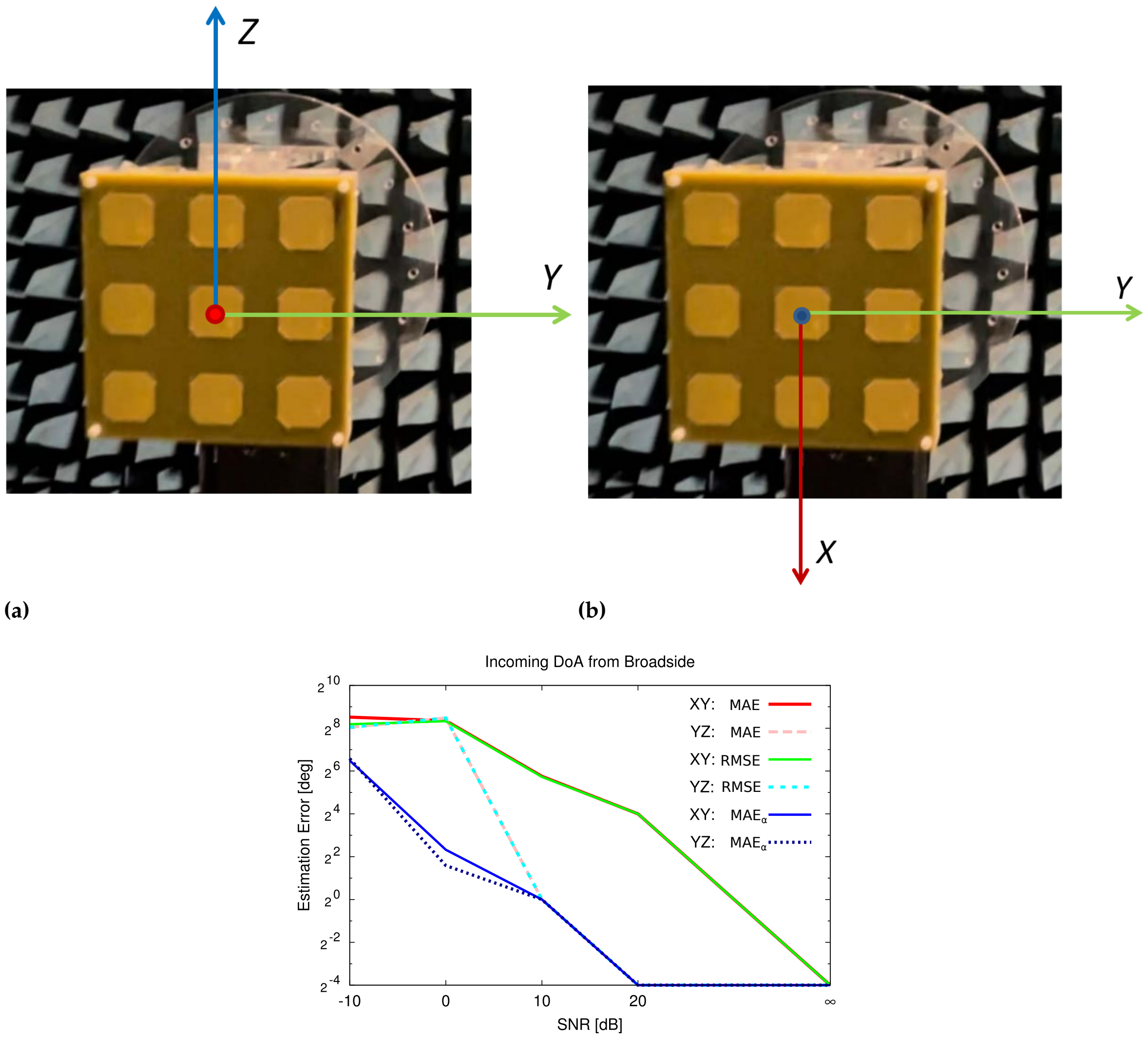

(a) **(b)**

(c)

Figure 4.3: Frame dependence – (**a**) receiver in XY plane, (**b**) receiver in YZ plane, and (**c**) errors evaluated using different metrics.

in Figure Figure 4.3a. Thus, the same incoming signal from the broadside direction will have the direction of arrival $(\theta, \phi) = (0, 0)$ as the first choice (Figure 4.3a) when the antenna array lies in the XY plane, and $(\theta, \phi) = (90, 0)$ as the second choice, Figure 4.3b, when the antenna lies in the YZ plane. The estimated errors obtained from the different metrics at varying noise levels are presented in Figure 4.4. Notably, the proposed metric, MAE$_\alpha$, demonstrates a consistent error across reference systems, while other metrics show sensitivity to the different reference systems, as highlighted in Figure 4.4.

Dependence on number of trials

The proposed metric, MAE$_\alpha$ (Equation 4.10), is not exactly equal to RMSE$_\alpha$ in Equation 4.11, which is an extended version of the equation reported in [66], at $N = 1$, although MAE$_\alpha$ = RMSE$_\alpha$ when

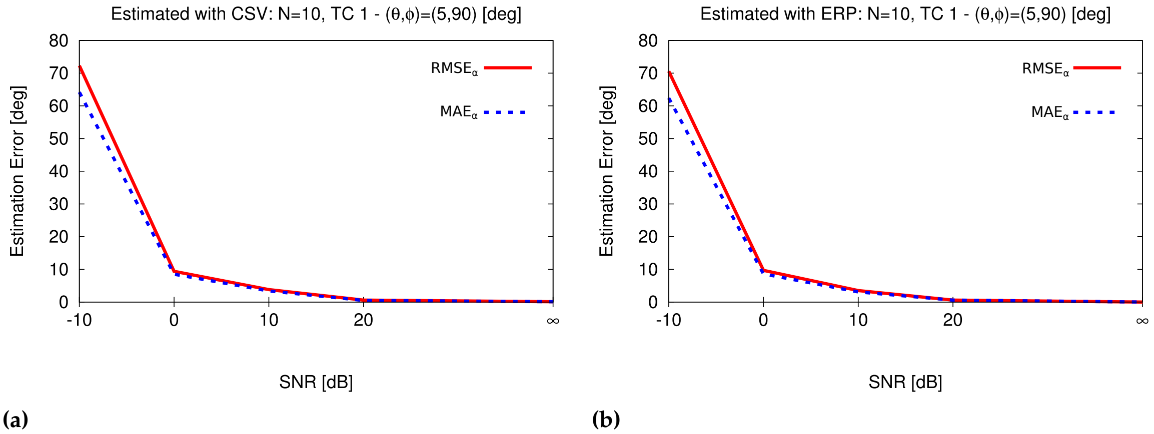

(a) **(b)**

Figure 4.4: Sensitivity to number of trials – (**a**) CSV and (**b**) ERP.

$N = 1$. Figure Figure 4.3 shows the dependence of error estimation on the number of trials, N, with the proposed metric Equation 4.10 and with the metric reported in [66]. It is clearly evident that the error metric discussed in [66] and the newly proposed one are very similar but not exactly equal.

4.4 Conclusions

The error metrics used in the literature on DoA estimation have been reviewed and a *proper and unique* error metric for 2D DoA estimation has been recommended. In recent papers, a proper definition of the error metric used is often omitted, and, in some cases, inappropriate ones that lack a meaningful physical interpretation are adopted. It has been observed that commonly used error metrics can sometimes yield incorrect and misleading results due to the physical 3D nature of the 2D DoA estimation problem. Therefore, an error-free universal error metric was proposed, which was defined by exploiting the directional cosines. In addition, it has been verified, using numerous representative examples, that the proposed new error metric is able to provide meaningful results as it is related to the angular difference between the actual direction of arrival and its estimation. Moreover, the sensitivity of different error metrics were validated using the experimental data from a fabricated 3×3 locator designed for BLE applications. The experimental validation confirmed that the proposed metric is insensitive to the direction of incoming signals, the reference system used, and the number of trials conducted compared to other well-known error metrics.

Drop Size Distribution retrieval through Deep Learning approach

5

In this chapter, a novel method to estimate the drop size distribution (DSD) of a cloud of particles – focusing on hydrometeors – is presented. This method exploits the polarimetric capacity of modern weather radars by using the ensemble-averaged covariance matrices to perform the estimation of the parameters for a distribution modelled after the gamma DSD through a Deep Learning (DL) approach using modern techniques, such as multi-task learning (MTL). Before the application itself, a little summary of the necessary theory used in the methodology is presented.

5.1 Introduction 39
5.2 Theory 41
5.2.1 Radar scattering 41
5.2.2 DSD 44
5.3 Methodology 45
5.3.1 Dataset generation . . 45
5.3.2 NN design 48
5.4 Results 51
5.4.1 Frequency tests 57
5.5 Conclusions 64

5.1 Introduction

The drop size distribution (DSD) is one of the most fundamental descriptors of the microphysics behind the precipitation of hydrometeors. Its aim is to characterise the sensed medium (e.g., air-water mixture during rain) through the computation of the number of raindrops in a unit volume [1] by assuming the particles statistically distributed with respect to the diameter (Figure 5.1). This results in a macrophysical model that directly links the microphysical processes in the medium to macroscopic quantities such as rain rate, reflectivity, and attenuation. Accurate retrieval of DSDs from ground-based and satellite instruments is at the core of modern quantitative precipitation estimation (QPE) and remote sensing of rainfall.

Over the past several decades, advances in radar meteorology have made it possible to infer DSD parameters from active and passive microwave sensors. Polarimetric and dual-frequency radars, in particular, allow for the retrieval of the median volume diameter, normalised intercept parameter, and shape factor of the DSD through empirical or physically constrained relationships [67, 68]. However, these retrievals are highly sensitive to assumptions about the underlying DSD model; the most commonly used ones are the exponential, gamma, or generalized gamma distributions [69, 70]. Also, the uncertainty in DSD retrievals arises from both instrumental limitations and natural variability; for example, the choice of radar frequency affects sensitivity to different drop sizes and scattering regimes [71].

A common approach to estimate the DSD has been the integration of in-situ measurements from disdrometers with polarimetric radar observations. This represents one of the most robust and comprehensive approaches for retrieving DSDs. Each observational system offers

[1] Generally, a cube of 1 m^3 is considered as a unit volume.

complementary strengths: disdrometers provide high-resolution, ground-based DSDs, while polarimetric radars offer wide-area coverage and vertical profiling capability. Together, these data sources enable both calibration and validation of DSD retrieval algorithms and allow improved quantification of uncertainties across spatial and temporal scales [70, 72]. One of the central advancements in this area has been the development of physically constrained DSD models that use radar observables such as reflectivity (Z), differential reflectivity (Z_{DR}), and specific differential phase (K_{DP}) to estimate the parameters of gamma or generalized gamma DSDs. When these radar-derived estimates are validated against in-situ disdrometer data, strong agreement is often observed, particularly when constrained-gamma models are employed [73, 74]. Such multi-sensor comparisons have been instrumental in refining shape-slope relationships in constrained models, reducing biases in retrieved median volume diameter (D_0) and intercept parameter (N_{w}).

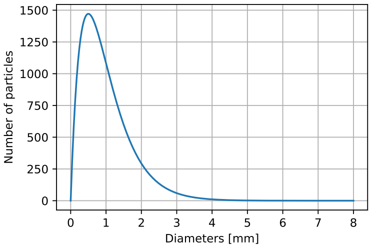

Figure 5.1: Generic example of DSD, where the number of particles are distributed against their diameters. It is worth noticing that the distribution is generally skewed towards the smaller particles.

Recent studies have also demonstrated the benefits of collocated radar and disdrometer networks for retrieving higher-order DSD moments. For instance, a study showed that lower-order DSD moments (M_0 - M_2), which are typically difficult to retrieve from radar alone, can be accurately estimated by combining polarimetric variables with complete in-situ spectra extending down to small drop sizes. The integrated retrievals achieved less than 15 % bias in moment estimates compared with direct disdrometer calculations, illustrating the synergy between remote and ground-based sensing [75]. Similarly, dual-polarization radar networks integrated with disdrometer arrays have provided valuable insight into the variability of DSDs during stratiform and convective events. Ground-based disdrometers capture localized microphysical features such as breakup and coalescence processes, while polarimetric radars enable the spatial extrapolation of these characteristics to mesoscale domains. Validation campaigns, such as those conducted in Oklahoma and West Africa, confirm that co-located datasets significantly improve the accuracy of radar-based DSD retrievals and rainfall estimation [72, 76].

Despite the significant advancements in radar-based retrieval algorithms, accurate and reliable DSD estimation remains fundamentally dependent on disdrometer data. Polarimetric radar systems, while offering extensive spatial and temporal coverage, inherently provide indirect measurements of DSD parameters that require model assumptions – such as gamma or exponential forms – introducing potential biases and uncertainties. Disdrometers, by contrast, directly measure the size and fall velocity of individual raindrops, serving as the essential ground truth for calibrating, validating, and refining radar-based retrievals.

5.2 Theory

In this section, an overview of the basic theory of radar scattering and drop size distribution will be given, which will be useful to understand the results in this study.

5.2.1 Radar scattering

Let us consider the scattering of an incident plane wave by a single particle in the Rayleigh regime [2]. Suppose a cartesian reference system with the origin at the centre of the particle, and the incident wave coming from a direction specified by the unit vector $\hat{\mathbf{k}}_i$ or by the polar angle θ_i and the azimuthal angle ϕ_i, forming the triplet of unit vectors $(\hat{\mathbf{k}}_i, \hat{\theta}_i, \hat{\phi}_i)$. If the horizontal unit vector $\hat{\mathbf{h}}_i = \hat{\phi}_i$ and the vertical unit vector $\hat{\mathbf{v}}_i = \hat{\theta}_i$ are considered, the triplet $(\hat{\mathbf{k}}_i, \hat{\mathbf{v}}_i, \hat{\mathbf{h}}_i)$ can be obtained. The incident wave can be written as:

$$\mathbf{E}^i = \hat{\mathbf{e}}_i E_0 \, e^{-jk_0 \, \hat{\mathbf{i}} \cdot \mathbf{r}_i} \tag{5.1}$$

where $\mathbf{r}_i$ is the vector from the origin to a point of the plane of constant phase (wavefront), $\hat{\mathbf{i}}$ is the direction of incidence, $k_0 = 2\pi/\lambda$ is the wave number of free space, with λ the associated wavelength. At the origin of the reference system – i.e. the centre of the particle – the electric field becomes the plane wave amplitude and, considering the vertical and horizontal unit vectors, can be written:

$$\mathbf{E}^i(\mathrm{O}) = \hat{\mathbf{e}}_i E_0 = E_h^i \hat{\mathbf{h}}_i + E_v^i \hat{\mathbf{v}}_i \tag{5.2}$$

where O identified the origin. If the back scatter alignment (BSA) is used, the reflected wave at the origin will have the form $\mathbf{E}^r = E_h^r \hat{\mathbf{h}}_r + E_v^r \hat{\mathbf{v}}_r$ and, following the result in [77], the relationship between the incident and reflected waves is:

$$\mathbf{E}^r = \underline{\mathbf{S}}_{\mathrm{BSA}} \, \mathbf{E}^i = \begin{bmatrix} E_h^r \\ E_v^r \end{bmatrix} = \frac{e^{-jk_0 r}}{r} \begin{bmatrix} S_{hh} & S_{hv} \\ S_{vh} & S_{vv} \end{bmatrix}_{\mathrm{BSA}} \begin{bmatrix} E_h^i \\ E_v^i \end{bmatrix} \tag{5.3}$$

where r is the magnitude of the position vector and $\underline{\mathbf{S}}_{\mathrm{BSA}}$ is the scattering matrix in BSA convention. For the reciprocity theorem [78], in BSA convention $S_{hv} = S_{vh}$, making the scattering matrix Hermitian.

Considering that the raindrops are generally considered to be oblate spheroids instead of perfect spheres, the elements of the scattering matrix in BSA can be written:

[2] The scattering problem at hand is in the Rayleigh regime when the dimensions of the particles are very small compared to the wavelength of the incident plane wave.

$$
\begin{aligned}
(S_{hh})_{\mathrm{BSA}} &= \frac{k_0^2}{4\pi\varepsilon_0}\left[\alpha + (\alpha_z - \alpha)\sin^2\theta_{\mathrm{O}}\sin^2\phi_{\mathrm{O}}\right] \\
(S_{hv})_{\mathrm{BSA}} &= \frac{k_0^2}{4\pi\varepsilon_0}\,[\,\frac{(\alpha_z - \alpha)}{2}\,(\,\cos\theta_i\sin^2\theta_{\mathrm{O}}\sin 2\phi_{\mathrm{O}} \\
&\quad + \sin\theta_i\sin 2\theta_{\mathrm{O}}\sin\phi_{\mathrm{O}}\,)\,] \\
(S_{vv})_{\mathrm{BSA}} &= \frac{k_0^2}{4\pi\varepsilon_0}\,[\,\alpha + (\alpha_z - \alpha)\,(\,\cos^2\theta_i\sin^2\theta_{\mathrm{O}}\cos^2\phi_{\mathrm{O}} \\
&\quad + \sin^2\theta_i\cos^2\theta_{\mathrm{O}} + \frac{\sin 2\theta_i\sin 2\theta_{\mathrm{O}}\cos\phi_{\mathrm{O}}}{2}\,)\,]
\end{aligned}
\tag{5.4}
$$

where θ_{O} and ϕ_{O} are the orientation angles of the particle, which express the rotation of its symmetry axis along the x axis and along the z axis, respectively. α_z is the polarisability along the symmetry axis of the particle – supposed to be along z – and α is the one along the other two axes; they both derive from the way the polarisability matrix is expressed:

$$\underline{\boldsymbol{\alpha}} = \alpha\underline{\mathbf{I}} + (\alpha_z - \alpha)\hat{\mathbf{z}}\hat{\mathbf{z}}$$

Since the scattering matrix is symmetric, a feature vector can be introduced:

$$\mathbf{s} = \begin{bmatrix} S_{hh} \\ S_{hv} \\ S_{vv} \end{bmatrix}_{\mathrm{BSA}} \tag{5.5}$$

containing the elements of the upper triangular part of the scattering matrix.

The scattering matrix above is related to the scattered signal from a single particle. When observing a weather phenomenon, the scattering of a single particle cannot be measured; also, it is not possible to determine the number of particles in the illuminated volume or other properties (e.g. orientation, shape). Thus, the cloud of particles is modelled as a statistical distribution per unit volume, either for the number of particles or the other properties. The modelling of the number of particles is generally achieved by using a drop size distribution (DSD), which returns the concentration of particles per diameter in a unit volume (see Subsection 5.2.2).

To study the polarimetric characteristics of the cloud of particles (raindrops), the ensemble-averaged covariance matrix can be built from the feature vector above:

$$\Sigma_{\mathrm{BSA}} = \langle n\mathbf{s}\mathbf{s}^* \rangle = \begin{bmatrix} \sigma_{11} & \sigma_{12} & \sigma_{13} \\ \sigma_{21} & \sigma_{22} & \sigma_{23} \\ \sigma_{31} & \sigma_{32} & \sigma_{33} \end{bmatrix}$$

$$= \left\langle n \begin{bmatrix} |S_{hh}|^2 & \sqrt{2}(S_{hh}S^*_{hv}) & (S_{hh}S^*_{vv}) \\ \sqrt{2}(S_{hv}S^*_{hh}) & 2|S_{hv}|^2 & \sqrt{2}(S_{hv}S^*_{vv}) \\ (S_{vv}S^*_{hh}) & \sqrt{2}(S_{vv}S^*_{hv}) & |S_{vv}|^2 \end{bmatrix} \right\rangle \tag{5.6}$$

$$= \begin{bmatrix} \langle n\ |S_{hh}|^2 \rangle & \langle n\ \sqrt{2}(S_{hh}S^*_{hv}) \rangle & \langle n\ (S_{hh}S^*_{vv}) \rangle \\ \langle n\ \sqrt{2}(S_{hv}S^*_{hh}) \rangle & \langle n\ 2|S_{hv}|^2 \rangle & \langle n\ \sqrt{2}(S_{hv}S^*_{vv}) \rangle \\ \langle n\ (S_{vv}S^*_{hh}) \rangle & \langle n\ \sqrt{2}(S_{vv}S^*_{hv}) \rangle & \langle n\ |S_{vv}|^2 \rangle \end{bmatrix}$$

The generic element σ of the matrix depends on the M particle states $g_1, g_2, \dots, g_M$ (e.g. shape, orientation, thermodynamic phase, etc.) and the DSD $N(D)$. Visually dropping this dependence for the generic scattering element $S_{ab}(D; g_1, g_2, \dots, g_M) = S_{ab}$ and for the joint probability density function $\mathbb{P}(g_1, g_2, \dots, g_M) = \mathbb{P}(\mathbf{g})$ (with $\mathbf{g} = (g_1, g_2, \dots, g_M)$), the generic element will have this form:

$$\sigma = \int_D N(D) \int_{g_1} \cdots \int_{g_M} S_{ab} S_{cd}\, \mathbb{P}(\mathbf{g})\, dg_1\, dg_2 \dots dg_M\, dD \tag{5.7}$$

where $a, b, c, d \in \{h, v\}$.

In this case, only the orientation of the particles is considered as a particle state; this can be statistically modelled through a particle orientation distribution (POD), which gives a statistical orientation for the raindrops by using their orientation angles θ_{O} (which will become θ_{POD}) and ϕ_{O} (which will become ϕ_{POD}); thus, the scattering element can be rewritten as:

$$\sigma = \int\limits_D N(D) \int\limits_{\theta_{\mathrm{POD}}} \int\limits_{\phi_{\mathrm{POD}}} S_{ab}\, S_{cd}\, \mathbb{P}_{\mathrm{POD}}\, d\theta_{\mathrm{POD}}\, d\phi_{\mathrm{POD}}\, dD \tag{5.8}$$

where $\mathbb{P}_{\mathrm{POD}} = \mathbb{P}(\theta_{\mathrm{POD}}, \phi_{\mathrm{POD}})$ represents the probability density of the POD.

The scattering elements in Equation 5.4, the ensemble-averaged covariance matrix in Equation 5.6 with its elements expressed as in Equation 5.8 are the basis for the simulator built to generate the necessary input, as described in Subsection 5.3.1.

5.2.2 Drop Size Distribution

The drop size distribution (DSD) statistically models the distribution of the particles inside a cloud by their diameter – or, better, the diameter of the equivolume sphere, as explained below.

The importance of DSD estimation lies in the possibility of computing many rainfall-related variables; these are generally derived using the moments (also statistical) of the DSD function. The definition of the DSD function is the following.

Physically, the **drop size distribution** $N(D)$ [$\mathrm{mm}^{-1}\,\mathrm{m}^{-3}$] is the concentration of drops (particles) of diameter D [mm] per unit volume of air. We write:

$$N(D) = N_T f(D) \tag{5.9}$$

where

$$N_T = \int_0^\infty N(D)dD \tag{5.10}$$

is the total number concentration of raindrops [m^{-3}] and $f(D)$ [mm^{-1}] is a probability density function for the drop diameters such that:

$$\int_0^\infty f(D)dD = 1 \quad , \qquad \mathbb{P}[D \leq x] = \int_0^x f(D)dD$$

The diameter D in the definition is not the real diameter of a water drop, but the diameter of the equivalent (or equivolume) sphere, since a drop may not have a spherical shape. In general, due to aerodynamic forces, the drops are oblate spheroids; this effect is more evident in the bigger particles, and less for smaller particles (they are almost spheres) [79].

Considering that the rain phenomena are generally extended very widely in space, the local concentrations of raindrops, their positions, and sizes all fluctuate over space and time. Therefore, the DSD should be seen as a probabilistic summary of the average (i.e., the expected) raindrop size distribution over a large number of unit volumes. For weather-radar-related applications, this assumption is reasonable because radar sampling volumes are generally much larger than one cubic meter (unit volume).

A concept widely used for a DSD is related to its statistical moments, which are related to some physical properties of the cloud of particles. The nth (or nth-order) **moment** M_n [$\mathrm{mm}^n\,\mathrm{m}^{-3}$] of the DSD is defined as:

$$M_n = \int_0^\infty D^n N(D) dD \tag{5.11}$$

where D is the equivalent diameter. As said before, these moments are related to some rainfall properties of interest:

- 0th moment is the **total number concentration** $N_T[\mathrm{m}^{-3}]$;
- 1st moment is related to the **mean drop diameter**;
- 2nd moment is the most relevant to assess **optical extinction** (in visibility studies) [80];
- 3rd moment is linked to the **liquid water content** (LWC);
- 3.67th moment is approximately proportional to the **rainfall rate** [81];
- 5th moment is roughly proportional to the **kinetic energy** [82];
- 6th moment is equal to the microwave backscattering (**radar reflectivity**) in the Rayleigh scattering regime [83].

Most radar remote-sensing applications rely heavily on higher-order moments of the DSD, while microphysical processes in rain, such as collisional drop breakup, coalescence, and evaporation, also depend on lower-order moments [84, 85]. Higher-order moments are more sensitive to the concentration of large drops than lower-order moments. This is why a few large drops will affect rain rate and radar reflectivity substantially, while having very little impact on the mean drop diameter and drop number concentration.

5.3 Methodology

The approach used here aims at retrieving the DSD parameters by predicting them with a fully connected neural network (FCNN), taking the ensemble-averaged covariance matrices as input. To achieve this goal, the solution of the direct problem was studied for the generation of a dataset; it was also needed the design and training of a neural network. In the following, the details of these operations are given, together with the tools used to assess the prediction quality.

5.3.1 Dataset generation

When using a machine learning (ML) approach, the first step is usually to create a dataset to train the network – thus containing the "real" *training* samples and the ones used for the *validation* and *test* phases.

Here, a simulator capable of solving the direct problem – i.e. capable of computing the ensemble-averaged scattering matrix and the ensemble-averaged covariance matrix – was developed, implementing also the theory from Section 5.2. There are many parameters that can be set, both related to the physics of the cloud of particles and the simulation itself; the most important ones, along with the values used in this case, are listed in Table 5.1.

Table 5.1: Parameters fed to the simulator to generate the ensemble-averaged covariance matrices to be used as input to the FCNN.

Dataset generation parameters

Parameter	**Value**
Incoming echo elevation angle θ_{el}	0°
Radar frequency	2 GHz
Relative permittivity ε_{w}	$77.9 + j\,7.57$
drop size distribution	Gamma DSD
Diameter range	0 mm to 8 mm
Diameter resolution	0.1 mm
Parameters resolutions	
$\Delta\mu$	0.01
$\Delta\lambda$	$0.01\,\mathrm{mm}^{-1}$
DSD parameters	
μ	0 to 15
λ	$0\,\mathrm{mm}^{-1}$ to $30\,\mathrm{mm}^{-1}$
N_0	$8000\,\mathrm{m}^{-3}\,\mathrm{mm}^{-1-\mu}$
particle orientation distribution	Fisher Distribution
Parameters resolutions	
$\Delta\theta_{\mathrm{POD}}$	1°
$\Delta\phi_{\mathrm{POD}}$	1°
Orientation angles ranges	
θ_{POD}	0° to 180°
ϕ_{POD}	0° to 360°
POD parameters	
κ	100
$\bar{\theta}_{\mathrm{POD}}$	0°
$\bar{\phi}_{\mathrm{POD}}$	0°

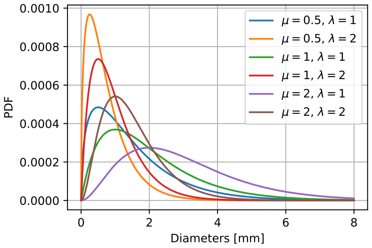

Figure 5.2: Effect of μ and λ parameters on the form of the gamma DSD. Increasing μ moves the "bell" shape to the right, while increasing λ dumps the right slope of the bell, narrowing it.

Since the aim is to train a neural network to retrieve the DSD parameters, the generated dataset contains the ensemble-averaged covariance matrices obtained by changing those parameters in their chosen ranges and considering all the possible combinations. The chosen DSD is the classical gamma DSD, as defined in [81]:

$$N(D) = N_0 D^{\mu} e^{-\lambda D} \qquad [\mathrm{m}^{-3}] \tag{5.12}$$

where $N_0[\mathrm{m}^{-3}\mathrm{mm}^{-1-\mu}]$ is the intercept to scale the total concentration of particles, μ is the shape parameter, and $\lambda[\mathrm{mm}^{-1}]$ is the slope parameter. The effect of μ and λ in the distributions can be observed in Figure 5.2.

The investigated variation in parameters is related to the change of μ and λ, with μ varying from 0 to 15 and λ varying from $0\,\mathrm{mm}^{-1}$ to $30\,\mathrm{mm}^{-1}$. These ranges of values for both parameters were chosen by looking at empirical DSD ranges in literature [86]. The only difference in range is for μ which starts from 0 and not from -2; the reason for this choice is that the DSD is just a very high peak at $D = 0$ for $\mu \leq 0$ – decreasing μ moves the "bell" to the left, narrowing it – which destabilises the numerical integrations to compute the covariance matrix, leading to a matrix with no valid values.

To compute the scattering from a cloud of raindrops, the orientation of the particles is also important. The distribution that was used is the *Fisher distribution*, which is a special case of the *von Mises-Fisher distribution* in directional statistics, as suggested in [78].

The *von Mises-Fisher distribution* is a probability distribution on the $(p-1)$-sphere in $\mathbb{R}^p$. Its probability density function for the random p-dimensional unit vector $\hat{\mathbf{x}}$ is given by:

$$f_p(\hat{x}, \hat{\mu}, \kappa) = C_p(\kappa) e^{\kappa\, \hat{\boldsymbol{\mu}}^T \hat{\mathbf{x}}}$$

where $\kappa \geq 0$ is the concentration parameter, $\hat{\boldsymbol{\mu}}$ ($\|\hat{\boldsymbol{\mu}}\| = 1$) is the mean direction, and $C_p(\kappa)$ is the normalisation constant. If $p = 3$, the distribution becomes the Fisher distribution

$$f_3(\hat{\mathbf{x}}, \hat{\boldsymbol{\mu}}, \kappa) = C_3(\kappa) e^{\kappa\, \hat{\mu}^T \hat{\mathbf{x}}} = \frac{\kappa}{4\pi\ \sinh\kappa} e^{\kappa\, \hat{\mu}^T \hat{\mathbf{x}}}$$

If we consider that

$$\begin{aligned}
\hat{\mu} &= \sin\bar{\theta}_{\mathrm{POD}} \cos\bar{\phi}_{\mathrm{POD}} + \sin\bar{\theta}_{\mathrm{POD}} \sin\bar{\phi}_{\mathrm{POD}} + \cos\bar{\theta}_{\mathrm{POD}} \\
\hat{x} &= \sin\theta_{\mathrm{POD}} \cos\phi_{\mathrm{POD}} + \sin\theta_{\mathrm{POD}} \sin\phi_{\mathrm{POD}} + \cos\theta_{\mathrm{POD}}
\end{aligned}$$

where $\bar{\theta}_{\mathrm{POD}}$ and $\bar{\phi}_{\mathrm{POD}}$ are the angles with respect to the reference system values for the mean direction, we can rewrite:

$$\begin{aligned}
&F(\theta_{\mathrm{POD}}, \phi_{\mathrm{POD}}) = \\
&\frac{\kappa \sin\theta_{\mathrm{POD}}}{4\pi \sinh(\kappa)}\, e^{\,\kappa\left[\cos\bar{\theta}_{\mathrm{POD}} \cos\theta_{\mathrm{POD}} + \sin\bar{\theta}_{\mathrm{POD}} \sin\theta_{\mathrm{POD}} \cos(\phi_{\mathrm{POD}} - \bar{\phi}_{\mathrm{POD}})\right]}
\end{aligned} \tag{5.13}$$

where $0 < \theta_{\mathrm{POD}} < \pi; 0 < \phi_{\mathrm{POD}} < 2\pi$ and $\kappa > 0$; and $\bar{\theta}_{\mathrm{POD}}$ and $\bar{\phi}_{\mathrm{POD}}$ are the average values of θ_{POD} and ϕ_{POD}, respectively, and κ is a parameter that controls the width (scale) of the distribution.

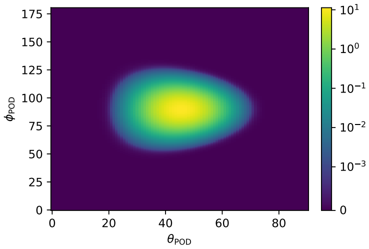

Figure 5.3: Visual heatmap for the Fisher distribution when using $\kappa = 100$, $\bar{\theta}_{\mathrm{POD}} = 0°$ and $\bar{\phi}_{\mathrm{POD}} = 0°$. θ_{POD} and ϕ_{POD} vary in the intervals [0°-180°] and [0°-360°], respectively.

In this case, θ_{POD} ranges from0° to 180°, ϕ_{POD} from0° to 360°, $\kappa = 100$, $\bar{\theta}_{\mathrm{POD}} = 0°$, and $\bar{\phi}_{\mathrm{POD}} = 0°$, as suggested in [78]. A visual representation of the Fisher distribution with these values is given in Figure 5.3.

Trying to emulate the real situation for a weather radar, and considering that the formulation above for the radar scattering was made in the Rayleigh regime, the frequency of the wave interacting with the cloud of raindrops was set to 2 GHz (S-band); at the same time, the relative permittivity of the water was set to $\varepsilon_{\mathrm{w}} = 77.9 + j\,7.57$, as considered in [87], for the chosen frequency and a temperature of 25 °C. Also, the elevation angle of the radar antenna was set to $\theta_{\mathrm{el}} = 0°$.

5.3.2 Neural network design

Here, a neural network-based model was developed, to address the problem of accurately retrieving the parameters of the DSD from radar polarimetric measurements. Various techniques of ML have been used in literature to this end, such as random forests, support vector regression, and Fully Connected Neural Networks (FCNNs); they represent a data-driven approach to model the complex dependencies and improve the retrieval accuracy [88] by using the polarimetric variables [89, 90].

The proposed approach focuses on the design of a FCNN in a Deep Learning (DL) framework to retrieve both the μ and λ of the traditional gamma DSD at the same time, without recurring to a neural network per parameter or normalised versions of the distribution. The configuration of the FCNN is shown in Table 5.2.

The input dataset contains the ensemble-averaged covariance matrices created with the methodology in Subsection 5.3.1. Before feeding them to the neural network, the matrices needed to be flattened to be passed to the input layer of the FCNN; also, there are some considerations that need to be done: (a) the elements of a covariance matrix are complex-valued numbers, (b) the matrix is symmetric, and (c) the off-diagonal elements of the matrix go to zero when a *"mirror" reflection symmetry* condition [3] happens. Since the POD used here (see Equation 5.13) satisfies (c) – and (b) is always true – the choice was to use only the upper-triangular part of the covariance matrix, and in particular using only the on-diagonal elements (the two off-diagonal are zero).

The general approach to handle complex-valued input data in neural networks is to find a real-valued representation suitable for the problem at hand [91]. Here, the choice was to split complex-valued numbers in magnitude and phase; considering part of the matrix selected before, this leaves us with 4 magnitudes and 1 phase. Only

[3] As demonstrated in [78], this happens when the POD is symmetric with respect to the mean canting angle

MTL FCNN configuration

Parameter	**Value**
Dataset	covariance matrices
Batch size	128
Dataset percentages	
Training phase	70 %
Validation phase	20 %
Test phase	10 %
Number of inputs	4
Number of outputs (tasks)	2
Common hidden layers	1
Number of units	128
Task 1	retrieve μ
Hidden layers	3
Number of units	64, 32, 16
Task 2	retrieve λ
Hidden layers	3
Number of units	64, 32, 16
Hidden layers regularisation	Yes
Weights reg. factor	1×10^{-3}
Biases reg. factor	1×10^{-3}
Hidden layers normalisation	Yes
Normalisation type	LayerNormalisation
Hidden layers activation	GELU
learning rate (LR)	1×10^{-4} (reduce on plateau)
Loss	
Task 1 loss	MSE
Task 1 loss weight	1
Task 2 loss	MSE
Task 2 loss weight	1

Table 5.2: Parameters fed to the simulator to generate the ensemble-averaged covariance matrices to be used as input to the FCNN.

the magnitudes of σ_{11}, σ_{13}, σ_{22}, and σ_{33} are used as the input to the FCNN, while dropping the only phase: this choice was made to avoid the possible numerical instabilities caused by the phase values being completely different in range with respect the magnitude values.

The whole dataset – which is huge, with 4.5×10^6 elements – was randomly split in three parts for the various stages of the learning phase: 70 % for training, 20 % for validation, 10 % for test. After the partitioning, each part was divided in batches of 128 elements, to perform the training efficiently.

The FCNN architecture is a custom design, which exploits the advantages of multi-task learning (MTL). MTL, as described in [92], is an inductive transfer method that improves generalization by learning related tasks in parallel using shared representations. The core idea is that what is learned for one task can help other tasks be learned more effectively. This is realised by having a normal FCNN, and then create n branches (for n tasks) with their own hidden layers and then output layers. Considering that generally a FCNN is a Multi-Layer Perceptron (MLP) using the back-propagation algorithm, the common hidden layers transfer what they learn to all the n tasks, so that all of them can use those features while focusing on learning their tasks.

Here, we consider the retrieval of μ and λ as two separate tasks; this means that the FCNN will have two branches. The network architecture starts with the input layer, which accepts the aforementioned four magnitudes selected from the covariance matrix; after that, there is the only common layer with 128 units. All the units in this layers are then connected to the two branches, both having three hidden layers with 64, 32, and 16 units, respectively. At the end of each branch, there is a output layer, with only 1 unit, with neither normalisation nor activation function.

All the hidden layers in the network (common and per branch) normalise their input data (input from the previous layer multiplied by the weights matrix and adding the biases vector) before passing it to the activation function; the reason behind this is the problem of having inputs to the neurons – and their activations – with a great variance, making the learning unstable. The normalisation is achieved by using the Layer Normalization (LN) technique, designed to accelerate and stabilise the training of DL neural networks [93]. This technique was created to solve the problems of Batch Normalization (BN), mainly the requirement of large mini-batches to compute stable mean and variance statistics and the different behaviour of the layer during training and inference. LN, instead, normalises across the neurons in a layer rather than across the batch dimension; for each layer, this technique normalises the outputs of the neurons by using a mean μ and a standard deviation σ defined as:

$$\mu = \frac{1}{H} \sum_{i=1}^{H} a_i, \qquad \sigma = \sqrt{\frac{1}{H} \sum_{i=1}^{H} (a_i - \mu)^2} \tag{5.14}$$

where H is the number of neurons, and a_i is the output of the ith neuron.

After having normalised, the output of this layer goes to the activation function; in this case, amongst the various alternatives, the chosen one was the gaussian-error linear unit (GELU), which smooths the classical rectified linear unit (ReLU) in the region close to 0 by having a "bump" with negative derivative to the left of 0. This avoids numerical instabilities when values are close to 0.

The model was trained using the *Adam* optimiser with a constant learning rate (LR) of 1×10^{-4}. Although there was no LR scheduler, the Reduce-On-Plateau strategy was applied, reducing LR by a factor of 0.2 when the training loss reduction was less than 1×10^{-1} for 4 successive epochs; the admitted minimum LR was 1×10^{-6}. The loss function was MSE for both tasks; to help the training, some penalties related to the weights and biases of the hidden layers were used, adding a *L2 regularisation* with a factor of 1×10^{-3} for the weights, and a *L1 regularisation* with a factor of 1×10^{-3} for the biases. Thus, the complete loss function is given by:

$$L = \alpha_\mu \frac{1}{N} \sum_{n=1}^{N} \left\| \hat{\mu} - \mu \right\|_2^2 + \alpha_\lambda \frac{1}{N} \sum_{n=1}^{N} \left\| \hat{\lambda} - \lambda \right\|_2^2 + \alpha_{\underline{\mathbf{W}}} \left\| \underline{\mathbf{W}} \right\|_F^2 + \alpha_{\mathbf{b}} \left\| \mathbf{b} \right\|_1 \tag{5.15}$$

where α_μ, α_λ, $\alpha_{\underline{\mathbf{W}}}$, and $\alpha_{\mathbf{b}}$ are the weights of each elements of the loss function – 2 MSE, L2 and L1 regularisations; N is the number of samples in a batch, $\underline{\mathbf{W}}$ is the weight matrix of the entire network, $\mathbf{b}$ is the biases vector of the entire network, $\|\cdot\|_F$ is the Frobenius' norm operator, and $\|\cdot\|_1$ is the taxicab norm operator.

Early stopping was employed to mitigate overfitting, and model checkpoints were saved based on training loss. The training was performed for 46 epochs – instead of 50 because of early stopping – using a batch size of 128 on a NVIDIA RTX 3080Ti, working with the TensorFlow framework through Keras API.

5.4 Results

The performance of the designed model was tested in several ways. To perform the inference phase, the whole dataset – training, validation and test parts – was passed as input to the trained model. In the following, the validation of the model is performed by evaluating several metrics and variables in the whole dataset, which can be represented as a 2D space in μ and λ, thus representing the results of these metrics as *heatmaps*. The parameters used to consider the entire

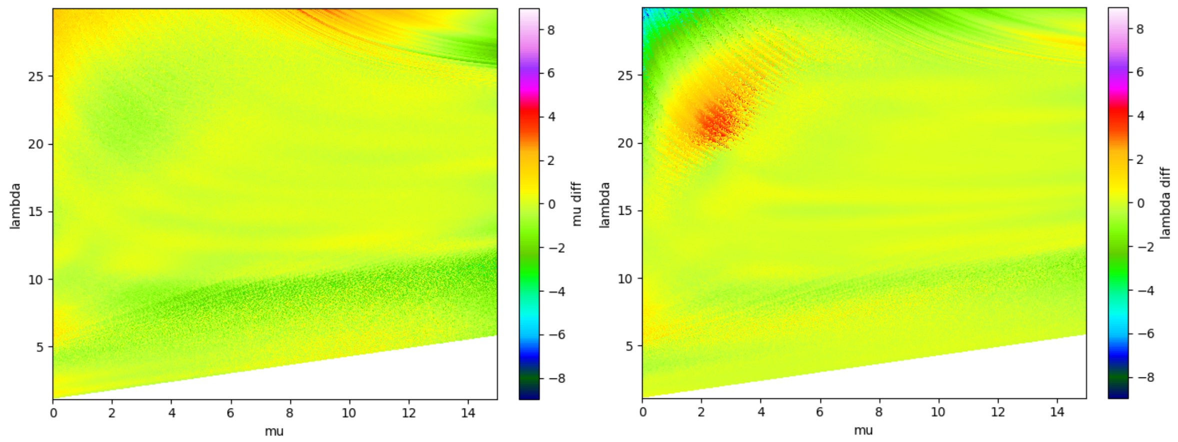

(a) $\hat{\mu} - \mu$ **(b)** $\hat{\lambda} - \lambda$

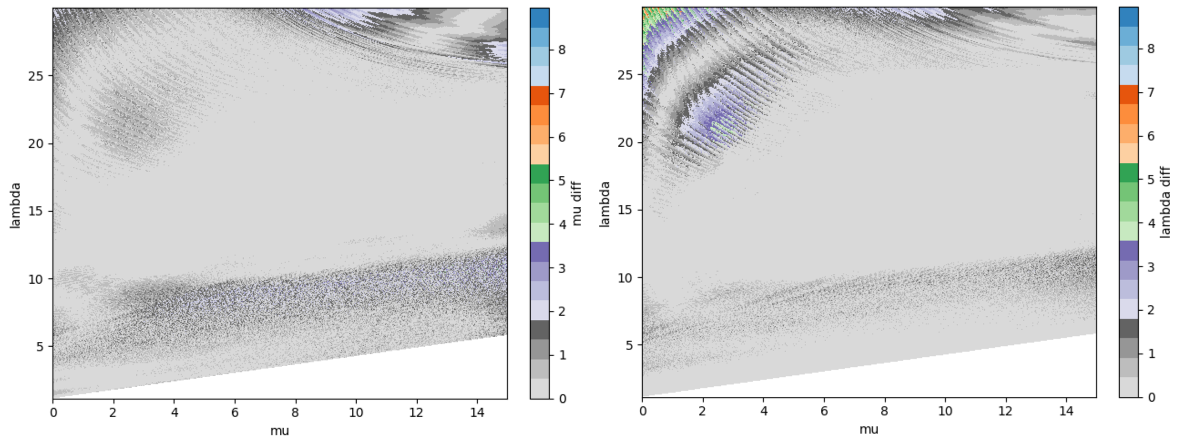

(c) $|\hat{\mu} - \mu|$ **(d)** $|\hat{\lambda} - \lambda|$

Figure 5.4: Heatmaps containing the errors between the estimated parameter and the true one for both μ and λ. In the figures, both the signed and the absolute errors are shown, as indicated in the caption of every figure. In general, in this range of parameters, both the errors are not so big, except for some small regions, leading to a possible problem in the total number concentration of the DSD.

space, are the true ones and not the estimated ones. The evaluated variables are:

- the errors (absolute and signed) on μ and λ;
- the probability density functions of μ and λ;
- two variables deriving from the DSD, the median diameter D_0 and the terminal velocity V_T;
- the *Kullback-Leibler divergence* on the normalised DSDs;
- the total number concentration ratio between the predicted and true DSD.

Moreover, to understand the generalisation limits of the proposed model, a change in radar frequency was explored – even though the theoretical model used to generate the input data started with the assumption of the Rayleigh regime. After the evaluation of the

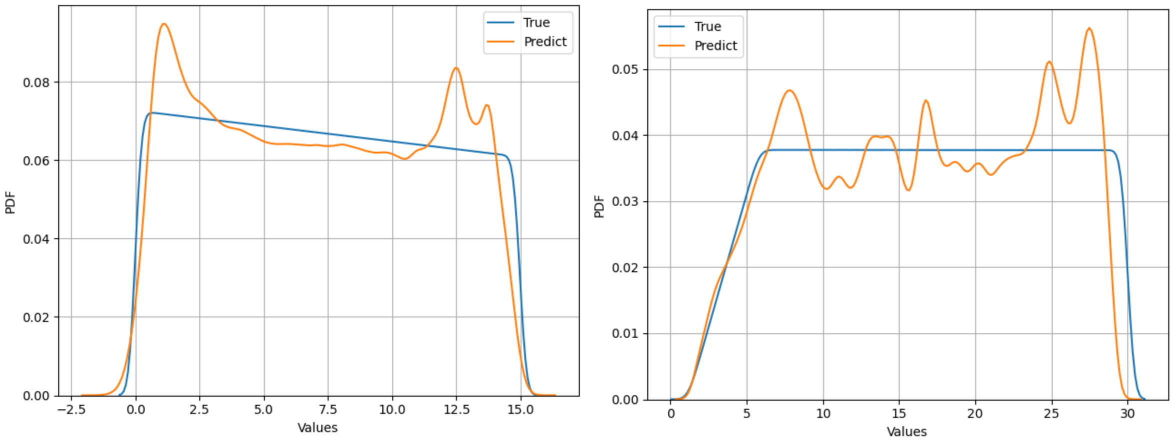

(a) μ PDF

(b) λ PDF

Figure 5.5: PDFs for μ, λ and their estimated versions. The distributions of the predicted quantities mostly follow the ones of the true parameters. Problems arise towards the edges of the intervals, but with no big concentrations around a single value.

model by looking at the variables listed above, a comparison of the results obtained by testing the proposed methodology with different radar frequencies will follow.

Parameters errors

The signed and absolute errors on μ and λ is a simple measure of how precise was the prediction. These errors are reported in Figure 5.4.

The coordinates of each point in the heatmap are given by the (μ, λ) values in the true inference sample, while the color of that point is given by the difference between the estimated parameter during interference and the true one (as indicated in the caption of every sub-figure). The errors (both signed and absolute) are very small for both μ and λ, except for some regions, where the error grows.

Parameters PDFs

Another variable worth evaluating is the probability distributions of the parameters, which are depicted in Figure 5.5.

Both parameters' PDFs are almost equal to the true ones. The $\hat{\mu}$ PDF is very precise in the central values of μ, while there is a difference in the values close to the edges of the intervals. The same trend can be seen for $\hat{\lambda}$, except that the upper limit of the distribution is at a lower value with respect to λ. Also, there is no value going outside these intervals, meaning that there are no DSD shapes different from the ones in this analysed in this space.

Median diameter

The median diameter D_0 is one of the variables describing the properties of the cloud of raindrops that derives directly from the DSD. This variable is defined as the diameter which divides the DSD such that half of the liquid water content (LWC) – which is another variable – is due to drops with diameters greater than D_0; mathematically,

$$2\int_0^{D_0} D^3\, N_0\, D^{\mu}\, e^{-\lambda D}\, dD = \int_0^{\infty} D^3\, N_0\, D^{\mu}\, e^{-\lambda D}\, dD \qquad (5.16)$$

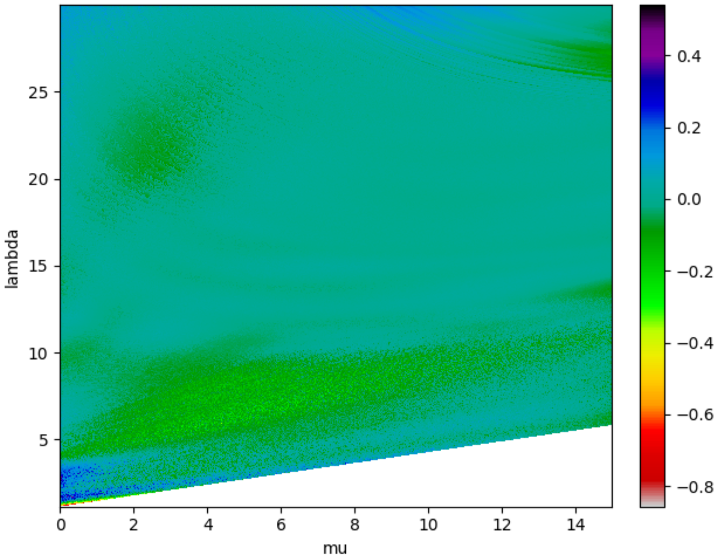

Figure 5.6: Heatmap depicting the difference in the median diameter between the estimated and the true DSD. The difference is expressed in mm, as the diameters are generally used in mm. The differences between the median diameters coming from the predicted DSDs and the ones coming from the true DSDs are very small, thus maintaining the distribution of the liquid water content (LWC) in the unit volume.

The difference between the median diameters between the estimated and the true DSDs is shown in Figure 5.6. Each point of the heatmap is a combination of true (μ, λ) – i.e. a sample in the dataset – to which corresponds a combination of predicted ($\hat{\mu}$, $\hat{\lambda}$). Computing the median diameter for both the DSDs coming from these combinations, leads to two values, $D_0(\mu, \lambda)$ and $D_0(\hat{\mu}, \hat{\lambda})$; by subtracting these two median diameters for each combination, the spectrum in the figure is obtained. By observing its values, one can notice that the difference (in mm) is very small, and increases only for small values of μ and λ. A small difference means that the LWC calculated before and after D_0 is equal to the one related to the true DSD.

Reflectivity-weighted mean terminal velocity

In the same way as for the median diameter, another variable deriving from the DSD is the *reflectivity-weighted mean terminal velocity*, which relates the the fall velocity of a particle of diameter D with the reflectivity at the same diameter, as defined in [94]. The mathematical definition is given by:

$$V_T = 9.65 - 10.3\left(1 + \frac{0.6}{\lambda}\right)^{-(\mu+7)} \qquad (5.17)$$

Following the same process as the median diameter, the results are shown in Figure 5.7.

The trend of the difference between these velocities coming from the estimated and true DSDs is similar to the median diameter,

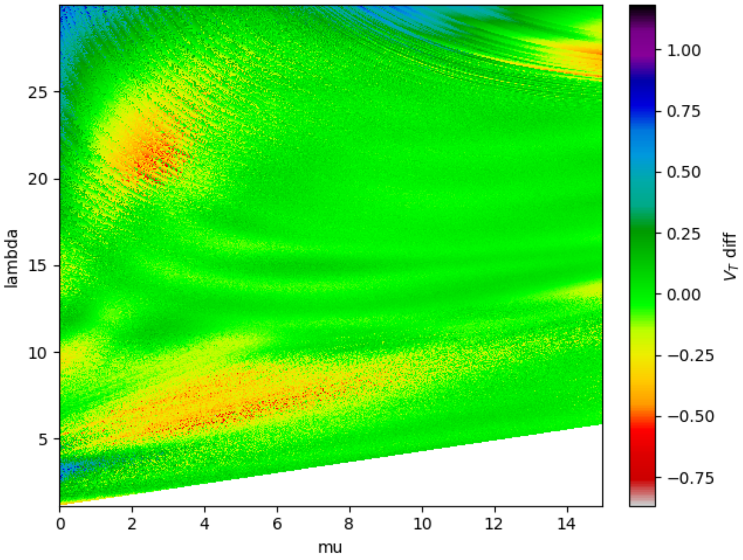

Figure 5.7: Heatmap depicting the difference in the reflectivity-weighted terminal velocity between the estimated and the true DSD. The difference is expressed in $\mathrm{m\,s^{-1}}$.

with no great differences between the two, considering each (μ, λ) combination.

Kullback-Leibler divergence

Another way to compare the results of the prediction, is to actually compare the shapes of the predicted and true DSDs. By normalising both distributions for their 0th-order moment, the PDFs deriving from the DSDs are obtained; these are scaled in magnitude (compared to the DSDs), but maintain the shape of the distribution. At the same time, they can be compared with well-known methods to compare PDFs. In this case, the *Kullback-Leibler divergence* from information theory was used, which is defined as:

$$D_{KL}(\mathbb{P}_T \parallel \mathbb{P}_P) = \sum_{D \in \Delta} \mathbb{P}_T(D) \log \frac{\mathbb{P}_T(D)}{\mathbb{P}_P(D)} \tag{5.18}$$

where $\mathbb{P}_T$ and $\mathbb{P}_P$ are the PDFs of the true and predicted DSDs, respectively. This divergence derives from the definition of entropy in information theory; thus, a value close to 0 means that the distributions are very close (or equal), while a bigger value means they are far apart. The result for this are presented in Figure 5.8.

The resulting divergences for each (μ, λ) combination are almost zero in the whole space, meaning that the shape of the true DSD was fully recovered in the estimated one. Although there are regions with mildly higher values (reaching divergences of 0.5 or a little less), the true region with higher values is the top left corner, with very low μ and high λ.

Total number concentration

The final variable to look at is the total number concentration, which is the 0th-order moment of the DSD. It is given by:

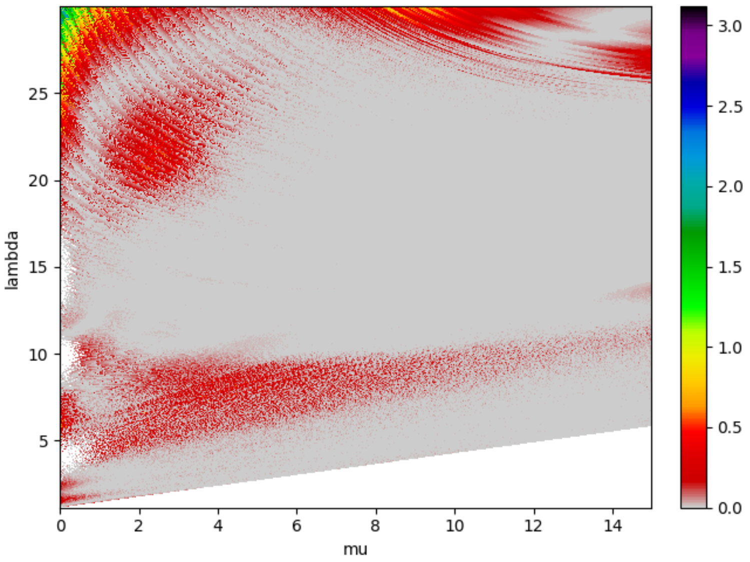

Figure 5.8: Heatmap depicting the Kullback-Leibler divergence between the estimated and the true DSD. It can be noticed that its value it is almost always 0, meaning the shapes of the DSDs for all the combinations are well predicted.

$$N_T = \int N_0 D^{\mu} e^{-\lambda D} dD \tag{5.19}$$

Since this is the magnitude of the DSD, i.e. the total number of particles in the unit volume, it makes sense to compute the ratio between the predicted and true DSD, for each (μ, λ) combination. Such computation is reported in Figure 5.9.

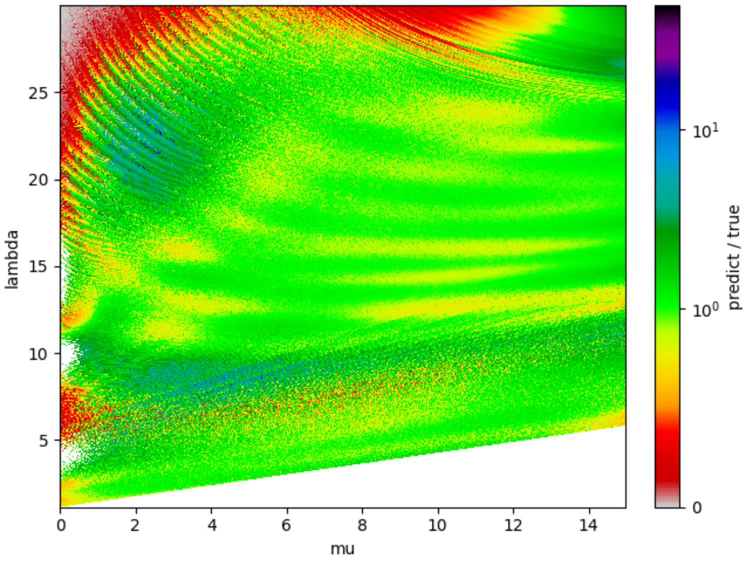

Figure 5.9: Heatmap showing the ratio of the total number concentration between the estimated and the true DSD. The prediction is mostly good, except for the region at the left and top borders.

Most of the values in the picture are around 1, meaning that the network also estimated well the total number of particles in the unit volume. From this plot, and considering the plots related to the errors in parameters estimations (see Figure 5.4), it is worth to notice that with this method, and when the errors between the real and the estimated parameters gets bigger, the shape of the estimated DSD is not really affected by it, while the total number of particles inside the reference volume is greatly affected, thus changing the intensity of the phenomenon.

5.4.1 Frequency dependence

Frequency is one of the most important variables to consider when evaluating the generalisation of the proposed method, since weather radars adopted in meteorology span several radar bands (S, C, X, K). The FCNN model described in the previous sections was designed to work with data generated at 2 GHz. To test it against data collected at other radar frequencies and being able at the same time to make the comparisons between the various operating frequencies, these steps were performed (for each frequency):

1. Training stage with the same parameters as the ones described in Subsection 5.3.2 and in Table 5.2, but using another dataset; data were generated with the parameters listed in Subsection 5.3.1 and in Table 5.1, but changing the radar frequency and the electric permittivity of water. This resulted in a generated dataset for each frequency tested.
2. Inference stage with the new trained model and the newly generated dataset at the related frequency.

Considering the theoretical model exposed in Subsection 5.2.1 (particularly the formulae in Equation 5.4), the variables that change with the frequency are the wavelength in free space and the polarisability, which depends on the electric permittivity ε_w of the water. Thus, the choice of the frequencies was based on the availability of tabular data for ε_w in [87]. See Table 5.3 for the chosen values, which range in S, C, and X radar bands. The main problem with the formulae in Equation 5.4 is that they are obtained after simplifying the general scattering equations by using the Rayleigh assumption, which does not really apply to the higher bands, such as the X one.

Table 5.3: Frequencies and water permittivities adopted to train the FCNN.

Frequency	ε_w
2 GHz	$77.9 + j\,7.57$
3.417 GHz	$76.4 + j\,12.9$
5.3 GHz	$73.1 + j\,18.7$
6 GHz	$71.9 + j\,20.6$
7.9 GHz	$67.8 + j\,25.7$
10.45 GHz	$61.1 + j\,30.2$

The following results are obtained by using the variables and indices considered in the previous section, which were computed during the inference stage for all the tested frequencies. Generally, the estimation of the DSD shape is quite good across the analysed frequencies, with a little to none degradation of the estimation gradually introduced with the frequency increase. Despite this, it can be observed that performances related to some indices greatly worsen with the increasing frequency.

The first important indices to look at are the errors in the DSD parameters estimations, which are depicted in Figure 5.10 (errors on μ) and in Figure 5.11 (errors on λ).

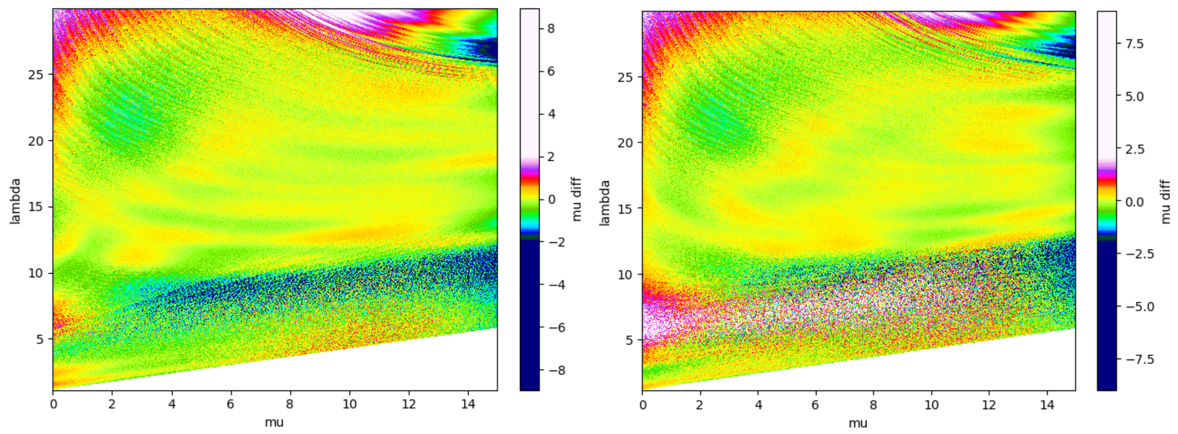

(a) $\hat{\mu} - \mu$ @ 2 GHz

(b) $\hat{\mu} - \mu$ @ 3.417 GHz

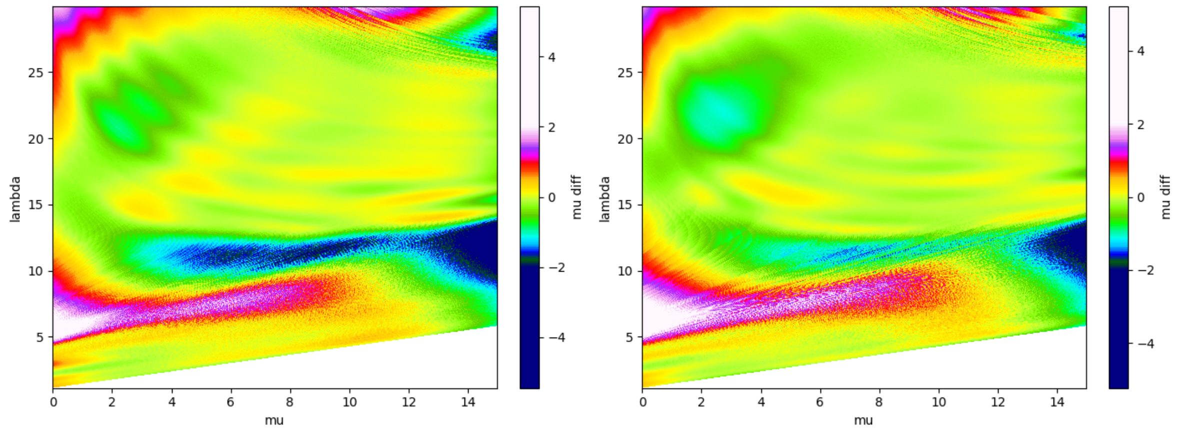

(c) $\hat{\mu} - \mu$ @ 5.3 GHz

(d) $\hat{\mu} - \mu$ @ 6 GHz

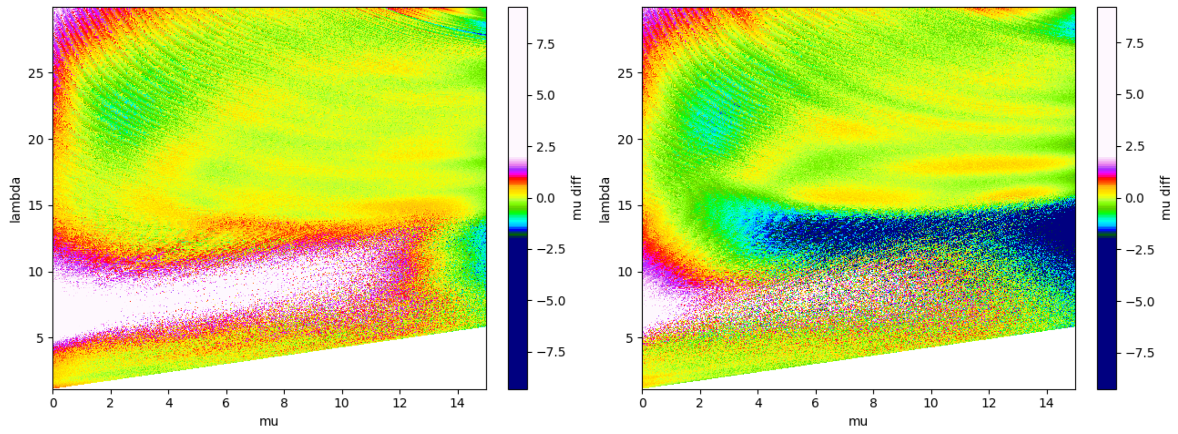

(e) $\hat{\mu} - \mu$ @ 7.9 GHz

(f) $\hat{\mu} - \mu$ @ 10.45 GHz

Figure 5.10: Heatmaps containing the errors between the estimated μ parameter and the true one for all the analysed frequencies. In the figures, the signed errors are shown, with the white and blue areas denoting the regions where the absolute error is equal or greater than 2. In general, the errors are not so big in this range, except for the white and blue regions, leading to a possible problem in the total number concentration of the DSD. It can be observed a degradation of estimation for lower values of λ (lower region of the figure) with the increase of the frequency.

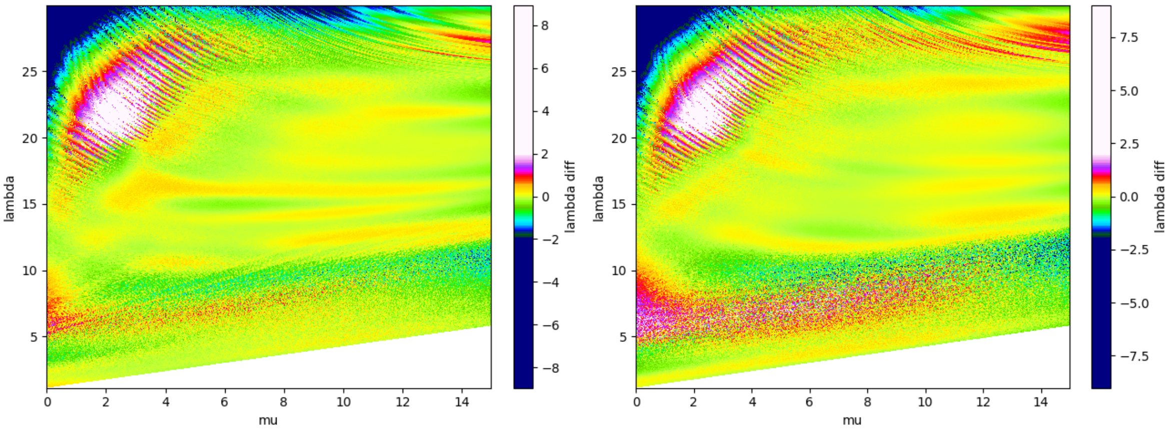

(a) $\hat{\lambda} - \lambda$ @ 2 GHz **(b)** $\hat{\lambda} - \lambda$ @ 3.417 GHz

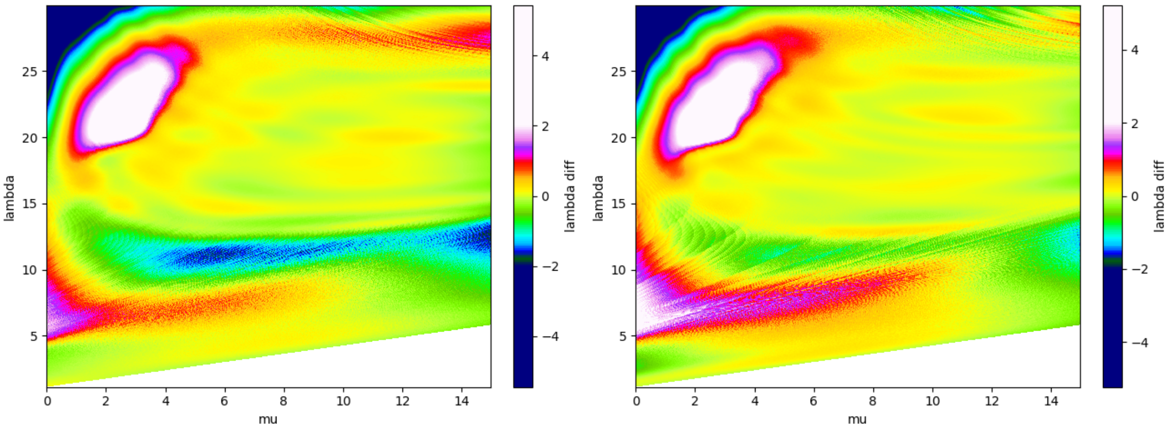

(c) $\hat{\lambda} - \lambda$ @ 5.3 GHz **(d)** $\hat{\lambda} - \lambda$ @ 6 GHz

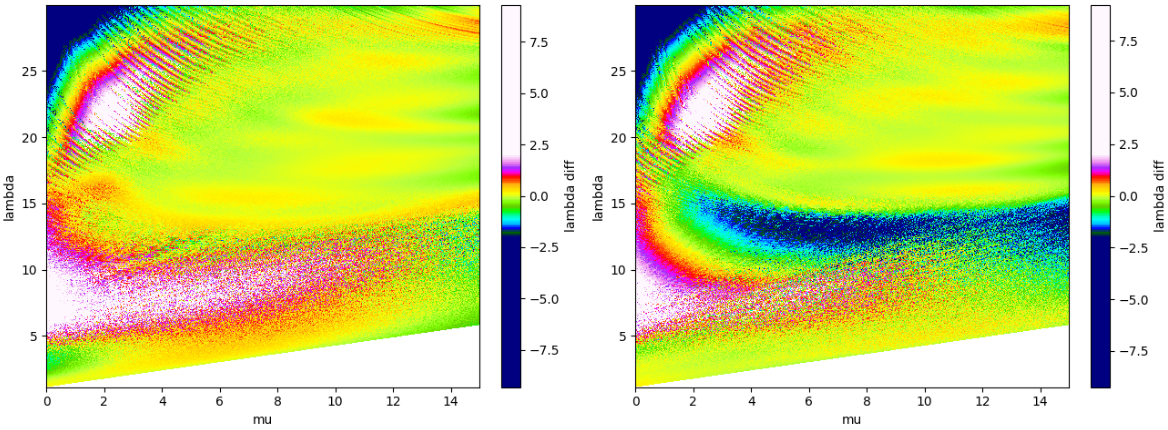

(e) $\hat{\lambda} - \lambda$ @ 7.9 GHz **(f)** $\hat{\lambda} - \lambda$ @ 10.45 GHz

Figure 5.11: Heatmaps containing the errors between the estimated λ parameter and the true one for all the analysed frequencies. In the figures, the signed errors are shown, with the white and blue areas denoting the regions where the absolute error is equal or greater than 2. In general, the errors are not so big in this range, except for the white and blue regions, leading to a possible problem in the total number concentration of the DSD. It can be observed a degradation of estimation for lower values of λ (lower region of the figure) with the increase of the frequency.

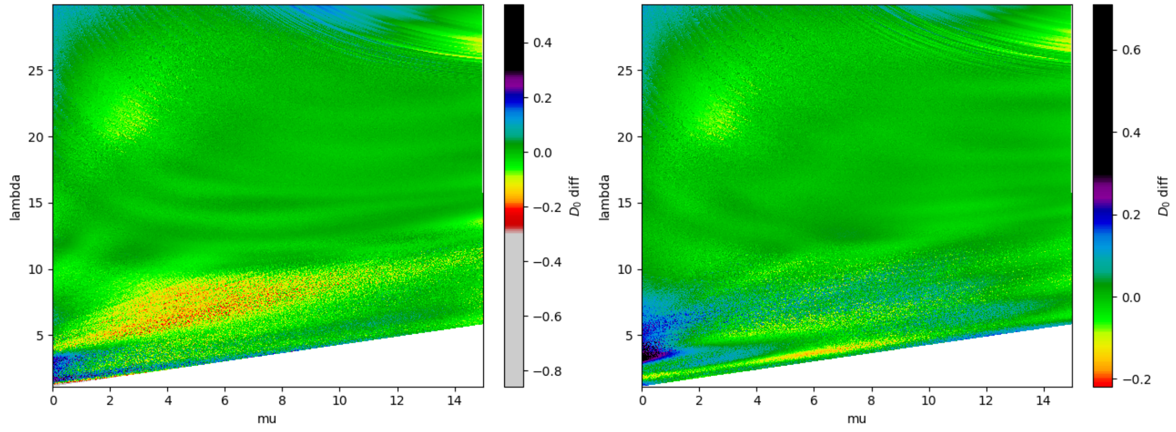

(a) D_0 @ 2 GHz **(b)** D_0 @ 3.417 GHz

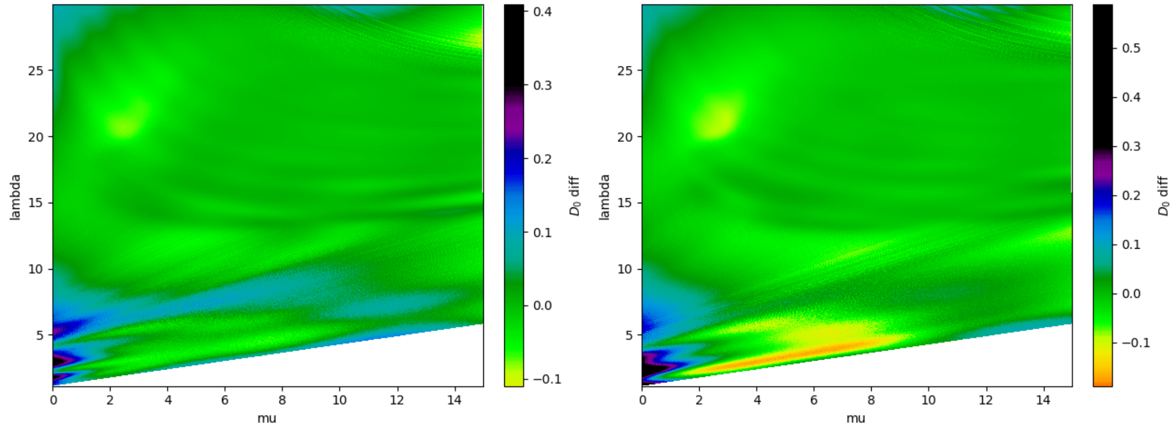

(c) D_0 @ 5.3 GHz **(d)** D_0 @ 6 GHz

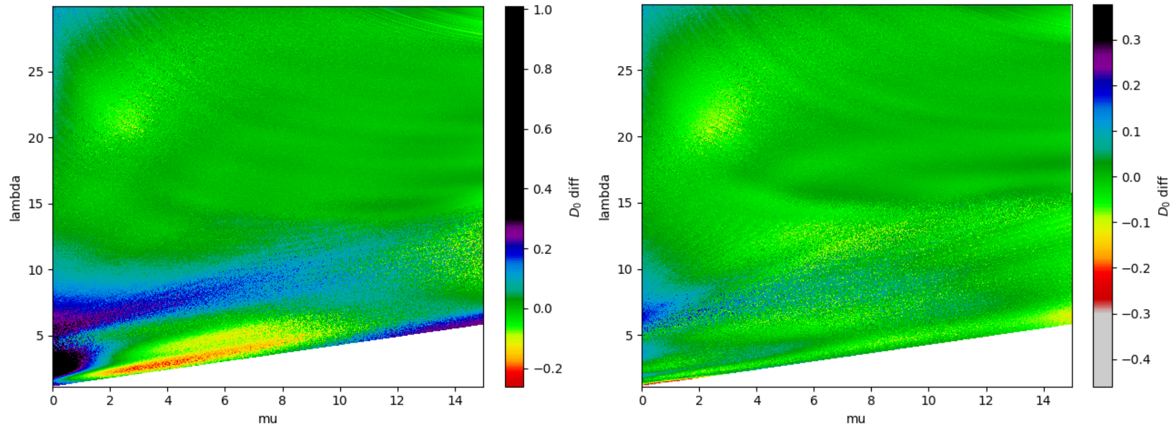

(e) D_0 @ 7.9 GHz **(f)** D_0 @ 10.45 GHz

Figure 5.12: Heatmaps depicting the difference in the median diameter between the estimated and the true DSD. The difference is expressed in mm, as the diameters are generally used in mm. In the figures, the grey and black areas denote the regions where the absolute error is equal or greater than 0.3 mm. The differences between the median diameters coming from the predicted DSDs and the ones coming from the true DSDs are very small, thus maintaining the distribution of the liquid water content (LWC) in the unit volume. It can be observed a degradation of estimation for lower values of λ and μ (lower left region of the figure) with the increase of the frequency.

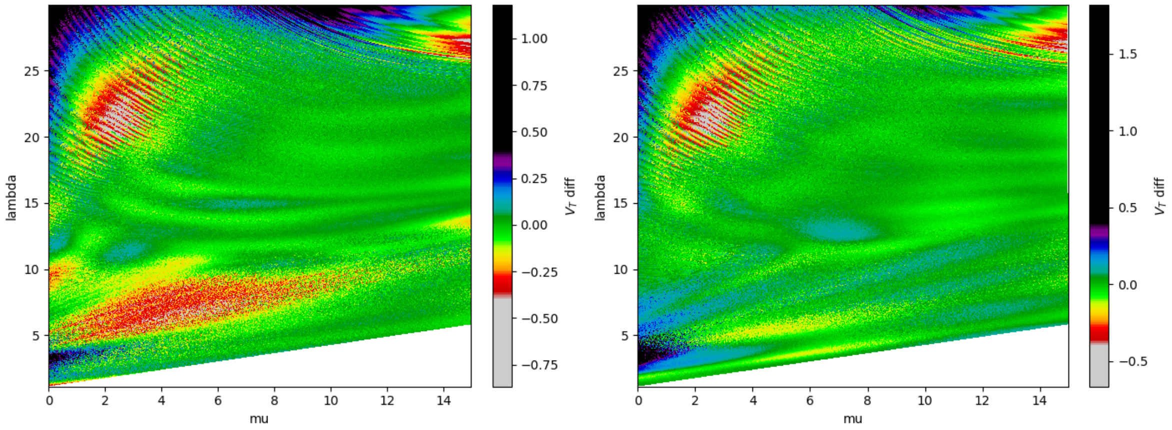

(a) V_T @ 2 GHz **(b)** V_T @ 3.417 GHz

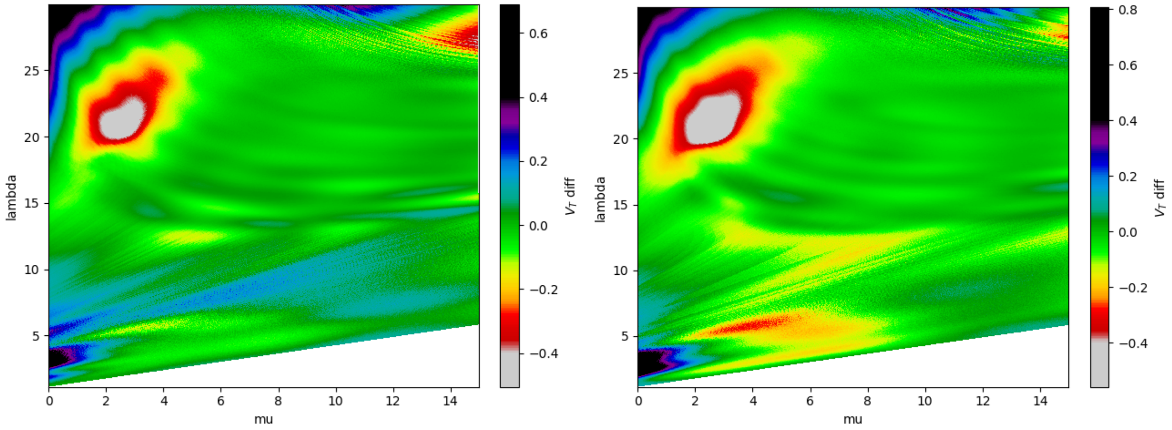

(c) V_T @ 5.3 GHz **(d)** V_T @ 6 GHz

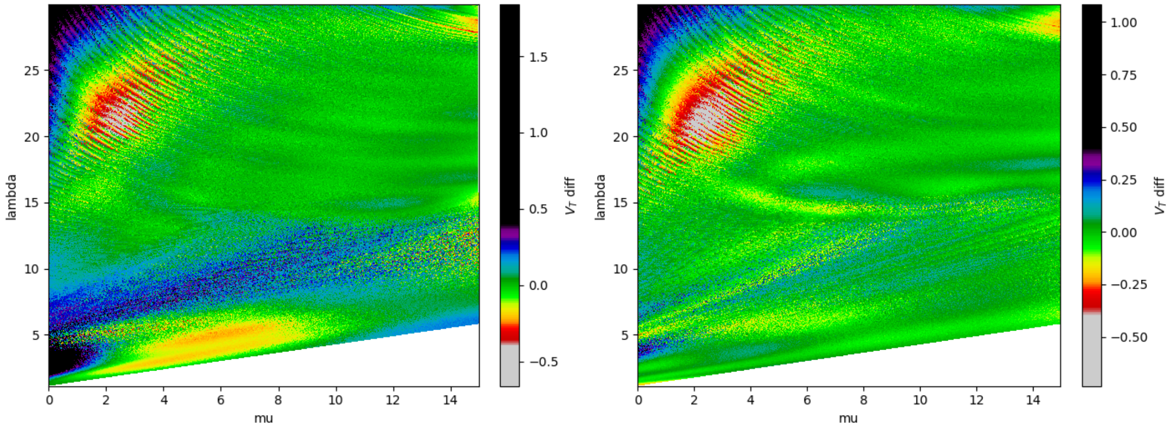

(e) V_T @ 7.9 GHz **(f)** V_T @ 10.45 GHz

Figure 5.13: Heatmaps depicting the difference in the reflectivity-weighted terminal velocity between the estimated and the true DSD. The difference is expressed in $\mathrm{m\,s^{-1}}$. In the figures, the grey and black areas denote the regions where the absolute error is equal or greater than $0.4\,\mathrm{m\,s^{-1}}$. The differences between the terminal velocities coming from the predicted DSDs and the ones coming from the true DSDs are very small. There is not a clear degradation of estimation for with the increase of the frequency.

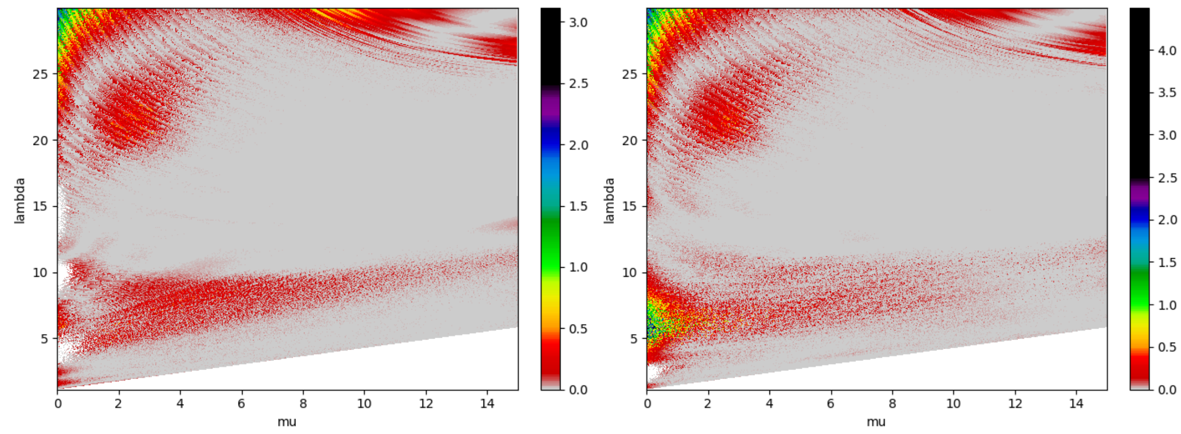

(a) D_{KL} @ 2 GHz **(b)** D_{KL} @ 3.417 GHz

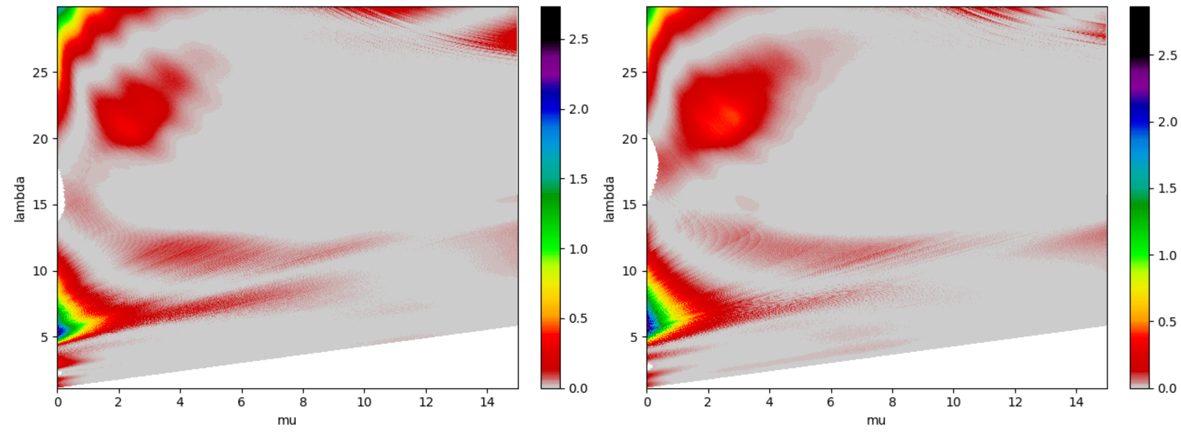

(c) D_{KL} @ 5.3 GHz **(d)** D_{KL} @ 6 GHz

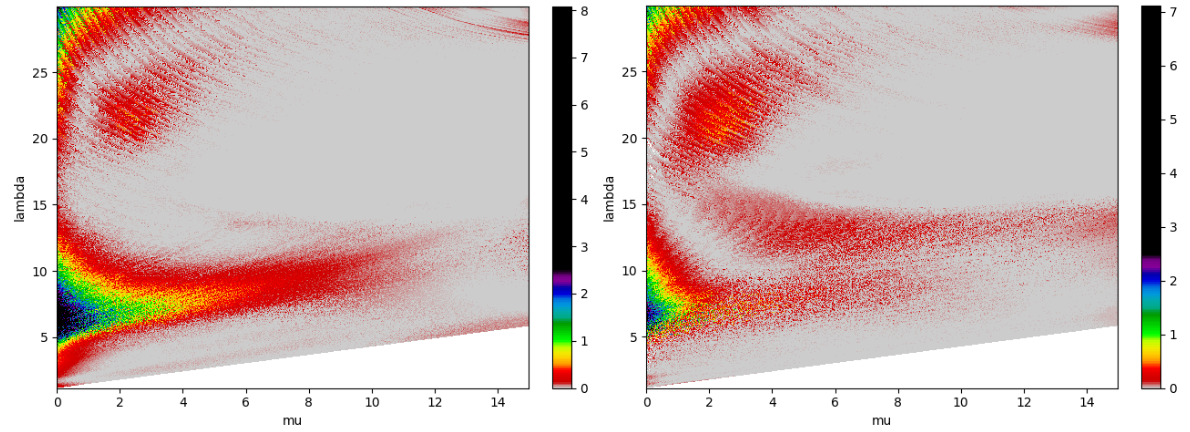

(e) D_{KL} @ 7.9 GHz **(f)** D_{KL} @ 10.45 GHz

Figure 5.14: Heatmaps depicting the Kullback-Leibler divergence between the estimated and the true DSD. In the figures, the black areas denote the regions where the divergence is equal or greater than 2.5. It can be noticed that its value it is almost always very close to 0, meaning the shapes of the DSDs for all the combinations are well predicted; although, a slight degradation in the shape estimation can be observed with the increase of the frequency in the lower left region on the heatmap (low μ and low λ).

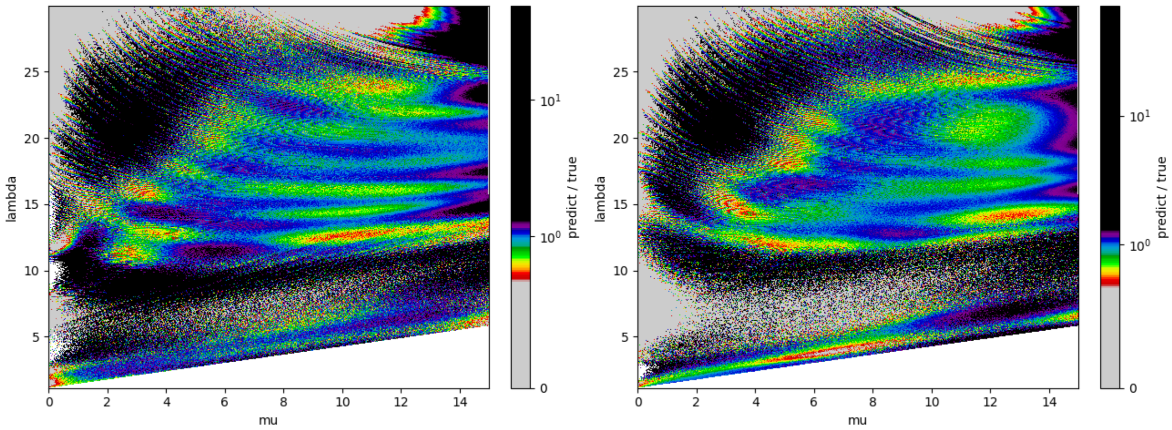

(a) N_T @ 2 GHz

(b) N_T @ 3.417 GHz

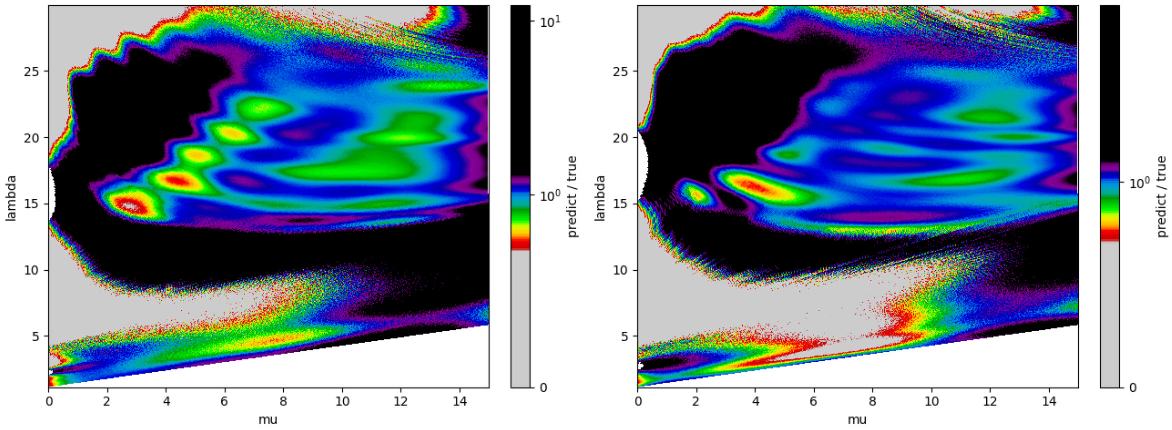

(c) N_T @ 5.3 GHz

(d) N_T @ 6 GHz

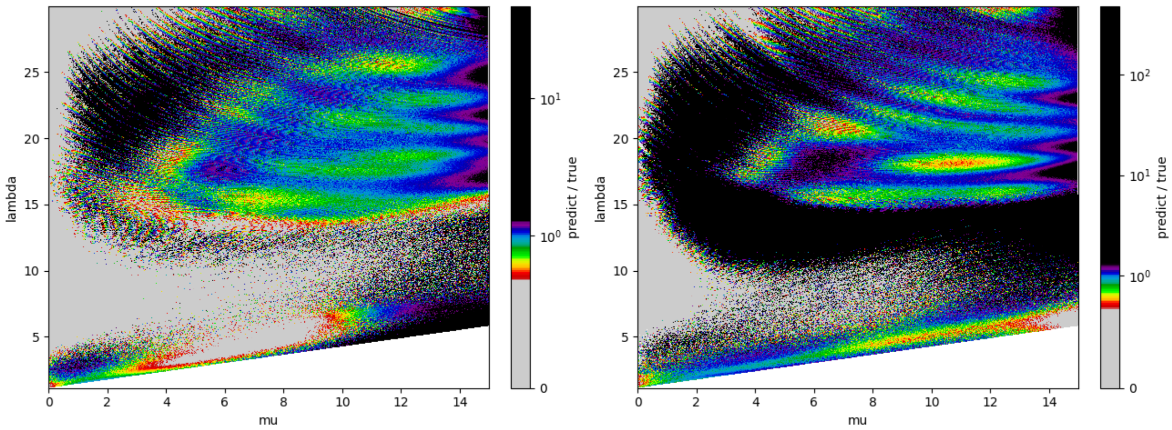

(e) N_T @ 7.9 GHz

(f) N_T @ 10.45 GHz

Figure 5.15: Heatmaps showing the ratio of the total number concentration between the estimated and the true DSD. In the figures, the black and gray areas denote the regions where the ratio is equal or greater than 1.3 and equal or lower than 0.7, respectively. The coloured regions represent very good ratio values. Here, the degradation due the increase of the frequency is very strong, mostly present in the bottom and top left regions.

The overall accuracy deteriorates with the frequency increase for combinations of parameters with low values of λ (bottom region of the plot) and for combinations with high values of λ and low values of μ (top left corner of the plot). A similar behaviour can be noticed in the estimation of the total number concentration (shown in Figure 5.15), confirming that a variation in DSD parameters can significantly impact the total number of particles inside the reference volume, thus changing the intensity of the phenomenon.

Nonetheless, this lack of accuracy does not affect the estimation of the DSD shape, as it can be observed from the plots in Figure 5.14. Here, the Kullback-Leibler divergence has values close to zero almost in the whole (μ, λ) region for all the tested frequencies; the only region where its value gets bigger is the bottom left part of the plot (low values of both μ and λ), and this can be observed for all the frequency, except 2 GHz.

Another index that is directly connected to the shape of the DSD – because of its definition – is the median diameter D_0, with its estimation being shown in Figure 5.12. The plots show how accurately the median diameter is estimated, meaning that the distribution of the LWC across the drop diameters is predicted with very good precision.

Another variable used in this comparison is the reflectivity-weighted terminal velocity, which is a flux variable of the DSD; the related plots are shown in Figure 5.13. Even though this variable is not really related to the shape of the DSD or the total number of particles in the reference volume, it can be noticed that the proposed FCNN model is capable of retrieving it in a good way for all the tested frequencies.

5.5 Conclusions

Here, a novel approach for DSD estimation was presented. Starting from the full polarimetric information given by an ensemble-averaged covariance matrix, a Deep Learning FCNN was designed, featuring the implementation of novel techniques such as multi-task learning and Layer Normalization to stabilise and shorten the learning process, along the augmentation of learning common features for different tasks (objectives). The designed model aims at retrieving the parameters of the distribution of the number of particles characterising a unit volume, which is modelled as a traditional gamma DSD. The results show that this model is capable of estimating the DSD parameters from the features contained in a ensemble-averaged covariance matrix, returning a small error that does not affect the shape and slope of the statistical distribution and some related rain variables, such as the median diameter or the terminal velocity. As expected, the estimation of the total number concentration needs some improvements, although the results here are mostly acceptable.

Conclusions 6

Amongst the various applications in remote sensing, leveraging the power of different instruments, the ones presented in this thesis are very important for their respective types of remote sensing.

Detection and localisation tasks, which are generally performed together (with the second usually depending on the first), are very common in passive remote sensing, where the instruments are often used to observe and monitor phenomena and targets; examples may be the monitoring performed with imaging instruments (visible and thermal cameras, LiDAR) or the tracking of little transmitting targets working in radio frequency (RF).

One of the most discussed and applied techniques is the direction of arrival (DoA) estimation when working with networks of antennas or an antenna array as sensing device. Many solutions have been proposed to this problem, applying also very different strategies. This thesis focus on bringing novelty into two specific directions of improvement: the study of an appropriate antenna for the problem at hand, its interaction with the signal processing methods and frameworks to perform the estimation, and the assessment of the performance reached by the proposed methodology.

The design of the antenna is the first aspect to take care when dealing with a specific custom problem, shortly followed by the exploitation of its properties in the signal processing chain. The novelty proposed here analyses the usage of circular polarisation (CP) and of embedded radiation patterns (ERPs) directly measured on the antenna design (physically or in an accurate simulation) and combining it with the most common algorithms used in literature, i.e. MUSIC and Bartlett. As seen in the dedicated chapter, this approach enhances the performances of these algorithms compared to the classical approach, where the conventional steering vector (CSV) are analytically computed, thus missing the real physical properties of the measuring device. Moreover, the performances shown are influenced positively by the choice to design the antenna with right-handed circular polarisation (RHCP), which is more resistant to noise and reflections generated by the environment's obstacles and limits.

In addition to starting with a very well designed hardware and the seamless integration of its properties in the processing methods, it is important to evaluate in the best possible way the performances of the developed system and strategy. In DoA literature, this aspect is taken care in very different ways across the many existing solutions, thus lacking of a reference method to compare evaluations. Even if there are some very common methods that are the mostly used, these many times do not take into account the physical geometry of the problem. In fact, the most common used metrics to compare the true and estimated DoA – which are generally expressed through angles – are the ones taken from classical statistics, such as root mean square error (RMSE). Here, a novel metric is proposed, which treats the direction of arrival as a vectors in space, thus finding a better way to compare the distance (error) between the true and the estimated one, as shown in the dedicated chapter.

While in passive remote sensing the received signal is transmitted by the target itself, in active remote sensing is the sensing system that does that. This makes this type of remote sensing very adapt to measure the electromagnetic properties of a material, since the emitted wave is fully known, as it is accurately designed for the specific problem and the wanted properties to analyse; thus, the response of the target can be compared with the transmitted one, discerning the characteristics of the measured target.

This approach is very useful when measuring physical phenomena, where many times there is very little or inaccurate knowledge of the phenomenon itself. Amongst the various applications and their aims, a very common one is the measurement of meteorological phenomena, such as rain. When measuring such phenomenon, a cloud of particles – hydrometeors, for rain specifically – interacts with the atmosphere, generating a precipitation phenomenon. To accurately measure the phenomenon, its important to know its structure and its properties. In this context, one of the most analysed problem is the estimation of the drop size distribution (DSD), which statistically models the number of particles and their distribution with respect to the drop size – generally expressed through the diameter of an equivolume spherical particle – in a unit volume; the statistical modelling is necessary, since at the moment of writing there is no instrument capable of measuring the particles one by one. Through the years, many different methods were proposed, bringing novelty in both the used instrumentation (e.g., from using single radars to dual-radars measurements or combining radars and other devices such as disdrometers) and the used processing chains due to the enhancement of processing devices and techniques. The latest development exploit the usage of polarimetric weather radars, capable of giving more information about the shape of the particle and their response in two different orthogonal polarisations – i.e. linear (vertical and horizontal) and circular (right and left). At the same time, the developments in the machine learning (ML) field brings new way to deal with the acquired data.

In this work, a novel approach combining polarimetry and the latest developments in ML is proposed. From the radar polarimetric measurements, the ensemble-averaged covariance matrix is extracted, which combines the information from both polarisations by correlating the different scattering factors, averaged for the properties of the particles in the unit volume, such as the DSD and the particle orientation distribution (POD). The elements of this matrix are then fed to a Deep Learning (DL) fully connected neural network (FCNN) integrating a multi-task learning (MTL) approach, which let the neural network learn different objectives at the same time. In this case, the objectives are the parameters of the chosen model for the DSD, which is the traditional gamma DSD, one of the most used distributions. As shown in the related chapter, the network learns quite well the standalone features and representations per task, as well as the ones that span across both tasks. The result show a very precise retrieval of the shape of the DSD, thus estimating very well the variables deriving from the distributions, such as the median diameter.

Future research directions

Even though the results in the studies discussed in this thesis represent novelties for the respective fields, there is a lot of directions to follow to improve these results.

For the DSD estimation part, the new approach was used with very well known analytical algorithms to solve the direct problem. Considering the improvement given with the current approach, it may reach new performance levels if applied to data-driven approaches in ML, since both the ERPs and a massive quantity of measurements to be used as dataset can be acquired through antenna testing in real world. At the same time, it can be considered to implement the proposed metric as a loss function in a DL approach or in a ML one in general.

The proposed method for DSD parameters retrieval also has many ways in which can be improved. It may be worth expanding it in several direction, such as a multi-frequency approach or one that is capable of accurately measure the total concentration number only using the polarimetric radar measurements; for sure, the biggest improvement would be to generalise the formulation of the DSD, with a generalised model that can become all of the proposed models for the various types of precipitations in all the regions in the world or using an estimation more focused on the distribution itself instead of the parameters of the mathematical model, with the aim to provide a unified framework to macroscopically describe clouds of different types of particles, e.g. hydrometeors and lithometeors originating from sandstorms or volcanic eruptions.

Bibliography

Here are the references in citation order.

[1] Chuan Xu et al. 'Rethinking Building Change Detection: Dual-Frequency Learnable Visual Encoder With Multiscale Integration Network'. In: *IEEE Journal of Selected Topics in Applied Earth Observations and Remote Sensing* 17 (2024), pp. 6174–6188. DOI: `10.1109/JSTARS.2024.3401581` (cited on page 1).

[2] Hoon-Keun Lee et al. 'Passive IoT Optical Fiber Sensor Network for Water Level Monitoring with Signal Processing of Feature Extraction'. In: *Electronics* 12.8 (2023). DOI: `10.3390/electronics12081823` (cited on page 1).

[3] D. Pastina et al. 'Passive Radar Imaging of Ship Targets With GNSS Signals of Opportunity'. In: *IEEE Transactions on Geoscience and Remote Sensing* 59 (2021), pp. 2627–2642. DOI: `10.1109/TGRS.2020.3005306` (cited on page 1).

[4] M. Amani, F. Mohseni, N. Farsad Layegh, et al. 'Remote Sensing Systems for Ocean: A Review (Part 2: Active Systems)'. In: *IEEE Journal of Selected Topics in Applied Earth Observations and Remote Sensing* 15 (2022), pp. 1421–1453. DOI: `10.1109/jstars.2022.3141980` (cited on page 2).

[5] Daniel Peters, K. O. Niemann, and R. Skelly. 'Remote Sensing of Ecosystem Structure: Fusing Passive and Active Remotely Sensed Data to Characterize a Deltaic Wetland Landscape'. In: *Remote Sensing* 12 (2020), p. 3819. DOI: `10.3390/rs12223819` (cited on page 2).

[6] J. Susanne Otto et al. 'Distant RF field sensing with a passive Rydberg-atomic transducer'. In: *Applied Physics Letters* 123.14 (Oct. 2023), p. 144003. DOI: `10.1063/5.0169993` (cited on page 3).

[7] J. C. Vogeler and W. B. Cohen. 'A review of the role of active remote sensing and data fusion for characterizing forest in wildlife habitat models'. In: *Revista de Teledetección* 45 (Feb. 2016), pp. 1–14. DOI: `10.4995/raet.2016.3981` (cited on page 3).

[8] Jianyu Wang et al. 'An Active Object-Detection Algorithm for Adaptive Attribute Adjustment of Remote-Sensing Images'. In: *Remote Sensing* 17.5 (2025). DOI: `10.3390/rs17050818` (cited on page 3).

[9] S. L. Mason et al. 'Improved rain rate and drop size retrievals from airborne Doppler radar'. In: *Atmospheric Chemistry and Physics* 17.18 (2017), pp. 11567–11589. DOI: `10.5194/acp-17-11567-2017` (cited on page 4).

[10] Tianwen Wei et al. 'Remote sensing of raindrop size distribution using the coherent Doppler lidar'. In: *Opt. Express* 29.11 (May 2021), pp. 17246–17257. DOI: `10.1364/OE.426326` (cited on page 4).

[11] R. Saravanan et al. 'Direction of Arrival Estimation using Conventional Subspace Algorithms'. In: *International Journal of Innovative Technology and Exploring Engineering* (2019). DOI: `10.35940/ijitee.h7503.078919` (cited on page 5).

[12] Xiaofei Zhang and Renzheng Cao. 'Direction of Arrival Estimation: Introduction'. In: *Wiley Encyclopedia of Electrical and Electronics Engineering*. John Wiley & Sons, Ltd, 2017, pp. 1–22. DOI: `https://doi.org/10.1002/047134608X.W8343` (cited on page 5).

[13] G. Radha Kumari Ch. Kusuma Kumari. 'Robust Direction of Arrival Estimation using Subspace Methods'. In: *International Journal of Computer Applications* 159.1 (Feb. 2017), pp. 24–29. DOI: `10.5120/ijca2017912686` (cited on page 5).

[14] Zai Yang et al. 'Sparse methods for direction-of-arrival estimation'. In: *Academic Press Library in Signal Processing, Volume 7*. Ed. by Rama Chellappa and Sergios Theodoridis. Academic Press, 2018. Chap. 11, pp. 509–581. DOI: `https://doi.org/10.1016/B978-0-12-811887-0.00011-0` (cited on page 6).

[15] Sujit Kumar Sahoo and Anamitra Makur. 'Signal recovery from random measurements via extended orthogonal matching pursuit'. In: *IEEE Transactions on Signal Processing* 63.10 (2015), pp. 2572–2581 (cited on page 6).

[16] Abhishek Aich and P Palanisamy. 'On-grid DOA estimation method using orthogonal matching pursuit'. In: *2017 International Conference on Signal Processing and Communication (ICSPC)*. IEEE. 2017, pp. 483–487 (cited on page 6).

[17] Maryam Dehghani and Keyvan Aghababaiyan. 'FOMP algorithm for direction of arrival estimation'. In: *Physical Communication* 26 (2018), pp. 170–174 (cited on page 6).

[18] Yuri I Abramovich and Nicholas K Spencer. 'Design of nonuniform linear antenna array geometry and signal processing algorithm for DOA estimation of Gaussian sources'. In: *Digital Signal Processing* 10.4 (2000), pp. 340–354 (cited on page 6).

[19] Keyvan Aghababaiyan, Vahid Shah-Mansouri, and Behrouz Maham. 'High-precision OMP-based direction of arrival estimation scheme for hybrid non-uniform array'. In: *IEEE Communications Letters* 24.2 (2019), pp. 354–357 (cited on page 6).

[20] Keyvan Aghababaiyan, Reza Ghaderi Zefreh, and Vahid Shah-Mansouri. '3D-OMP and 3D-FOMP algorithms for DOA estimation'. In: *Physical Communication* 31 (2018), pp. 87–95 (cited on page 6).

[21] Christoph Stoeckle et al. 'DoA estimation performance and computational complexity of subspace-and compressed sensing-based methods'. In: *WSA 2015; 19th International ITG Workshop on Smart Antennas*. VDE. 2015, pp. 1–6 (cited on page 6).

[22] Richard Roy and Thomas Kailath. 'ESPRIT-estimation of signal parameters via rotational invariance techniques'. In: *IEEE Transactions on acoustics, speech, and signal processing* 37.7 (2002), pp. 984–995 (cited on page 6).

[23] Yuji Liu, Huixiu Chen, and Biao Wang. 'A direction of arrival estimation method based on deep learning'. In: *Journal of Physics: Conference Series* 1550 (2020). DOI: `10.1088/1742-6596/1550/3/032066` (cited on page 6).

[24] Jianwei Wan et al. 'Direction of arrival estimation based on neural networks'. In: *Applications and Science of Artificial Neural Networks III*. Vol. 3077. 1997. DOI: `10.1117/12.271528` (cited on page 6).

[25] Min Huang et al. 'A comprehensive review of metasurface-assisted direction-of-arrival estimation'. In: *Nanophotonics* 13.24 (2024), pp. 4381–4396. DOI: `doi:10.1515/nanoph-2024-0423` (cited on page 6).

[26] A B Anne Gowda et al. 'A Comprehensive Survey on Subspace-based Direction of Arrival Estimation Algorithms: Performance, Accuracy and Complexity Analysis'. In: *2025 International Conference on Knowledge Engineering and Communication Systems (ICKECS)*. 2025, pp. 1–7. DOI: `10.1109/ICKECS65700.2025.11035231` (cited on page 6).

[27] Dor Haim Shmuel et al. 'SubspaceNet: Deep Learning-Aided Subspace Methods for DoA Estimation'. In: *IEEE Transactions on Vehicular Technology* 74.3 (2025), pp. 4962–4976. DOI: `10.1109/TVT.2024.3496119` (cited on page 6).

[28] Wei Mao and Feng Xi. 'Subspace-based DOA estimation method for coherent signals assisted by transformer'. In: *Sixteenth International Conference on Signal Processing Systems (ICSPS 2024)*. Ed. by Robert Minasian and Li Chai. Vol. 13559. International Society for Optics and Photonics. SPIE, 2025, p. 1355911. DOI: `10.1117/12.3061524` (cited on page 7).

[29] Xiaoxuan Xu and Qinghua Huang. 'MD-DOA: A Model-Based Deep Learning DOA Estimation Architecture'. In: *IEEE Sensors Journal* 24.12 (2024), pp. 20240–20253. DOI: `10.1109/JSEN.2024.3396337` (cited on page 7).

[30] Constantine A. Balanis. *Antenna Theory: Analysis and Design*. 4th ed. John Wiley & Sons, 2016 (cited on page 7).

[31] Harry L. Van Trees. *Optimum Array Processing: Part IV of Detection, Estimation, and Modulation Theory*. New York: John Wiley & Sons, 2002 (cited on pages 8–11).

[32] H. Krim and M. Viberg. 'Two decades of array signal processing research: the parametric approach'. In: *IEEE Signal Processing Magazine* 13.4 (1996), pp. 67–94. DOI: `10.1109/79.526899` (cited on pages 8–12).

[33] Marius Pesavento, Minh Trinh-Hoang, and Mats Viberg. 'Three More Decades in Array Signal Processing Research: An optimization and structure exploitation perspective'. In: *IEEE Signal Processing Magazine* 40.4 (2023), pp. 92–106. DOI: `10.1109/MSP.2023.3255558` (cited on pages 8–10).

[34] Ralph Schmidt. 'Multiple emitter location and signal parameter estimation'. In: *IEEE Transactions on Antennas and Propagation* 34.3 (1986), pp. 276–280 (cited on pages 10–12).

[35] Ying Liu and Hongyuan Cui. 'Antenna Array Signal Direction of Arrival Estimation on Digital Signal Processor (DSP)'. In: *Procedia Computer Science* 55 (2015). 3rd International Conference on Information Technology and Quantitative Management, ITQM 2015, pp. 782–791. DOI: `https://doi.org/10.1016/j.procs.2015.07.158` (cited on page 15).

[36] Mariana G. Pralon et al. 'Suitability of Compact Antenna Arrays for Direction-of-Arrival Estimation'. In: *IEEE Transactions on Antennas and Propagation* 65.12 (2017), pp. 7244–7256. DOI: `10.1109/TAP.2017.2757968` (cited on page 15).

[37] Paolo Rocca et al. 'Single-snapshot DoA estimation in array antennas with mutual coupling through a multiscaling BCS strategy'. In: *IEEE Transactions on Antennas and Propagation* 65.6 (2017), pp. 3203–3213 (cited on page 16).

[38] Oluwole John Famoriji and Thokozani Shongwe. 'Electromagnetic machine learning for estimation and mitigation of mutual coupling in strongly coupled arrays'. In: *ICT Express* 9.1 (2023), pp. 8–15 (cited on page 16).

[39] Oluwole John Famoriji, Oludare Y Ogundepo, and Xiaokang Qi. 'An intelligent deep learning-based direction-of-arrival estimation scheme using spherical antenna array with unknown mutual coupling'. In: *IEEE Access* 8 (2020), pp. 179259–179271 (cited on page 16).

[40] Oluwole John Famoriji and Thokozani Shongwe. 'Source Localization of EM Waves in the Near-Field of Spherical Antenna Array in the Presence of Unknown Mutual Coupling'. In: *Wireless Communications and Mobile Computing* 2021.1 (2021), p. 3237219 (cited on page 16).

[41] Oluwole John Famoriji and Thokozani Shongwe. 'Spherical atomic norm-inspired approach for direction-of-arrival estimation of EM waves impinging on spherical antenna array with undefined mutual coupling'. In: *Applied Sciences* 13.5 (2023), p. 3067 (cited on page 16).

[42] Ottavio Crisafulli et al. 'Octagonal Patch Tag Antenna and 3 x 3 Array Locator for DoA Applications'. In: *2024 18th European Conference on Antennas and Propagation (EuCAP)*. 2024, pp. 1–4. DOI: `10.23919/EuCAP60739.2024.10501650` (cited on pages 16, 21, 34).

[43] Santi Concetto Pavone et al. 'Design of dual circularly polarized sequentially-fed patch antennas for satellite applications'. In: *Applied Sciences* 10.6 (2020), p. 2107 (cited on page 16).

[44] Harine Govindarajan et al. 'Design of a compact dual circular-polarized antenna for L-band satellite applications'. In: *IEEE Antennas and Wireless Propagation Letters* 19.4 (2020), pp. 547–551 (cited on page 16).

[45] Gaurav Kumar, Vrinda Gupta, and Rahul Tank. 'Phase-based angle estimation approach in indoor localization system using Bluetooth low energy'. In: *2020 International Conference on Smart Electronics and Communication (ICOSEC)*. IEEE. 2020, pp. 904–912 (cited on page 20).

[46] Wei Zhao et al. 'Multiple-target localization by millimeter-wave radars with trapezoid virtual antenna arrays'. In: *IEEE Internet of Things Journal* 9.20 (2022), pp. 19589–19598 (cited on pages 23, 24).

[47] QS Ren and AJ Willis. 'Extending MUSIC to single snapshot and on line direction finding applications'. In: *Radar Systems (RADAR 97)*. IET, 1997, pp. 783–787 (cited on page 25).

[48] Michele Perrone, Danilo Pietro Pau, and Nicoló Ivan Piazzese. 'Constrained neural estimation of Bluetooth direction of arrival with non-uniform arrays'. In: *2022 IEEE International Conference on Consumer Electronics (ICCE)*. IEEE. 2022, pp. 1–6 (cited on page 25).

[49] Matteo Carlin et al. 'Directions-of-arrival estimation through Bayesian compressive sensing strategies'. In: *IEEE Transactions on Antennas and Propagation* 61.7 (2013), pp. 3828–3838 (cited on page 25).

[50] Fangqing Wen et al. '2D-DOD and 2D-DOA estimation using sparse L-shaped EMVS-MIMO radar'. In: *IEEE Transactions on Aerospace and Electronic Systems* 59.2 (2022), pp. 2077–2084 (cited on page 31).

[51] Fangqing Wen et al. 'Compressive sampling framework for 2D-DOA and polarization estimation in mmWave polarized massive MIMO systems'. In: *IEEE Transactions on Wireless Communications* 22.5 (2022), pp. 3071–3083 (cited on page 31).

[52] Liangtian Wan et al. 'Deep learning based autonomous vehicle super resolution DOA estimation for safety driving'. In: *IEEE Transactions on Intelligent Transportation Systems* 22.7 (2020), pp. 4301–4315 (cited on page 31).

[53] Ming-Yi You. 'A unified two-dimensional direction finding approach for sensor arrays based on deep neural networks with inhomogeneous angle and frequency partition'. In: *IEEE Sensors Journal* 22.7 (2022), pp. 6840–6850 (cited on page 31).

[54] Wenli Zhu et al. 'Two-dimensional DOA estimation via deep ensemble learning'. In: *IEEE Access* 8 (2020), pp. 124544–124552 (cited on pages 31, 33).

[55] Saleh A Alawsh et al. 'Sparse billboard and t-shaped arrays for two-dimensional direction of arrival estimation'. In: *IEEE Open Journal of Signal Processing* 4 (2023), pp. 322–335 (cited on page 31).

[56] Ibrahim Aboumahmoud et al. 'A review of sparse sensor arrays for two-dimensional direction-of-arrival estimation'. In: *IEEE Access* 9 (2021), pp. 92999–93017 (cited on page 31).

[57] Zhaolin Wang, Xidong Mu, and Yuanwei Liu. 'STARS enabled integrated sensing and communications'. In: *IEEE transactions on wireless communications* 22.10 (2023), pp. 6750–6765 (cited on page 31).

[58] Seyed Ali Keivaan, Pascal Burasa, and Ke Wu. 'Virtual receiver matrix and combinatory analog operations for future multifunction reconfigurable sensing and communication wireless systems'. In: *IEEE Transactions on Microwave Theory and Techniques* 71.1 (2022), pp. 424–433 (cited on page 31).

[59] Fangqing Wen et al. '3-D positioning method for anonymous UAV based on bistatic polarized MIMO radar'. In: *IEEE Internet of Things Journal* 10.1 (2022), pp. 815–827 (cited on page 31).

[60] Zhigang Chen, Lei Wang, and Lu Chen. 'Virtual antenna array and multipath AOA-delay fingerprints based location for moving targets'. In: *IEEE Access* 8 (2020), pp. 186919–186931 (cited on page 31).

[61] Jianfeng Li et al. 'Improved DFT algorithm for 2D DOA estimation based on 1D nested array motion'. In: *IEEE Communications Letters* 24.9 (2020), pp. 1953–1956 (cited on page 32).

[62] Qiuze Yu et al. 'A novel 2D off-grid DOA estimation method based on compressive sensing and least square optimization'. In: *IEEE Access* 7 (2019), pp. 113596–113604 (cited on page 32).

[63] Ke Xiao et al. 'Abnormal behavior detection scheme of UAV using recurrent neural networks'. In: *IEEE Access* 7 (2019), pp. 110293–110305 (cited on page 32).

[64] Kunda Wang, Lin Shi, and Tao Chen. 'Two-Dimensional Separable Gridless Direction-of-Arrival Estimation Based on Finite Rate of Innovation'. In: *IEEE Access* 9 (2021), pp. 17275–17283 (cited on page 32).

[65] MA Hannan et al. 'Fast direction of arrival estimation using subspace-based methods for BLE applications'. In: *2024 IEEE International Symposium on Antennas and Propagation and INC/USNC-URSI Radio Science Meeting (AP-S/INC-USNC-URSI)*. IEEE. 2024, pp. 1457–1458 (cited on page 34).

[66] Brad R Jackson. '2D direction of arrival estimation using uniform circular arrays with radiation pattern reconfigurable antennas'. In: *IEEE Access* 10 (2022), pp. 11909–11923 (cited on pages 36, 37).

[67] Merhala Thurai et al. 'Retrieving Rain Drop Size Distribution Moments from GPM Dual-Frequency Precipitation Radar'. In: *Remote Sensing* 13.22 (2021). DOI: `10.3390/rs13224690` (cited on page 39).

[68] Hao Huang et al. 'Uncertainty in Retrieving Raindrop Size Distribution from Polarimetric Radar Measurements'. In: *Journal of Atmospheric and Oceanic Technology* 36 (4 Apr. 2019), pp. 585–605. DOI: `10.1175/JTECH-D-18-0107.1` (cited on page 39).

[69] Merhala Thurai et al. 'Measurements and Modeling of the Full Rain Drop Size Distribution'. In: *Atmosphere 2019, Vol. 10, Page 39* 10 (1 Jan. 2019), p. 39. DOI: `10.3390/ATMOS10010039` (cited on page 39).

[70] Edward A. Brandes, Guifu Zhang, and Juanzhen Sun. 'On the Influence of Assumed Drop Size Distribution Form on Radar-Retrieved Thunderstorm Microphysics'. In: *Journal of Applied Meteorology and Climatology* 45 (2 Feb. 2006), pp. 259–268. DOI: `10.1175/JAM2335.1` (cited on pages 39, 40).

[71] Thomas T. Wilheit, V. Chandrasekar, and Wanyu Li. 'Impact of Uncertainty in the Drop Size Distribution on Oceanic Rainfall Retrievals From Passive Microwave Observations'. In: *IEEE Transactions on Geoscience and Remote Sensing* 45.10 (2007), pp. 3160–3164. DOI: `10.1109/TGRS.2007.903824` (cited on page 39).

[72] Qing Cao et al. 'Analysis of Video Disdrometer and Polarimetric Radar Data to Characterize Rain Microphysics in Oklahoma'. In: *Journal of Applied Meteorology and Climatology* 47.8 (2008), pp. 2238–2255. DOI: `10.1175/2008JAMC1732.1` (cited on page 40).

[73] Marios N. Anagnostou et al. 'Comparison of Two Raindrop Size Distribution Retrieval Algorithms for X-Band Dual Polarization Observations'. In: *Journal of Hydrometeorology* 9 (3 June 2008), pp. 589–600. DOI: `10.1175/2007JHM904.1` (cited on page 40).

[74] E Gorgucci, V Chandrasekar, and VN Bringi. 'Drop size distribution retrieval from polarimetric radar measurements'. In: *Proceedings of ERAD*. Vol. 134. 139. 2002 (cited on page 40).

[75] V Bringi et al. 'Retrieval of lower-order moments of the drop size distribution using CSU-CHILL X-band polarimetric radar: a case study'. In: *Atmospheric Measurement Techniques* 13 (9 2020), pp. 4727–4750. DOI: `10.5194/amt-13-4727-2020` (cited on page 40).

[76] Matias Alcoba, Hervé Andrieu, and Marielle Gosset. 'An Inverse Method for Drop Size Distribution Retrieval from Polarimetric Radar at Attenuating Frequency'. In: *Remote Sensing 2022, Vol. 14, Page 1116* 14 (5 Feb. 2022), p. 1116. DOI: `10.3390/RS14051116` (cited on page 40).

[77] George Sinclair. 'The transmission and reception of elliptically polarized waves'. In: *Proceedings of the IRE* 38.2 (2006), pp. 148–151 (cited on page 41).

[78] V. N. Bringi and V. Chandrasekar. *Polarimetric Doppler Weather Radar: Principles and Applications*. Cambridge University Press, Aug. 2001 (cited on pages 41, 47, 48).

[79] Kenneth V. Beard, V. N. Bringi, and M. Thurai. 'A new understanding of raindrop shape'. In: *Atmospheric Research* 97 (4 Sept. 2010), pp. 396–415. DOI: `10.1016/J.ATMOSRES.2010.02.001` (cited on page 44).

[80] David Atlas. 'Optical Extinction By Rainfall'. In: *Journal of Atmospheric Sciences* 10 (6 1953), pp. 486–488. DOI: `10.1175/1520-0469(1953)010<0486:OEBR>2.0.CO;2` (cited on page 45).

[81] Carlton W Ulbrich. 'Natural Variations in the Analytical Form of the Raindrop Size Distribution'. In: *Journal of Climate and Applied Meteorology* 22 (10 1983), pp. 1764–1775 (cited on pages 45, 46).

[82] Walter H. Wischmeier and Dwight D. Smith. 'Rainfall energy and its relationship to soil loss'. In: *Eos, Transactions American Geophysical Union* 39 (2 Apr. 1958), pp. 285–291. DOI: `10.1029/TR039I002P00285;CTYPE:STRING:JOURNAL` (cited on page 45).

[83] J S Marshall, R C Langille, and W Mc K Palmer. 'Measurement Of Rainfall By Radar'. In: *Journal of Atmospheric Sciences* 4 (6 1947), pp. 186–192. DOI: `10.1175/1520-0469(1947)004<0186:MORBR>2.0.CO;2` (cited on page 45).

[84] David B Johnson and Kenneth V Beard. 'Oscillation Energies of Colliding Raindrops'. In: *Journal of Atmospheric Sciences* 41 (7 1984), pp. 1235–1241. DOI: `10.1175/1520-0469(1984)041<1235:OEOCR>2.0.CO;2` (cited on page 45).

[85] K R Hardy. 'The Development of Raindrop-size Distributions and Implications Related to the Physics of Precipitation'. In: *Journal of Atmospheric Sciences* 20 (4 1963), pp. 299–312. DOI: `10.1175/1520-0469(1963)020<0299:TDORSD>2.0.CO;2` (cited on page 45).

[86] M. Thurai, C. R. Williams, and V. N. Bringi. ‘Examining the correlations between drop size distribution parameters using data from two side-by-side 2D-video disdrometers’. In: *Atmospheric Research* 144 (July 2014), pp. 95–110. doi: `10.1016/J.ATMOSRES.2014.01.002` (cited on page 47).

[87] Udo Kaatze. ‘Complex permittivity of water as a function of frequency and temperature’. In: *Journal of Chemical and Engineering Data* 34 (4 Oct. 2002), pp. 371–374. doi: `10.1021/JE00058A001` (cited on pages 48, 57).

[88] Kyuhee Shin et al. ‘Polarimetric Retrieval of Raindrop Size Distribution: Double-Moment Normalization Approach and Machine Learning Techniques’. In: *Geophysical Research Letters* 51 (1 Jan. 2024), e2023GL106057. doi: `10.1029/2023GL106057;PAGE:STRING:ARTICLE/CHAPTER` (cited on page 48).

[89] Gianfranco Vulpiani et al. ‘Polarimetric weather radar retrieval of raindrop size distribution by means of a regularized artificial neural network’. In: *IEEE Transactions on Geoscience and Remote Sensing* 44 (11 Nov. 2006), pp. 3262–3274. doi: `10.1109/TGRS.2006.878438` (cited on page 48).

[90] Robert Conrick, Joseph P. Zagrodnik, and Clifford F. Mass. ‘Dual-Polarization Radar Retrievals of Coastal Pacific Northwest Raindrop Size Distribution Parameters Using Random Forest Regression’. In: *Journal of Atmospheric and Oceanic Technology* 37 (2 Feb. 2020), pp. 229–242. doi: `10.1175/JTECH-D-19-0107.1` (cited on page 48).

[91] Sylvia Hochstuhl et al. ‘Your Input Matters—Comparing Real-Valued PolSAR Data Representations for CNN-Based Segmentation’. In: *Remote Sensing 2023, Vol. 15, Page 5738* 15 (24 Dec. 2023), p. 5738. doi: `10.3390/RS15245738` (cited on page 48).

[92] Rich Caruana, Lorien Pratt, and Sebastian Thrun. ‘Multitask Learning’. In: *Machine Learning 1997 28:1* 28 (1 1997), pp. 41–75. doi: `10.1023/A:1007379606734` (cited on page 50).

[93] Jimmy Lei Ba, Jamie Ryan Kiros, and Geoffrey E. Hinton. ‘Layer Normalization’. In: (July 2016) (cited on page 50).

[94] Chao Hsin Chen et al. ‘Vertical Wind Effect on Slope and Shape Parameters of Gamma Drop Size Distribution’. In: *Journal of Atmospheric and Oceanic Technology* 37 (2 Feb. 2020), pp. 243–262. doi: `10.1175/JTECH-D-18-0026.1` (cited on page 54).

List of Publications

Journal Articles

1. O. Crisafulli, N. I. Piazzese, S. C. Pavone, G. Giammello, G. Galvagna, S. Pitrulli, A. F. Morabito, L. Di Donato, M. Sardo, G. Sorbello. ’Performance analysis of BLE-5.1 angle of arrival estimation using embedded radiation patterns on a 3 x 3 uniform rectangular array’. In: *IEEE Access* 12 (2024), pp. 42572-42584.
2. M. A. Hannan, O. Crisafulli, G. Giammello, G. Sorbello. ’On the Error Metrics Used for Direction of Arrival Estimation’. In: *Sensors* 25.8 (2025), p. 2358.

Works outside the scope of this thesis

Journal Articles

1. D. C. Guastella, L. Cantelli, G. Giammello, C. D. Melita, G. Spatino, G. Muscato. ’Complete coverage path planning for aerial vehicle flocks deployed in outdoor environments’. In: *Computers & Electrical Engineering* 75 (2019), pp. 189-201.
2. G. Giammello, M. Firetto Carlino, M. Coltelli. ’Automatic detection of the explosive activity of the Mt. Etna volcano through Doppler radar monitoring’. In: *Remote Sensing*, 14.22 (2022), p. 5663.

Conference papers

1. O. Crisafulli, D. Guarnera, G. Giammello, A. F. Morabito, S. C. Pavone, L. Di Donato, G. Sorbello. ’Octagonal patch tag antenna and 3 x 3 array locator for DoA applications’. In: *2024 18th European Conference on Antennas and Propagation (EuCAP)* (2024), pp. 1-4.
2. M. A. Hannan, O. Crisafulli, G. Giammello, A. F. Morabito, L. Di Donato, S. C. Pavone, G. Sorbello. ’Low Cost Array Design and Exploitation for DoA in Multipath Propagation Environment’. In: *2024 17th United Conference on Millemetre Waves and Terahertz Technologies (UCMMT)* (2024), pp. 13-16.

Datasets

1. E. Adirosi, et al. ’Database of the Italian disdrometer network (V04)’. In: *Zenodo* (2025). DOI: 10.5281/zenodo.17432012

Alphabetical Index

array manifold, 9
array reconstruction
    CSV, 10
    ERP, 21
array steering
    matrix, 9
    vector, 8

distribution
    drop size, 44
    gamma DSD, 46
    von Mises-Fisher, 47
DoA algorithms, 10
    Bartlett, 11
    MUSIC, 11

error metrics
    angular distance, 33
    MAE, 32
    MSE, 32
    RMSE, 32

Layer normalisation, 50

Multi-Task Learning, 50

polarimetric
    covariance matrix, 42
    scattering matrix, 41
polarisability matrix, 42